# A Computational Workbench Environment for Virtual Power Plant Simulation

**Quarterly Progress Report**

Reporting Period Start Date: October 1, 2003
Reporting Period End Date: December 31, 2003

Mike Bockelie, REI
Dave Swensen, REI
Martin Denison, REI
Zumao Chen, REI
Mike Maguire, REI
Adel Sarofim, REI
Changguan Yang, REI
Hong-Shig Shim, REI

January 28, 2004

DOE Cooperative Agreement No: DE-FC26-00NT41047

Reaction Engineering International
77 West 200 South, Suite 210
Salt Lake City, UT 84101

# Disclaimer

"This report was prepared as an account of work sponsored by an agency of the United States Government. Neither the United States Government nor any agency thereof, nor any of their employees, makes any warranty, express or implied, or assumes any legal liability or responsibility for the accuracy, completeness, or usefulness of any information, apparatus, product, or process disclosed, or represents that its use would not infringe privately owned rights. Reference herein to any specific commercial product, process, or service by trade name, trademark, manufacturer, or otherwise, does not necessarily constitute or imply its endorsement, recommendation, or favoring by the United States Government or any agency thereof. The views and opinions of authors expressed herein do not necessarily state or reflect those of the United States Government or any agency thereof."

# Abstract

This is the thirteenth Quarterly Technical Report for DOE Cooperative Agreement No: DE-FC26-00NT41047. The goal of the project is to develop and demonstrate a Virtual Engineering-based framework for simulating the performance of Advanced Power Systems. Within the last quarter, good progress has been made on all aspects of the project. Software development efforts have focused on a preliminary detailed software design for the enhanced framework. Given the complexity of the individual software tools from each team (i.e., Reaction Engineering International, Carnegie Mellon University, Iowa State University), a robust, extensible design is required for the success of the project. In addition to achieving a preliminary software design, significant progress has been made on several development tasks for the program. These include: 1) the enhancement of the controller user interface to support detachment from the Computational Engine and support for multiple computer platforms, 2) modification of the Iowa State University interface-to-kernel communication mechanisms to meet the requirements of the new software design, 3) decoupling of the Carnegie Mellon University computational models from their parent IECM (Integrated Environmental Control Model) user interface for integration with the new framework and 4) development of a new CORBA-based model interfacing specification. A benchmarking exercise to compare process and CFD based models for entrained flow gasifiers was completed. A summary of our work on intrinsic kinetics for modeling coal gasification has been completed. Plans for implementing soot and tar models into our entrained flow gasifier models are outlined. Plans for implementing a model for mercury capture based on conventional capture technology, but applied to an IGCC system, are outlined.

# Table of Contents

DISCLAIMER……. i

ABSTRACT…… ii

TABLE OF CONTENTS……... iii

EXECUTIVE SUMMARY……. 1

EXPERIMENTAL METHODS…….. 3
Task 1 Program Management …… 3
Task 2 Framework Enhancement – Software…… 5
Task 3 Framework Enhancement – Modeling... ……15

RESULTS AND DISCUSSION……..……19

CONCLUSIONS……..……36

REFERENCES……...……..37

APPENDIX
A. IDL for Virtual Engineering Framework……..……....38
B. Development of a Kinetics Preprocessor for Modeling Coal Gasification ……..41

# 1

# Executive Summary

The work to be conducted in this project received funding from the Department of Energy under Cooperative Agreement No: DE-FC26-00NT41047. This project period of performance started October 1, 2000. Through a Budget Revision, the project will continue to September 30, 2004.

The goal of the project is to develop and demonstrate a computational workbench, or *framework*, for simulating the performance of Advanced Power Generation Systems. The Year One effort focused on developing a prototype workbench for the DOE Low-Emissions Boiler System (LEBS) Proof of Concept (POC) design. The Year Two effort focused on developing a more advanced workbench environment for simulating a gasifier-based Vision 21 energyplex. The Year Three effort focused on continued development of the workbench environment and application of the workbench to Vision 21 plant configurations. The Year Four effort, which corresponds to the Budget Revision time period, is incorporating software enhancements to the workbench environment to (a) move it toward a Virtual Engineering based software framework, in which there is available a hierarchy of plant component models that can be connected in a user centered, interactive, immersive, 3D environment and (b) implement improvements to component models for critical plant processes, such as gasification and syngas clean up (including gas separation and mercury capture). This work effort is being closely coordinated with DOE funded projects at Carnegie Mellon University (CMU) and the Iowa State University Virtual Reality Applications Center (ISU) that are also developing simulation tools for use in evaluating Advanced Power Generation Systems.

The main accomplishments during the last three months included:

- Completion of a preliminary software design to support the Virtual Engineering based framework, including:
  - Design of the overall structure of the framework software, including definition and role of major components
  - Choice of appropriate open source libraries for implementation of enhanced user interface and communication mechanisms
  - CORBA IDL design to provide communication and data passing between framework software components
  - Design for integration of ISU Virtual Engineering capabilities with framework
  - Design for integration of CMU modeling capabilities with framework

- Continued software development to create the Virtual Engineering framework, including:
  - The enhancement of the controller user interface to support detachment from the Computational Engine and support for multiple computer platforms
  - Modification of the ISU interface-to-kernel communication mechanisms to meet the requirements of the new software design
  - Decoupling of the CMU computational models from their parent IECM (Integrated Environmental Control Model) user interface for integration with the new framework
  - Development of a CORBA-based model interfacing specification (MILESTONE)

- An updated version of the workbench was installed at NETL (Morgantown), and another user training session was provided to NETL personnel.

- An updated version of the workbench was provided to the CCSD. The CCSD has continued to provide valuable feedback on suggested improvements for the workbench and the component models contained within the workbench. The suggested enhancements have been implemented and are contained in the versions of the workbench provided to the NETL and CCSD.

- The coordinated effort between Reaction Engineering International (REI) and DOE funded projects at Carnegie Mellon University (CMU) and the Iowa State University Virtual Reality Applications Center (ISU) has made good progress. The teams communicate via email and conference calls frequently and have developed positive, productive working relationships. A software repository is being established at ISU to provide coordinated access to all personnel working on the program regardless of geographical location.

- An extensive write-up on our approach for including intrinsic kinetics for coal gasification has been completed and is provided herein. Continued collaboration with colleagues at the CCSD in Australia is planned for benchmarking of an intrinsic kinetics pre-processor tool.

- Plans for implementing sub-models for soot and tar production/destruction within an entrained flow gasifier and a model for mercury capture in an IGCC system are highlighted.

Each of these topics is discussed in the following sections.

# 3

# Experimental Methods

Within this section we present brief discussions on the many subtasks that must be addressed in developing the workbench (framework). For simplicity, the discussion items are presented in the order of the tasks as outlined in our Budget Revision.

## Task 1 – Program Management

During the last performance period, REI project team members traveled to NETL (Morgantown) on October 28, 2003 to facilitate technology transfer. An updated version of the workbench framework was installed at NETL and a presentation to members of the Computational Energy Sciences (CES) group was conducted. The presentation included demonstrations of operating the workbench. The updated workbench included modifications requested during previous visits to NETL.

An updated version of the workbench framework was provided to the Collaborative Research Center for Coal and Sustainable Development (CCSD) in Australia. The CCSD is investigating the use of the workbench for IGCC plant evaluations. This collaborative effort is being performed through a Memo of Understanding (MOU) between REI and the CCSD.

During the last performance period, REI has continued to work closely with collaborators at **Carnegie Mellon University** (**CMU**, Program Manager: Prof. Ed Rubin) and the **Iowa State University Virtual Reality Applications Center** (**ISU**, Program Manager: Prof. Mark Bryden). The result of the collaboration, or coordinated effort, will be a software framework based on Virtual Engineering concepts in which there is available a hierarchy of plant component models that can be connected in a user-centered, interactive, immersive, 3D environment. The Virtual Engineering based framework will provide the ability to interactively visualize and interrogate Advanced Power Generation plant configurations, including those with CO2 capture such as Futuregen. A conceptual representation of the capability and development effort for the Virtual Engineering framework is shown in the figure below.

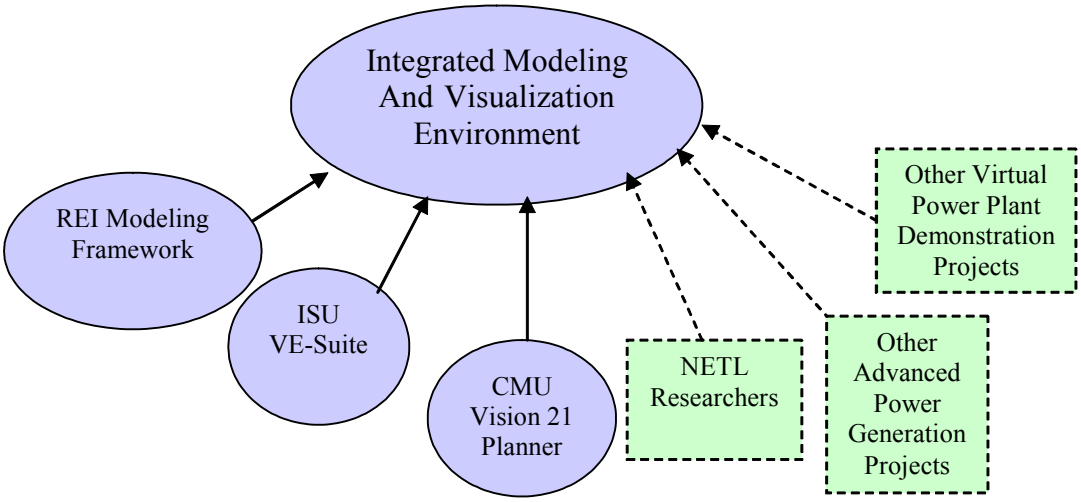

As highlighted in the figure above, REI's role in the CMU-ISU-REI coordinated effort is to incorporate software enhancements to our current simulation framework as well as improvements to component models for key processes needed to simulate emerging concepts for Advanced Power Generation. The CMU team is focused on developing simple models for rapid assessment of the performance and economics of Advanced Power Generation plant configurations, including those with Carbon Management. The ISU team is developing advanced visualization software tools to apply Virtual Engineering principles to power generation systems. The enhanced framework will leverage the work products from these separately funded DOE projects at CMU and ISU. In addition, NETL researchers, NETL funded projects and other projects developing simulation tools for modeling advanced power generation systems will be encouraged to collaborate with our coordinated effort.

- During the last performance period, a series of information exchanges were conducted between technical and management level personal from CMU, ISU and REI, relating to model interfacing, software exchange, resource allocation and working together in a coordinated manner. To ensure proper coordination, conference calls that include senior personnel are held on roughly a bi-weekly basis. Conference calls that include technical personnel are held on roughly a weekly basis and email communication occurs as needed. As noted herein, good progress is being made on the coordinated efforts.
- During the next performance period
  - Mr. Doug McCorkle (a graduate student at ISU), will visit REI to work directly with the REI personnel developing software elements that will need to interact closely with the ISU VE Suite software.
  - Technical personnel from CMU, ISU and REI will meet at ISU to coordinate development efforts and test an "alpha" version of the enhanced framework in the immersive visualization facilities at ISU.
  - Assuming successful demonstration of the "alpha" version of the framework, technical and management personnel from CMU, ISU and REI will subsequently meet at ISU to exercise an upgraded "alpha" version of the enhanced framework in the immersive visualization facilities at ISU.

Described in the section labeled Component Models (pp.12-14) is an overview of a model interface specification that represents achievement of our project milestone for Q1 of GFY2004. Provided in Appendix A is a detailed description of the proposed model interface specification.

# Task 2 – Framework Enhancement - Software

This task involves the integration of the different capabilities of the simulation tools being used by REI, CMU and ISU to create an integrated modeling and visualization environment. The design of this modeling environment will make it possible to interactively configure, analyze, interrogate and visualize advanced power systems on a wide range of platforms and at different levels of detail.

**Overview**

During the last quarter, efforts have been focused primarily on the software design for the virtual engineering based simulation environment. Given the complexity of the individual software tools from each team, a robust extensible design was deemed crucial to the success of the project. Details of the design are outlined later in this section.

In addition to achieving a preliminary software design, significant progress has been made on several development tasks for the program. These include:

1) the enhancement of the controller user interface to support detachment from the Computational Engine and support for multiple computer platforms,
2) modification of the ISU interface-to-kernel communication mechanisms to meet the requirements of the new software design,
3) decoupling of the CMU computational models from their parent IECM (Integrated Environmental Control Model) user interface for integration with the new framework and
4) development of a new CORBA-based model interfacing specification.

Software design details in addition to each of these development tasks are discussed in the following sections.

**Software Design and Implementation Details**

A key task accomplished during the last quarter involved the completion of a preliminary software design for the new modeling and visualization framework. This design includes the completion of the milestone for the past quarter which involved creating an enhanced model interfacing IDL specification (see Appendix A).

Figure 1 shows a high-level schematic of the software design. As seen in this figure, the key elements of the design are the user interface, Computational Engine, Visualization Engine and component models. Note that the various software elements all exist as independent CORBA components with standardized Interface Definition Language (IDL) implementations (denoted with “C” in a circle). The use of component architecture design techniques has numerous advantages for this application including platform independence, location transparency and reuse of component models.

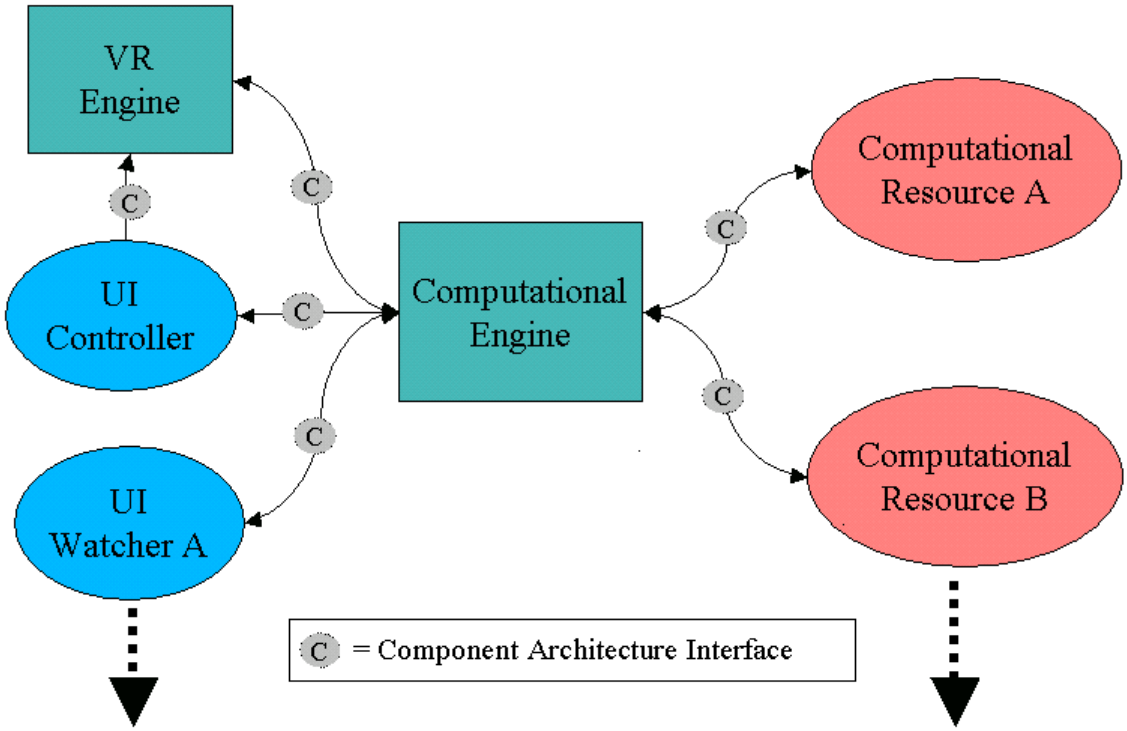


Figure 1. Advanced Power Simulation Framework Design

The following sections will detail the design of each of these elements, describe how they contribute to the overall framework functionality, and give their current developmental status.

*User Interface*

To achieve the goals outlined for this project, a powerful and flexible user interface (UI) is a necessity. The design goals for the user interface are:

- Multi-platform support
- Detachable/Location transparency
- Extensibility
- Unified control

Figure 2 illustrates the internal construction of the UI and its interaction with other major software components. This figure provides a level of detail beyond that given in Figure 1.

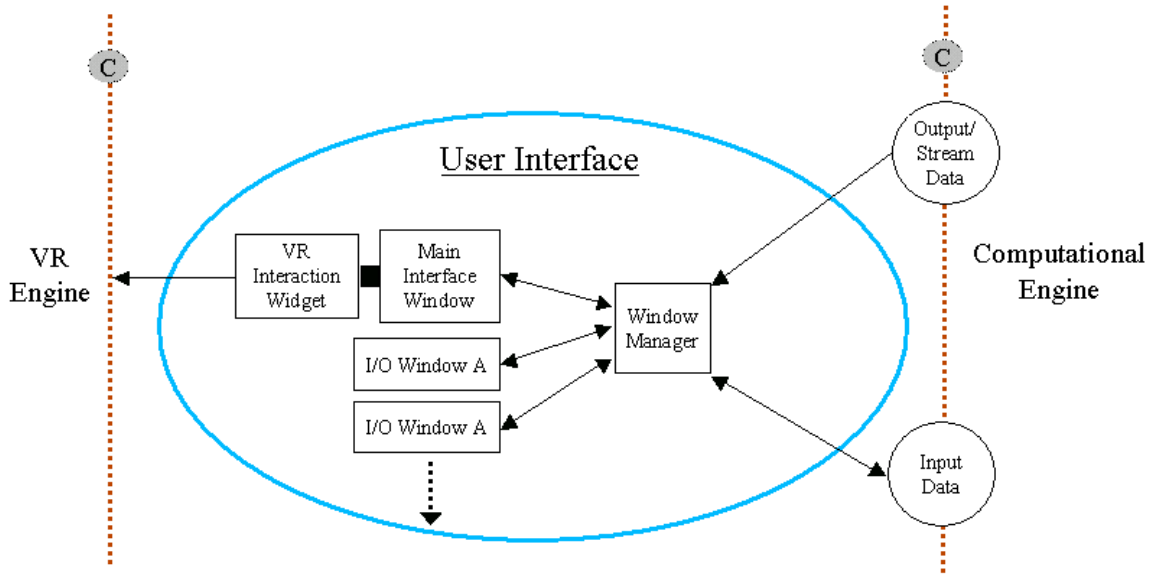


Figure 2. Details of the User Interface Design

Further details of the UI design, including the current state of the implementation are described in the following sections.

*Multi-Platform support:* The UI needs to make use of platform independent libraries to enable the software to run on a wide range of computer hardware and operating systems. These platforms range from Unix workstations to Pocket PC's and PDA's. This functionality is ideal for the virtual engineering based system being developed since users will frequently make use of handheld computing devices inside of immersive environments (e.g. cave-like systems at ISU-VRAC, NETL).

In order to provide complete platform independence, it was necessary to choose two open source libraries. The first library is for the user interface functionality and the second is for the component architecture. Details of these library choices are give in the following sections.

*1) User Interface Library:* After reviewing a number of different UI packages, we chose WxWindows (www.wxwindows.org). WxWindows is one of the best cross-platform GUI packages available. It is well maintained, has a large user base, and has ports for Windows, Unix/X11, Unix/Motif, OS2, Mac and GTK. It also has an alpha version of a Windows CE port, which is under active development. This ensures that the user interface will run on all major platforms and even on Pocket PC-based PDA's (limited functionality now). WxWindows' license essentially is the L-GPL (Library General Public License), with an exception stating that derived works in binary form may be distributed on the users own terms. These characteristics make WxWindows an excellent choice for this project.

*2) Component Architecture Library:* Given that CORBA was chosen as the component architecture, it was necessary to choose an open source CORBA implementation. It should be noted that CORBA is used not just in the UI code, but is used throughout the various framework components to provide efficient, platform independent and distributed communication.

In choosing a CORBA implementation there were two main points to be considered. First, the library must be an Open Source library and under active development. Second, the library must support multiple operating systems. With these guidelines, two libraries, omniORB (omniorb.sourceforge.net) and TAO (The ACE ORB) (www.cs.wustl.edu/~schmidt/TAO.html), were selected for comparison and trial use with simple simulations. Both of these libraries are respected in the simulation community as solid implementations of the CORBA specification. They both support multiple operating systems and satisfied the initial requirements for the Computational Engine and the Visualization Engine.

Since both of the libraries were comparable, further criteria were used to select TAO for use in the framework. The main advantage influencing the decision was that TAO has a Real-Time interface that will allow better synchronization with the Computational Engine when dynamic and large simulations are run. The TAO library also supports the WinCE platform which will allow support of PocketPC PDAs.

*Detachable/Location Transparency:* The UI needs to exist independently from the Computational Engine. This functionality allows the UI to be attached and detached from an active simulation from any compatible computer on the network. As an example, this would allow a user to build and start a simulation and then detach from the Computational Engine. The user could then go to a different location, re-attach to the simulation and regain monitoring and control functions.

To accomplish this functionality we have defined a CORBA IDL interface (see Appendix A) between the UI and the Computational Engine (See Figure 1). This CORBA interface provides all the necessary communication mechanisms between these components. The communication link is bidirectional and handles items such as model parameters passed to the Computational Engine and receives items such as execution status and results from the Computational Engine.

Another advantage of this design is the ability for multiple user interfaces to be attached to the same Computational Engine, allowing multiple users to monitor a simulation from different locations. A locking mechanism will be used so that only one user interface (controller) can change the design and inputs of the simulation.

*Extensibility*: Another important consideration for the UI design is extensibility. The UI should be able to dynamically discover, identify and load UI elements for new component models. This capability will keep the level of difficulty involved in integrating new component models to a minimum and require no modifications to the core interface when new models are added.

The dynamic discover and load capability will be accomplished by loading user developed module UI's from dynamic linking library (DLL in windows) or shared library (SO lib in Linux/Unix). A plug-in base C++ class defining this UI-module interface will be provided to all

module developers. Developers can inherit from this class to create their own module UI and then compile the resulting code into a DLL/Shared library. The user interface framework's plug loader code will recognize the new module and bring that into its user-module library. By this mechanism, the core user interface can plug in the third-party module-specific UI directly from binaries.

*Unified Control:* Another design goal is unified control for all user interaction. This ensures that the user is not burdened with moving between different UI's to perform operations. Thus, there will be a single UI with the ability to: 1) construct, specify, execute and monitor simulations and 2) provide complete control of the 3D VR environment.

To provide this functionality, the UI is designed to communicate via CORBA to not only the Computational Engine, but also to the ISU Visualization Engine (see Figure 1). As was discussed for the UI to Computational Engine link, the use of CORBA with an appropriate IDL provides a flexible, detachable and platform independent communication mechanism for this link.

Current UI Development Status

During the past quarter of work, significant progress has been made toward a prototype UI meeting the aforementioned design requirements. This progress includes:

- Implementation of preliminary functionality to perform dynamic discovery and loading of computational models
- Creation of a flexible mechanism to show graphical depictions of component models
- Basic communication links between the UI, Computational Engine and Visualization Engine
- Implementation of a subset of Visualization Engine control functionality within the UI

*Computational Engine*

The Computational Engine is the core of the framework. Its duties are to construct, coordinate, schedule and monitor plant simulation runs. It must be capable of running a simulation containing a multitude of different types of models, each accepting and generating a myriad of data types. Given the unlimited number of simulation scenarios available for the user to create, the Computational Engine will be focused on a single goal: the successful and accurate plant simulation of a user supplied configuration. To this end, the Computational Engine will be able to analyze a plant configuration, determine execution order, marshal system resources to create model instances, and coordinate the flow of data through the entire simulation framework. Tasks that require specific knowledge about a data type or model are relegated to either a detachable UI or to a specific model, thus keeping the Computational Engine generalized at a high level.

Figure 3 illustrates the internal construction of the Computational Engine and its interaction with other major software components. This figure provides a level of detail beyond that given in Figure 1.

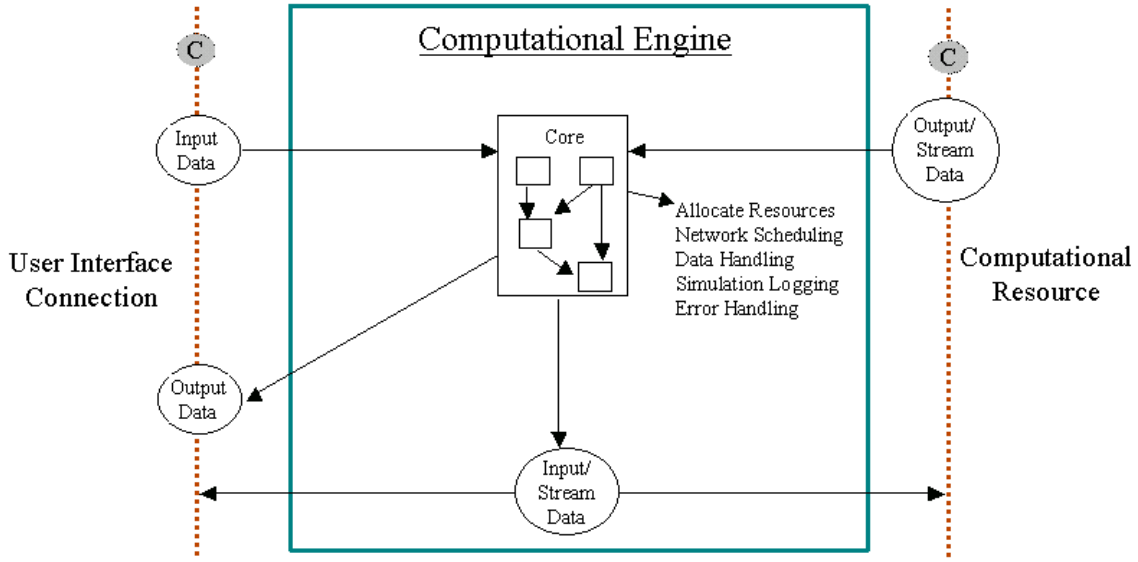


Figure 3. Details of the Computational Engine Design

Important functions that the Computational Engine controls can be broken down into several pieces for explanation: plant configuration, data handling, error handling, relationship to detachable UI, scheduling, resource allocation and relationship to models and logging. Each of these is described in detail below.

*Plant Configuration:* The configuration of the plant, provided by a detachable user interface, will be the primary data structure used by the Computational Engine. Nearly all algorithms utilized, such as proper data flow, scheduling and resource allocation depend on this topology.

*Data Handling:* Since there are an unlimited number of possible models capable of being integrated into the framework (with each model having a different input/output set), it is vital that the Computational Engine have access only to generalized datatypes. To address this requirement, we have designed the CORBA IDL interfaces between the Computational Engine and the component models to use mapped string blocks in combination with common dimensions of array data.

*Error Handling:* With the Computational Engine being the centralized power behind a simulation run, all errors that occur while performing this task (whether originating within its own structure or on an attached model) must be properly handled within the context of this overriding structure. Thus, the Computational Engine will have sophisticated error handling routines, and messaging facilities to alert attached users. To fit into the detached user interface paradigm, any errors that occur on an attached UI will be handled locally.

*Relationship to Detachable UI:* The Computational Engine is a CORBA server, into which a detachable user interface client can connect (see IDL in Appendix A). This detachable UI is where the user is able to create a plant configuration, set model inputs, start and stop execution of simulation, and view simulation results. Once a client-server connection is made, the engine

is able to send results, messages, updates and communications from other attached UI's in real time. The Computational Engine does not require a connection to a UI during a simulation run. Users can connect/disconnect at will to configure, modify or monitor the simulation of a given plant configuration.

*Scheduling:* The Computational Engine will utilize advanced scheduling algorithms developed earlier in this program. The scheduler, at a minimum, will be capable of handling single and embedded feedback loops, iterative solves and, eventually, transient simulation runs.

*Resource Allocation:* Component models will be delegated by the Computational Engine to run on system resources that are seen to be most efficient. These resources include both local and distributed, network accessible computers.

*Relationship to Models:* The Computational Engine, with its CORBA interface, will be able to connect to the various component models available for a simulation. Information passed through this connection will include inputs (user supplied and stream data), outputs, results and general messages. The importance of the CORBA interface being used for this purpose is discussed in detail in the *Component Models* section below.

*Logging:* The Computational Engine will be equipped with a full suite of logging capabilities. Data ranging from schedule information to model results will be logged into a database. This information will be archived for later retrieval.

Current Computational Engine Development Status

During the performance period, significant progress has been made toward a prototype Computational Engine meeting the aforementioned design requirements. This progress includes:

- Implementation of a new prototype model interface specification (CORBA IDL) to define interactions between the Computational Engine and component models (MILESTONE)
- Implementation of CORBA communication mechanisms for interfacing with the detachable UI
- Development of a prototype scheduling algorithm
- Development of a prototype inter-model data passing mechanism

*Visualization Engine*

The Visualization Engine provides the core functionality for the virtual engineering aspect of the framework. It is based on VE-Xplorer which is a portion of the VE-Suite software developed by Prof. Mark Bryden's research group at ISU. VE-Xplorer enables the engineering analysis and design process to take place in a virtual environment. For maximum graphical performance on multiple operating systems, it is built upon VRJuggler (www.vrjuggler.org), OpenGL Performer (www.sgi.com), and Kitware's Visualization ToolKit (VTK, www.vtk.org). This visual interface, controlled by the UI and the Computational Engine, is a graphical representation of the simulation under review.

The Visualization Engine is being generalized to load data not only from comprehensive models, but also from other engineering sources, including results generated from the CMU Vision 21 planner software and other generalized datasets (e.g., experimental data from a test rig). The engine is also being modified to make use of the high level CORBA interface specifications used throughout the software framework. This interface allows the Visualization Engine to communicate with the component models, Computational Engine and the UI directly.

Current Visualization Engine Development Status

During the past quarter of work, significant progress has been made toward integrating the Visualization Engine with the prototype UI. This progress includes:

- Changing the VE-suite CORBA implementation to TAO
- Resolving complicated library and threading interaction and overlap problems
- Creating a new IDL specification for UI-to-Visualization Engine communication
- Development of basic UI control panels for VR parameters
- Successful testing of basic UI-to-Visualization Engine communication

*Component Models*

Component models are mathematical representations of individual plant components which are used by the framework to construct an overall simulation. The key to making the simulation framework extensible is to provide a mechanism by which component models can be easily integrated without the need for extensive software development tasks.

To address these needs, we have adopted the relatively modern idea of component architecture design. CORBA (the component architecture) is used along with a standard model interface definition (implemented as an IDL) to create componentized computational models. These models can be used interchangeably with any framework which supports the standardized IDL, are location transparent (run on any network accessible machine), are platform independent (Linux, Windows, etc), are programming language flexible, and can be distributed in binary form.

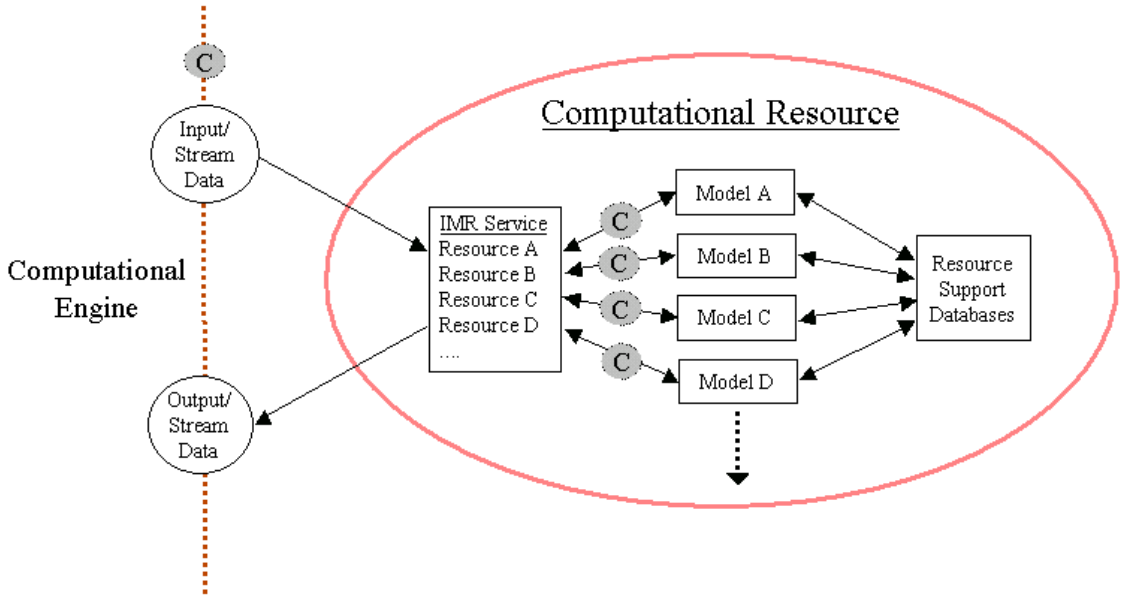


Figure 4. Interaction of Framework and Component Models

The interface to the CORBA-based component models is designed to allow the models to be autonomous, accepting inputs and stream data from the Computational Engine, running the encapsulated model, and generating outputs and modified stream data. Figure 4 illustrates the interaction of the framework with component models on a single computational resource.

It is important to note that the CORBA interface between the Computational Engine and the component models is the standardized model interface supported by the framework for model integration. The interface defined for this project (see Appendix A) is analogous to that of the CAPE-Open specification used by chemical process simulation tools. This newly developed model interface will be able to support CAPE components through wrapping and function mapping. When compared to CAPE, the new interface specification more closely meets the needs of the current simulation framework in a number of ways:

- Simplification – the new model interface specification eliminates the more obscure and infrequently used features of CAPE, making it more accessible to potential model developers
- Generalization – the new interface removes the specificity of chemical process to provide a more generic structure
- Enhanced data passing – the new interface provides facilities for passing data beyond the level of simple scalars to downstream models (a CAPE-Open limitation)

**The development of the model interface (in the form of a CORBA IDL – Appendix A) represents the completion of an important milestone for the last quarter.**

Integrating new models into the framework will require the following procedure be followed:

- The developer should start with a template to facilitate constructing the component
- The template will provide the necessary CORBA interfaces required for framework integration and communication
- The target model can be wrapped with the compiled IDL interface code – this will define how model inputs are set, execution is controlled and how results are retrieved
- The component source code is compiled into a DLL/shared library
- A corresponding UI for the model is generated using a WxWindows template
- The UI is compiled into a DLL/shared library compatible with the core framework UI

Current Component Model Development Status

Software engineers from REI and CMU have begun the process of wrapping the core computational model from the CMU Vision21 planner software. Thus far, no major difficulties have been encountered. It should be noted that eventually we will be extracting the individual models from the CMU software to provide better integration with the framework. This task will begin during the next performance period.

While the CMU Vision 21 Planner will provide a wide range of fast running component models, we will also port the detailed computational models which exist in REI's current Vision21 workbench. The combination of CMU's and REI's models within the virtual engineering-based framework will allow for a hierarchy of different models to be used for a given component, based on the level of detail needed for a simulation.

# Task 3 – Framework Enhancement - Modeling

This task involves the enhancement of the models contained within our original IGCC framework. Targeted items are improvements to the gasifier models, a greater range of models for gas clean up and metals (mercury) capture and collaborations for benchmarking reduced order models. All improved models will be integrated into the enhanced framework. In the following we summarize recent efforts and highlight future plans.

**Entrained Flow Gasifier**

The gasifier is a key element to any Integrated Gasification Combined Cycle (IGCC) plant because it converts a solid fossil fuel into a more environmentally attractive syngas. Hence, within this project we have put significant effort in to creating advanced gasifier models with capabilities not available in models described in the open literature. Two aspects of the gasifier models we plan to improve in GFY2004 are (1) intrinsic kinetics for coal gasification and (2) models for estimating soot and tar generation. The intrinsic kinetics work is largely completed and has focused on an approach for implementing intrinsic kinetics in a computationally efficient manner within our gasifier models. Provided in Appendix B is a comprehensive description of this work effort. The planned effort for soot/tar modeling will focus on integrating available soot/tar generation/destruction sub-models into our entrained flow gasifier models and will be performed later in GFY2004.

*Intrinsic Kinetics for Coal Gasification*

The heterogeneous reaction kinetics that describe coal gasification processes are important due to their direct impact on calculations performed to estimate gasifier size, expected carbon conversion and possible char recycle requirements. The wide range of conditions that exist in a commercial scale gasifier makes it difficult to apply a simple correlation, such as global kinetic parameters, to describe the competing effects on reactions from oxygen-firing, elevated operating pressure and small particle size. The impact of elevated system pressure (20-80 bar) shifts the coal reactions toward the diffusion–limited regime. In contrast, oxygen firing and small particle size shifts the reaction back toward the kinetically controlled regime. In addition, peak temperatures in an oxygen-fired gasifier can be very high, leading to low reactivity chars in the late stages of burning, which can shift the reaction mode to the chemical kinetics controlled regime. To accurately describe the mixed reaction mode that occurs in the gasifer, a more fundamental and mechanistic approach is needed. The approach we have pursued uses detailed intrinsic kinetics coupled with a pore diffusion model. The intrinsic kinetics are based on the active surface area and can be combined with a diffusion model to generate overall reaction rates for combustion and gasification. In addition, the intrinsic kinetics model can be extended for broader conditions by including pressure/temperature effects on pore development/diffusion. This capability is important for evaluating gasifier performance or exploring potential changes in gasifier operation or design.

The increase in computational resources required to use such a reaction model is acceptable for a process model of a gasifier. However, the required computational time for such a model would be intractable for a 3D CFD model executing on a workstation in a typical engineering office. Hence, our approach has been to develop a kinetic pre-processor that accounts for the details of

the heterogeneous reaction under gasifier specific conditions and generates kinetic parameters that can be directly used in a typical two phase, reacting CFD code.

Within this project, a literature survey on oxidation/gasification kinetics including devolatilization has been performed and relevant features in determining the rates examined. Based on the survey, a kinetic pre-processor (*PREKIN*) was developed that includes various processes such as devolatilization, intrinsic kinetics of char oxidation/gasification, thermal annealing, ash encapsulation, and pore diffusion. *PREKIN* generates kinetic parameters for a given range of temperatures and pressures that can be used directly in our process and CFD based gasifier models. Preliminary results from the application of the *PREKIN*-generated kinetics emphasize the importance of the accurate description of the heterogeneous kinetics in a gasifier. The pre-processor uses standard fuel (coal) properties, intrinsic kinetics data and an optimization routine to generate the global kinetics used by the REI models.

A comprehensive description of the work effort highlighted above is provided in Appendix B.

Moving forward, in GFY2004 REI will continue to collaborate with Prof. Terry Wall and Prof. David Harris (Collaborative Research Center for Coal and Sustainable Development [CCSD] in Australia) on intrinsic kinetics for coal gasification. The CCSD has an internal project to obtain intrinsic kinetic data for coal gasification from a pilot scale gasifier system. Through our Memo of Understanding (MOU) with the CCSD, REI will work with the CCSD to benchmark our models against data being collected by the CCSD.

*Soot/Tar Models for Coal Gasification*

Soot formation from gasification conditions plays an important role in radiative heat transfer in gasifiers. Likewise, tar formation imposes a limit on the oxygen-carbon ratios that can be used to operate a gasifier. At present, our gasifier model calculates local soot concentrations from a correlation, but tar formation is not estimated. In GFY2004, we plan to implement the Brown and Fletcher soot model [Brown and Fletcher, 1998] into our gasifier models. This soot model is comprised of three transport equations for tar mass fraction, soot mass fraction, and soot number density. Coal-derived soot is assumed to form only from tar. Tar evolution will be calculated from Lagrangian particle phase equations that use the Chemical Percolation Devolatilization (CPD) model to determine devolatilization rates and tar yields. The CPD model describes the devolatilization behavior of a rapidly heated coal based on the chemical structure measured by 13C NMR. Through other DOE funded projects soot and tar models have previously been incorporated into the REI coal combustion (not gasification) simulation tools [Shim et al, 2003]. Hence, the cost to this project to integrate the improved soot and tar models into our coal gasification models will be minor.

**Syngas Cleanup**

Within this sub-task, we plan to enhance our available models for tail-end clean up processes contained in the plant simulation framework. In particular, we will focus on models for mercury capture and $CO_2$ removal. Where feasible, we plan to build upon and leverage models previously developed under DOE funding, such as those contained in the CMU IECM, Carbon Management and Vision 21 Planner tools. In the following we highlight our plans for mercury capture.

*Mercury Capture*

Mercury emissions controls are likely to be imposed on the current fleet of coal-fired utility boilers in the U.S. Therefore, it is important that emerging technologies for power generation, like gasification systems, be able to meet the expected emission limits. Given the current state of knowledge, the best way to implement systems for removing mercury is through integration with a cold gas clean up system, as for example, the use of activated carbon beds documented by [Ghani et al, 2003], [Steele et al, 2003].

The goals of this work are

- to identify the relevant chemical speciation of mercury in gasifiers;
- to survey the existing data on emissions and control and;
- to implement a simple fixed bed sorbent model for cold-end mercury capture.

The result of this work will be the ability to predict mercury concentrations in the gas and condensed phases in the gasification system.

To start the analysis, the literature will be surveyed for appropriate mercury data. There is relatively little data on trace metal partitioning in gasifier streams. Figures 5 and 6 show partitioning of trace elements among gasifier streams with and without particulate recycle in the PRENFLO (1 stage, dry feed) gasifier [Hufen, 1990]. As expected, from conventional boilers Hg is found almost entirely in the raw gas. Without particulate recycle, a small fraction of Hg is found in the particulate phase, possibly due to adsorption on char downstream of the gasifier. For comparison, data on the semi-volatile trace elements are shown; note that only a fraction of these elements are found in the syngas. Some of these elements (notably Arsenic (As) and Selenium (Se)) might be expected to be collected in the cold gas clean-up system. Thus, the operation of the gasifier affects the partitioning of the more volatile trace metals between solid and gaseous phases in the raw syngas.

Work in the next quarter will concentrate on identifying the forms of mercury that are likely to occur at different locations in the gasifier.

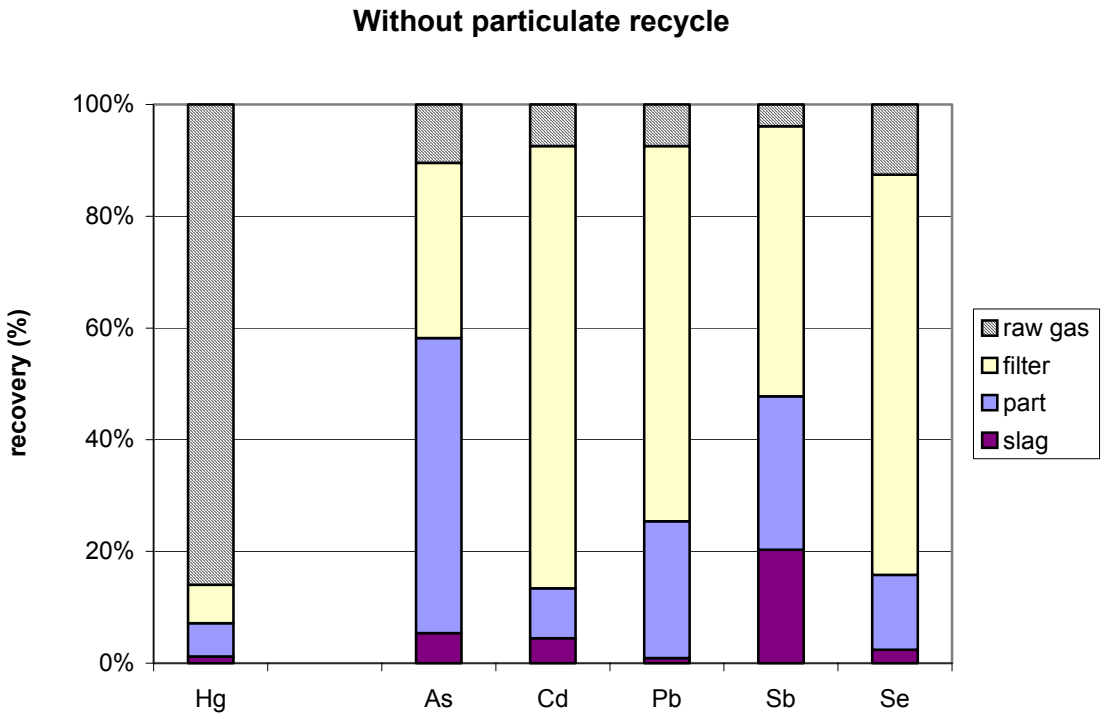


Figure 5. Partitioning of trace metals in the PRENFLO gasifier without particulate recycle.

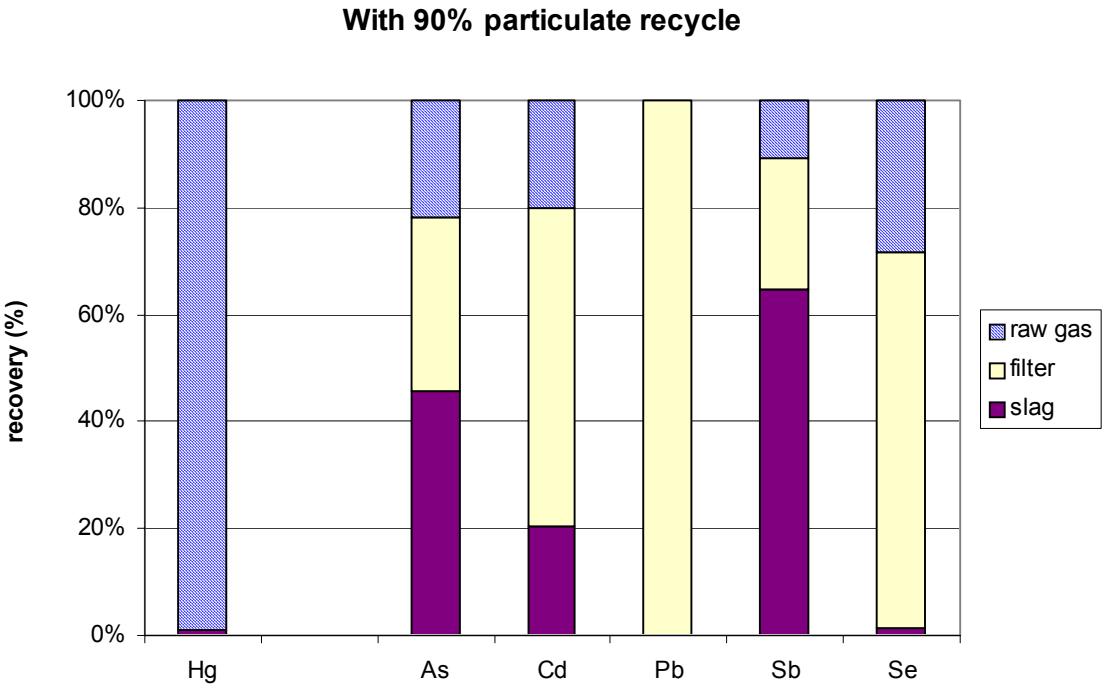


Figure 6. Partitioning of trace metals in the PRENFLO gasifier with 90% particulate recycle.

# Results and Discussion

As discussed in previous quarterly reports, REI has developed a process flow sheet model for entrained flow gasifiers. The model is a "reactor" model that includes equilibrium gas phase reactions, enthalpy balances, a submodel that calculates the carbon combustion efficiency for chars of different reactivity, and a quench model that allows for the reactions between the exit of the gasifier and the temperature at which the reactions are quenched. As described in previous reports, the model has been found to give gas compositions and cold gas efficiencies in relatively good agreement with the limited data in the literature. Recently, a series of parametric studies have been carried out to further study the effects of heat loss, gasifier pressure and variations in slurry concentration and reactor length on the cold-gas efficiency, with the hope of benchmarking the model against qualitative information on gasifier design and performance. In addition, we have investigated a procedure for calculating oxygen/fuel, steam/fuel ratio, and reactor length for use in rapid evaluations of gasifier performance or as inputs to CFD calculations to address a number of gasifier issues that cannot be addressed by the process model. The results of these studies are described below.

*Impact of Gasifier Syngas Quench*

The syngas exiting the gasifier can be cooled at different rates depending upon the design of the process. Mechanisms of cooling, listed in order of decreasing cooling rate, include injection of recycled cooled syngas, firetube heat exchangers, heat-exchange platens, and radiant coolers. The temperature at the exit plane of a single-stage gasifier is high enough that reactions will continue until they are quenched. The result of this cooling on the gas composition is to increase the concentrations of $CO_2$ and $H_2$ at the expense of those of CO and $H_2O$. The concentration profiles of the $CO_2$ concentration as a function of time from the exit of the gasifier are shown for three cooling rates in Figure 7. The cooling rate was kept constant down to a temperature of 500 K and the temperature maintained constant after that. It can be seen that the concentration of $CO_2$ (and, not shown here, those of $H_2$, $H_2O$, and CO) approaches an asymptotic value that increases as the cooling rate decreases. These asymptotic values can be used to calculate an effective water-gas-shift equilibrium constant. For an infinite cooling rate, the water-gas-shift equilibrium is equilibrated at the exit temperature. As the cooling rate decreases, the temperature at which the water-gas shift equilibrium reaction ($CO + H_2O = CO_2 + H_2$) is equilibrated in the product syngas also decreases. This is evident in Figure 8, in which the water-gas shift equilibrium constant of the quenched product gases is shown as a function of cooling rate for gasifier outlet temperatures of 1311, 1500, and 1687 K. No reactions occur downstream of the reactor for an exit temperature of 1311 K (representative of the exit temperature of a two-stage gasifier), as evidenced by the constancy of the equilibrium constant. As the exit temperature is increased, however, significant reactions occur at the lower cooling rates, as seen for exit temperatures of 1500 and 1687 K (representative of the range of exit temperatures of single-stage gasifiers). The lower cooling rates of 100 K/s may represent values in radiant coolers. The values on the order of 500 K/s are representative of cooling in firetubes. Higher values on the order of 30000 K/s can be obtained by rapid mixing with recycled cooled syngas.

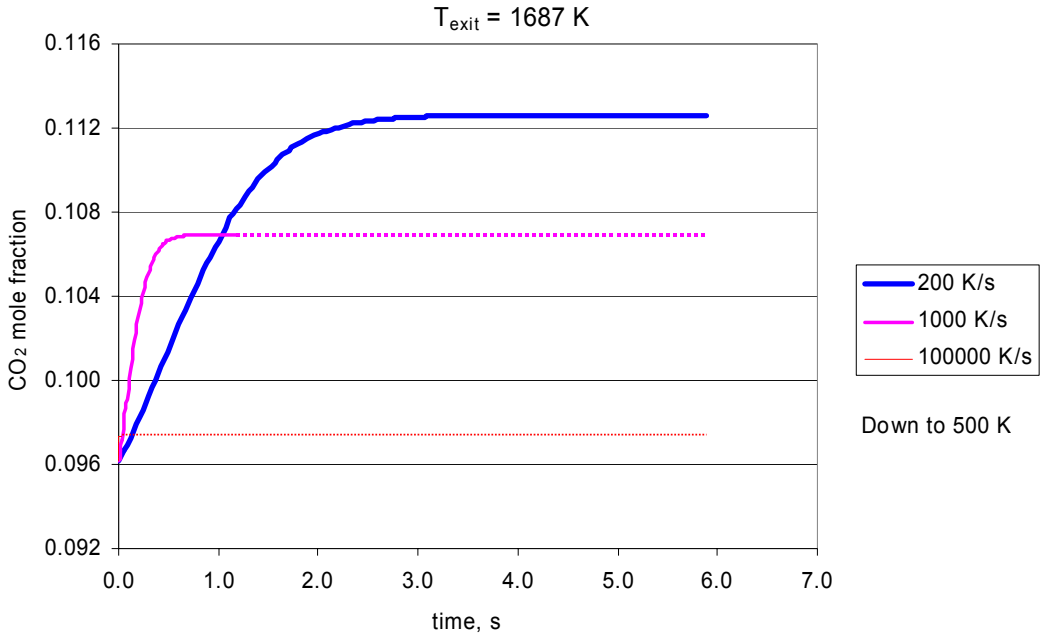


Figure 7. Effect of quench rate on variation of $CO_2$ concentration.

The frozen water-gas shift equilibrium constant calculated from the frozen gas compositions is shown in Figure 8. The constant can be translated into a temperature at which the water-gas-shift reactions are effectively frozen. The results of doing so are shown in Figure 9, where the equilibration temperature is shown as a function of the cooling rate of the gasifier product gases, for gasifier exit temperatures of 1311, 1500, and 1687 K. It can be seen that as the cooling rate is increased to levels in excess of 30000 K/s the gas composition is quenched at levels close to that at the gasifier outlet. As the cooling rate is decreased, the temperature drop before the syngas composition freezes increases. A rule of thumb for the differential between the exit and frozen temperatures that is used in the industry (Holt, 2001) is 85 K, but it can be seen that this drop is a function of both the gasifier exit gas temperature and the quench system design.

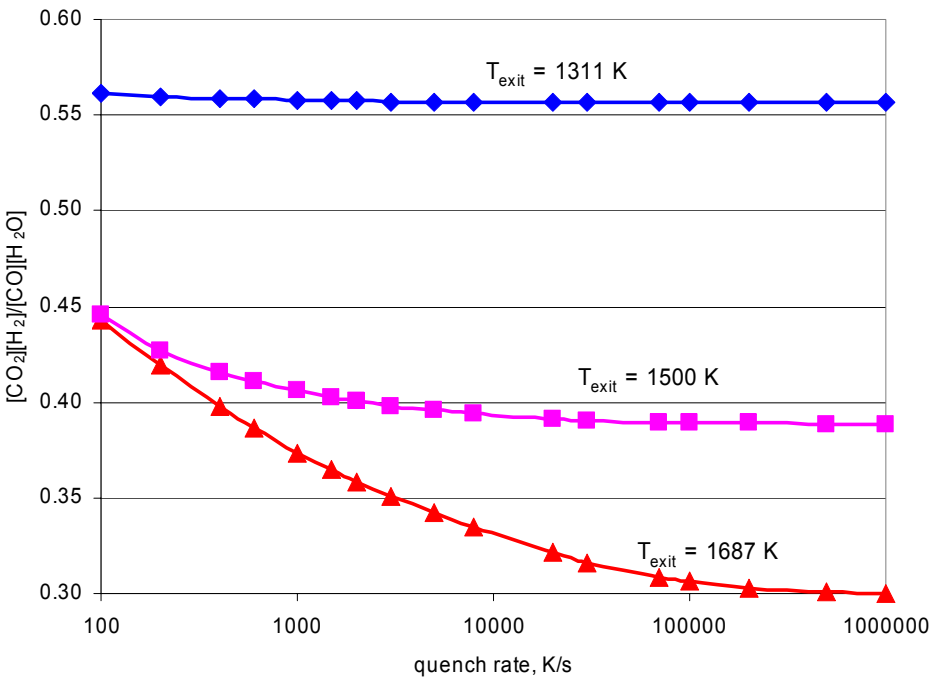


Figure 8. Effect of quench rate on water-gas shift equilibrium constant for syngas produced in gasifiers with exit temperatures of 1311, 1500 and 1687 K.

It should be pointed out that the impact on gas composition and cold gas efficiency due to the temperature differentials is small. Results for the gas composition for cooling rates of 100 K/s, 3000 K/s and 100000 K/s are shown in Table 1. The simulations were carried out for conditions corresponding to a dry-fed, oxygen-blown, Shell gasifier processing 26.88 kg/s of Illinois #5 coal. The coal is pulverized and pre-dried to less than 2 percent moisture, and then transported to the gasifier by high-pressure nitrogen. Oxygen of 95 percent purity is supplied by the Air Separation Unit. Over the wide range of quench rates studied, measurable differences in the gas concentrations of $H_2O$ and $CO_2$ are seen, but the absolute changes are small enough not to have a significant impact on the syngas heating value or cold gas efficiency. The effect of syngas quench rate on the water-gas shift equilibrium can therefore be considered to have a second order effect.

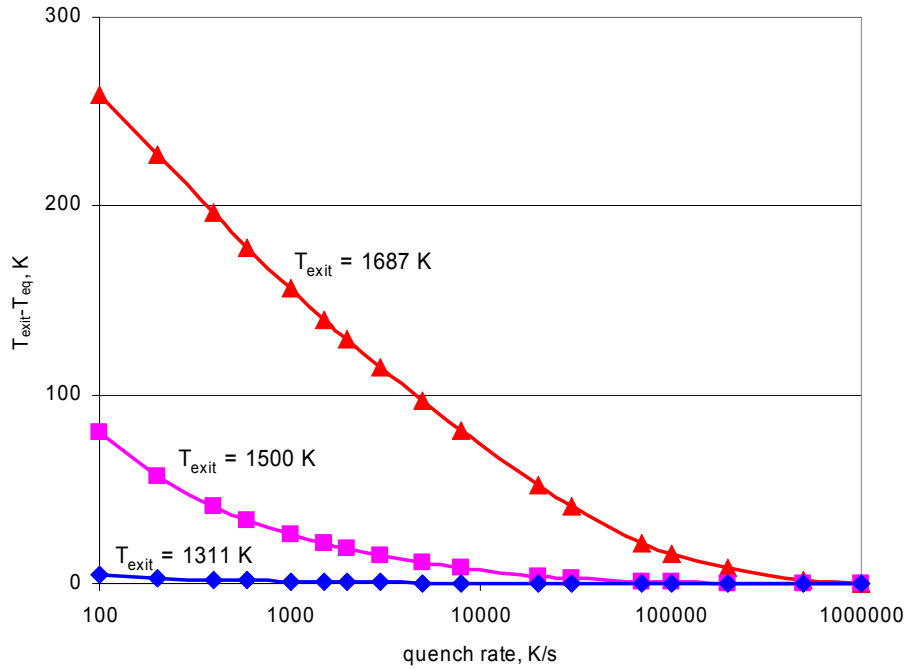


Figure 9. Difference between gasifier exit temperature, $T_{exit}$, and the water-gas shift equilibrium temperature, $T_{eq}$, for gasifier exit temperatures of 1311, 1500 and 1687 K.

Table 1. Impact of quench rate on gas composition and heating value.

| | **100 K/s** | **3000 K/s** | **100000 K/s** | **Gasifier exit** |
|---|---|---|---|---|
| Exit Temperature, K | 500 | 500 | 500 | 1708 |
| Carbon Conversion, % | 99.1 | 99.1 | 99.1 | 99.1 |
| Mole Fraction: CO | 0.6100 | 0.6160 | 0.6170 | 0.6173 |
| $H_2$ | 0.2340 | 0.2280 | 0.2270 | 0.2264 |
| $H_2O$ | 0.0418 | 0.0476 | 0.0491 | 0.0492 |
| $CO_2$ | 0.0465 | 0.0407 | 0.0392 | 0.0391 |
| $CH_4$ | 0.00003 | 0.00004 | 0.00004 | 0.00004 |
| $H_2S$ | 0.0121 | 0.0121 | 0.0119 | 0.0121 |
| COS | 0.0011 | 0.0011 | 0.0010 | 0.0011 |
| Ar | 0.0105 | 0.0105 | 0.0105 | 0.0105 |
| $N_2$ | 0.0439 | 0.0439 | 0.0439 | 0.0439 |
| HHV of Syngas, MJ/kg | 11.07 | 11.08 | 11.09 | 11.08 |
| Cold-Gas Efficiency (LHV), % | 79.4 | 79.5 | 79.5 | 79.5 |

*Parametric Studies*

The Process Model can be used to study the effects of a wide range of parameters, such as coal or other solid fuel composition, reactor volume, pressure, oxygen/carbon ratio, steam/carbon ratio, wall heat extraction, dry versus slurry feed and feed preheat. Selected parametric studies have been conducted to show the importance of different parameters. The base case is for a gasifier operating at 30 atmospheres, firing an Illinois #6 coal, a coal slurry feed with 65% slurry concentration, a slurry temperature of 298 K, a coal flow rate of 25.8 kg/s (about 2400 tpd), an oxidant (95%$O_2$, 5%$N_2$) flow rate of 13.9 kg/s (about 1345 tpd) and a temperature of 298 K, and a heat extraction rate of 100 kW/m$^2$. In running the parametric analysis one choice is to vary the parameters keeping the gasifier volume fixed, which is what is expected for changing the process variables for an existing gasifier. However, for the present case the parameter variation was so large that it was decided to vary the volume to keep the carbon conversion efficiency constant, since so many of the observed changes were a consequence of the effect of the parameters on carbon conversion efficiency.

The effect of the heat extraction on gasifier performance for the case of fixed carbon conversion efficiency is seen in Table 2. The range of heat extraction rates was varied from adiabatic (0) to a value of 200 kW/m$^2$ (the high end of a membrane wall heat transfer rate). It can be seen that the extraction rates are a small fraction of the total heat input so that the changes in gas composition, gas heating value, and cold gas efficiency are correspondingly small. The change in gas temperature of 60 ºC is large enough to affect the kinetics of gasification so that the impact on carbon conversion efficiency could be significant, as will be shown later.

Table 2. Effect of heat extraction on gas composition, exit temperature, and cold gas efficiency (carbon conversion maintained constant).

| Heat Extraction, kW/m$^2$ | 0 | 50 | **100** | 150 | 200 |
|---|---|---|---|---|---|
| | | | | | |
| Exit Temperature, K | 1683 | 1668 | 1653 | 1638 | 1623 |
| Thermal Input, MW | 700.6 | 700.6 | 700.6 | 700.6 | 700.6 |
| Thermal Output, MW | 526.7 | 526.6 | 526.4 | 526.3 | 526.2 |
| Carbon Conversion, % | 97.9 | 97.9 | 97.9 | 97.9 | 97.9 |
| Mole Fraction: CO | 0.3529 | 0.3519 | 0.3509 | 0.3499 | 0.3489 |
| $H_2$ | 0.2487 | 0.2497 | 0.2506 | 0.2516 | 0.2526 |
| $H_2O$ | 0.2626 | 0.2616 | 0.2606 | 0.2596 | 0.2586 |
| $CO_2$ | 0.1118 | 0.1127 | 0.1137 | 0.1147 | 0.1157 |
| $CH_4$ | 0.00001 | 0.00001 | 0.00002 | 0.00002 | 0.00002 |
| $H_2S$ | 0.00653 | 0.00654 | 0.00654 | 0.00654 | 0.00655 |
| COS | 0.00032 | 0.00032 | 0.00031 | 0.00031 | 0.00031 |
| $N_2$ | 0.0165 | 0.0165 | 0.0165 | 0.0165 | 0.0165 |
| Syngas Flow Rate, kg/s | 59.92 | 59.92 | 59.92 | 59.92 | 59.92 |
| HHV of Syngas, MJ/kg | 8.80 | 8.79 | 8.79 | 8.79 | 8.79 |
| CGE (HHV), % | 75.2 | 75.2 | 75.1 | 75.1 | 75.1 |

A similar result is seen on the impact of pressure in Table 3. The volume of the reactor was decreased as the pressure was increased to maintain a constant carbon conversion efficiency. This results in a fraction of the energy input being lost to the wall, but since the heat loss does not significantly influence the gasifier performance this is not significant. Furthermore, the major equilibrium reactions such as the water-gas shift do not involve a volume change on reaction so that the effect of pressure on the gas phase composition is negligibly small.

Table 3. Effect of pressure on gasifier performance for a fixed carbon conversion.

| Pressure, atm | 20 | **30** | 55 | 75 | 100 |
|---|---|---|---|---|---|
| | | | | | |
| Exit Temperature, K | 1653 | 1653 | 1653 | 1654 | 1654 |
| Thermal Input, MW | 700.6 | 700.6 | 700.6 | 700.6 | 700.6 |
| Thermal Output, MW | 526.4 | 526.4 | 526.4 | 526.4 | 526.3 |
| Carbon Conversion, % | 97.9 | 97.9 | 97.9 | 97.9 | 97.9 |
| Mole Fraction: CO | 0.3509 | 0.3509 | 0.3509 | 0.3509 | 0.3508 |
| $H_2$ | 0.2507 | 0.2506 | 0.2505 | 0.2504 | 0.2502 |
| $H_2O$ | 0.2606 | 0.2606 | 0.2607 | 0.2607 | 0.2608 |
| $CO_2$ | 0.1137 | 0.1137 | 0.1137 | 0.1137 | 0.1138 |
| $CH_4$ | 0.00001 | 0.00002 | 0.00005 | 0.00010 | 0.00018 |
| $H_2S$ | 0.00654 | 0.00654 | 0.00654 | 0.00654 | 0.00654 |
| COS | 0.00031 | 0.00031 | 0.00031 | 0.00032 | 0.00032 |
| $N_2$ | 0.0165 | 0.0165 | 0.0165 | 0.0165 | 0.0165 |
| Syngas Flow Rate, kg/s | 59.92 | 59.92 | 59.92 | 59.92 | 59.92 |
| HHV of Syngas, MJ/kg | 8.79 | 8.79 | 8.79 | 8.79 | 8.79 |
| CGE (HHV), % | 75.1 | 75.1 | 75.1 | 75.1 | 75.1 |

The effect of slurry concentration in Table 4 is dramatic. The impact of the water mass on the temperature in the gasifier is enormous. The variations provided here are unrealistic but make the point on the decrease in gasifier temperature on exit and the increase in cold gas efficiency with increases in water content.

The last parametric variation was that of carbon conversion efficiency, varied here by changing the gasifier length, as shown in Table 5. Again, the range of parameters is not realistic but makes the point of how sensitive the performance of the gasifier is to changing carbon conversion.

From these parametric studies it can be seen that the parameters of greatest importance are the pressure because of the effect of gasifier volume, the slurry concentration because of the impact of moisture on temperature and the gasifier performance, and any parameter (furnace length, oxygen concentration, furnace temperature) that affects the carbon conversion efficiency. Because of the interdependence of the parameters it is difficult to draw conclusions from varying one parameter at a time. The next section provides a parametric study that shows the impact of multiple parameters on performance and illustrates how this can be used to hone in on preferred operating conditions.

Table 4. Effect of slurry concentration on gasifier performance for a fixed carbon conversion.

| Slurry Concentration, % | 30 | 48 | **65** | 83 | 100 |
|---|---|---|---|---|---|
| $H_2O$ Flow Rate, kg/s | 60.244 | 27.971 | **13.903** | 5.288 | 0 |
| | | | | | |
| Exit Temperature, K | 895 | 1222 | 1653 | 2093 | 2475 |
| Thermal Input, MW | 700.6 | 700.6 | 700.6 | 700.6 | 700.6 |
| Thermal Output, MW | 559.3 | 546.5 | 526.4 | 511.9 | 503.6 |
| Carbon Conversion, % | 97.9 | 97.9 | 97.9 | 97.9 | 97.9 |
| Mole Fraction: CO | 0.0181 | 0.1946 | 0.3509 | 0.4832 | 0.5899 |
| $H_2$ | 0.1255 | 0.2700 | 0.2506 | 0.2379 | 0.2301 |
| $H_2O$ | 0.5890 | 0.3430 | 0.2606 | 0.1764 | 0.1019 |
| $CO_2$ | 0.2014 | 0.1705 | 0.1137 | 0.0734 | 0.0432 |
| $CH_4$ | 0.05178 | 0.00289 | 0.00002 | 0.00000 | 0.00000 |
| $H_2S$ | 0.00398 | 0.00531 | 0.00654 | 0.00758 | 0.00830 |
| COS | 0.00002 | 0.00012 | 0.00031 | 0.00057 | 0.00084 |
| $N_2$ | 0.0096 | 0.0130 | 0.0165 | 0.0198 | 0.0225 |
| Syngas Flow Rate, kg/s | 106.26 | 73.98 | 59.92 | 51.30 | 46.01 |
| HHV of Syngas, MJ/kg | 5.27 | 7.39 | 8.79 | 9.98 | 10.95 |
| CGE (HHV), % | 79.8 | 78.0 | 75.1 | 73.1 | 71.9 |

Table 5. Effect of carbon conversion on gasifier performance.

| Gasifier Length, m | 0.029 | 0.1 | 1.1 | **5.5** | 9.9 |
|---|---|---|---|---|---|
| | | | | | |
| Exit Temperature, K | 2642 | 2387 | 1862 | 1653 | 1596 |
| Thermal Input, MW | 700.6 | 700.6 | 700.6 | 700.6 | 700.6 |
| Thermal Output, MW | 68.3 | 247.5 | 447.9 | 526.4 | 541.1 |
| Carbon Conversion, % | 36.3 | 64.0 | 88.7 | 97.9 | 99.6 |
| Mole Fraction: CO | 0.0185 | 0.2146 | 0.3254 | 0.3509 | 0.3536 |
| $H_2$ | 0.0064 | 0.0989 | 0.2079 | 0.2506 | 0.2599 |
| $H_2O$ | 0.6168 | 0.4797 | 0.3186 | 0.2606 | 0.2486 |
| $CO_2$ | 0.2730 | 0.1792 | 0.1235 | 0.1137 | 0.1138 |
| $CH_4$ | 0.00000 | 0.00000 | 0.00000 | 0.00002 | 0.00003 |
| $H_2S$ | 0.00000 | 0.00102 | 0.00623 | 0.00654 | 0.00659 |
| COS | 0.00000 | 0.00009 | 0.00035 | 0.00031 | 0.00031 |
| $N_2$ | 0.0213 | 0.0195 | 0.0172 | 0.0165 | 0.0164 |
| Syngas Flow Rate, kg/s | 47.33 | 52.98 | 58.03 | 59.92 | 60.27 |
| HHV of Syngas, MJ/kg | 1.44 | 4.67 | 7.72 | 8.79 | 8.98 |
| CGE (HHV), % | 9.8 | 35.3 | 69.9 | 75.1 | 77.2 |

*Selecting Operating Conditions*

The comparisons with the data from pilot and demonstration gasification plants were carried out for oxygen and steam flow rates that had been specified. The question remains of how such conditions are selected. The criteria that are generally proposed are that the gasifier should be operated at a sufficiently high temperature to maintain the slag flowing, the cold gas efficiency be maximized, that the carbon conversion be high, and that the temperatures be moderated to protect the refractory.

The flowing characteristics of a slag is given by the critical viscosity for the slag, corresponding to the point at which the viscosity becomes non-Newtonian and corresponds to the point at which there is a change in slope of a plot of log(viscosity) vs. (1/T), and is of order 25 Pa·s. Correlations have been provided for the critical viscosity of ashes of different iron content by the CRC for Black Coal Utilization (Patterson et al., 2001). For slags with an iron content of less than 15%, temperature corresponding to the critical viscosity is given by:

$$T_{cv}(K) = 3452 - 519.2\alpha + 74.5\alpha^2 - 67.8\beta + 0.86\beta^2$$

where $\alpha = SiO_2 / Al_2O_3$ and $\beta = Fe_2O_3 + CaO + MgO$ and $SiO_2 + Al_2O_3 + Fe_2O_3 + CaO + MgO = 100$, and where concentrations are expressed in weight percent. The result of applying the correlation to a few of the coals above is given in Table 6. The ash composition was used to obtain $T_{CV}$ here; in practice allowance should be made for the differences in composition between the slag and the carryover ash in making such calculations. It can be seen that the critical viscosity is low for the alkaline slags and high for high silica and alumina slags. In the following calculations a maximum gasifier exit temperature of 1627 K was chosen to protect the refractories.

The optimization for oxygen/fuel and $H_2O$/fuel can now be carried out. The first set of calculations will be for a slurry-fed gasifier with the baseline coal of the Illinois #6 coal considered above. The $H_2O$/coal(dry-ash-free) and $O_2$/coal(daf) were varied systematically for a fixed carbon-burnout efficiency of 98 percent and the results on gasifier exit temperature, cold gas efficiency, and the concentrations (mole percent) of CO, $CO_2$, $H_2$, and $H_2O$ are presented in Figure 10-15. Increasing $O_2$/coal(daf) at a fixed $H_2O$/coal (daf) or decreasing $H_2O$/coal(dry-ash-free) at a fixed $O_2$/coal(daf) results in a systematic increase in temperatures as shown in Figure 10. The isotherm for 1627 K is highlighted to show the approximate demarcation between the slagging and nonslagging regimes. The operating conditions of interest are therefore to the right of the slagging line, although there clearly is an upper limit on oxygen content before refractory damage becomes an issue. There is a penalty in increasing $H_2O$/coal since this increases the $O_2$/coal ratio needed to achieve slagging. The benefit of varying the water content at a fixed oxygen content is seen in Figure 11. The changes in cold gas efficiency with increasing water content are a trade-off between the

- increase in the chemical energy in the CO and $H_2$ at the expense of the sensible enthalpy, and the

- decrease in the syngas heating value as CO is converted to $CO_2$ ($H_2$ concentration remains approximately constant because of the increase in $H_2O$).

This results in a peaking in the cold gas efficiency (see Figure 11). We would wish to select values of $O_2$/coal(daf) and $H_2O$/coal(daf) that lie on the locus of maximum cold gas efficiency that can be seen in Figure 12 but also be in the slagging region. The conditions close to the knee of the slagging curve provide the desired high cold gas efficiency, and a slagging temperature. The optimum conditions therefore correspond to an $O_2$/coal(daf) of about 0.85 and an $H_2O$/coal(daf) of about 0.05. Also shown on Figure 12 are the operating conditions for the slurry fed Tampa Electric and Cool Water Gasifiers described earlier. The slurry fed gasifiers operate with a $H_2O$/coal(daf) concentration higher than the optimum because of the water in the slurry feed. Holt (2001) has described schemes in which advantages can be taken of both slurry feed (ease of pumping to a high pressure) and dry feed (lower oxygen consumption, higher cold-gas efficiency). In these schemes, the slurry is pumped to pressure, heated, the steam flashed so that it can by-pass the gasifier and the coal then fed dry. The advantages of such a scheme for reducing oxygen use and increasing cold gas efficiency are clear from Figure 12, with the difference in operating conditions for the Tampa Electric Plant and those at the optimum point for a dry feed.

A set of calculations were also carried out for a dry feed with a systematic variation of the steam/coal(daf) and $O_2$/coal(daf) ratios. The results for temperature and cold gas efficiencies, and the concentrations of CO, $CO_2$, $H_2$, and $H_2O$ show similar trends as in Figures 10-15 and are therefore not reported here. Figure 15 shows the combination of oxygen and steam flows required to obtain slagging conditions. Figure 16 shows that the optimum cold gas efficiency is, as before, in the non-slagging regime. The optimum conditions satisfying both the slagging constraint and yielding high cold gas efficiencies are, from Figure 17, an $O_2$/coal(daf) around 0.85 and a steam/coal(daf) around 0.1. Also shown in Figure 17 are the operating conditions from data found in the literature for dry-fed gasifiers. It can be seen that they cluster around the optimum conditions but with a number of the points at higher $O_2$/coal(daf) ratios. This can be explained to a large part by the variation in coal (or coke) compositions. The effect of $O_2$/coal(daf) ratio on the cold gas efficiency, for a fixed steam/coal(daf) is shown in Figure 18 to illustrate that the optimum varies widely, being governed by the O/C ratio in the fuel. In addition, the coals for which the operating conditions are summarized in Figure 17 have a range of temperatures for critical viscosity that also contributes to the spread of the data points.

The above examples illustrate how the contour plots of cold gas efficiency together with the constraint of ash viscosity can be used to select operating conditions for gasifiers and provide input conditions for the more detailed process design optimization using CFD.

Table 6. Temperatures of critical viscosity for different coals.

| wt, % | Illinois #5 | Illinois #6 | Pittsburgh #8 | Drayton | Petcoke | SUFCo | Lemington | Pike County | Falkirk Lignite | Freedom Lignite |
|---|---|---|---|---|---|---|---|---|---|---|
| $SiO_2$ | 53.82 | 57.75 | 47.44 | 53.02 | 39.13 | 52.47 | 53.92 | 57.14 | 49.76 | 46.01 |
| $Al_2O_3$ | 18.62 | 22.92 | 25.28 | 29.33 | 9.94 | 12.74 | 32.14 | 35.07 | 15.42 | 16.76 |
| $Fe_2O_3$ | 21.85 | 15.90 | 21.21 | 8.29 | 15.73 | 8.36 | 5.77 | 5.30 | 5.42 | 8.78 |
| CaO | 4.63 | 2.44 | 4.99 | 8.70 | 24.64 | 22.33 | 7.63 | 1.88 | 18.67 | 21.14 |
| MgO | 1.08 | 1.00 | 1.08 | 0.65 | 10.56 | 4.11 | 0.54 | 0.61 | 10.72 | 7.31 |
| Total | 100 | 100 | 100 | 100 | 100 | 100 | 100 | 100 | 100 | 100 |
| $\alpha$ | 2.89 | 2.52 | 1.88 | 1.81 | 3.94 | 4.12 | 1.68 | 1.63 | 3.23 | 2.75 |
| $\beta$ | 27.56 | 19.33 | 27.27 | 17.64 | 50.93 | 34.79 | 13.94 | 7.79 | 34.82 | 37.23 |
| $T_{cv}$, K | 1358 | 1627 | 1530 | 1828 | 1339 | 1258 | 2012 | 2327 | 1233 | 1255 |

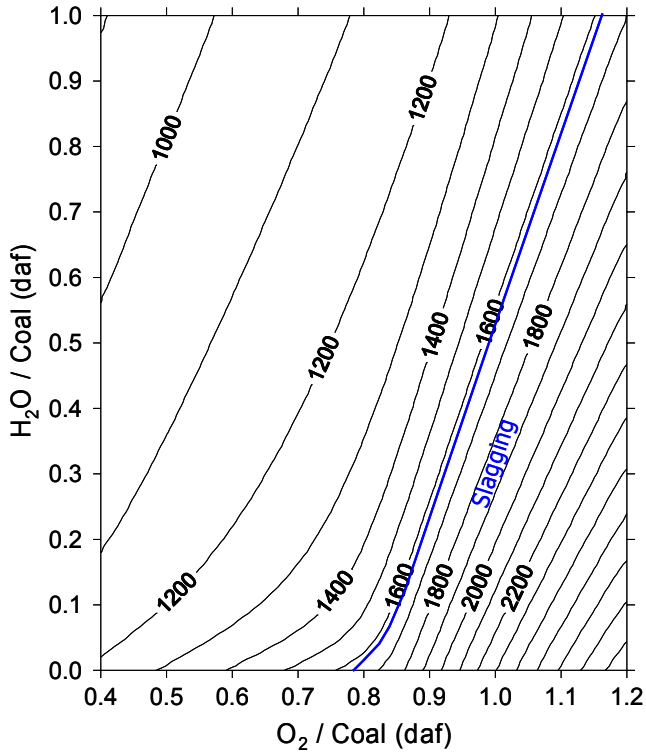


Figure 10. Effect of $H_2O$/coal (daf) and $O_2$/coal (daf) on gasifier exit temperature (K) (single-stage gasifier, 30 atm, Illinois #6 coal, slurry feed), solid line is locus for slagging condition.

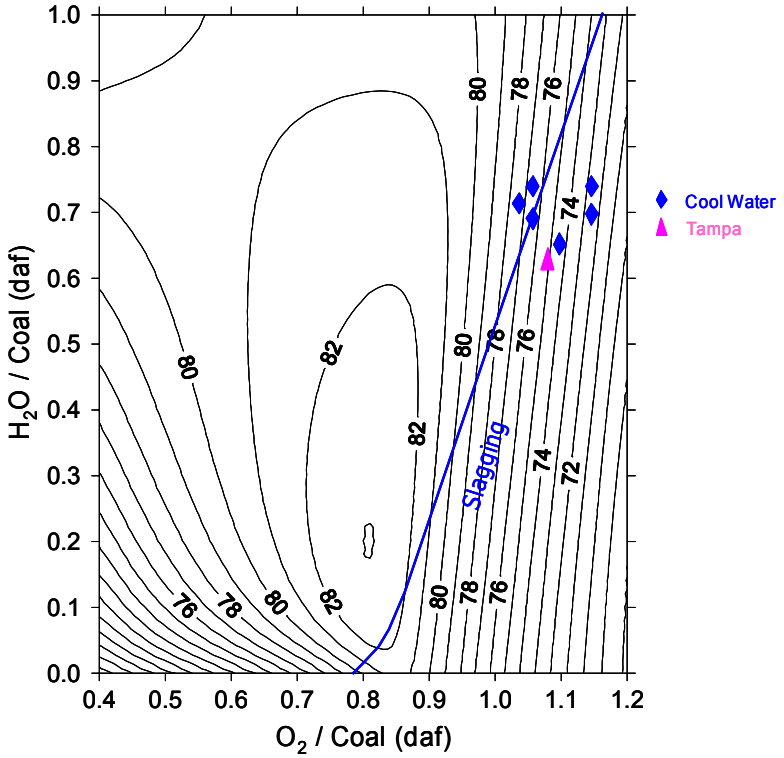


Figure 11. Effect of $H_2O$/coal (daf) and $O_2$/coal (daf) on cold-gas efficiency (%, HHV) (single-stage gasifier, 30 atm, Illinois #6 coal, slurry feed).

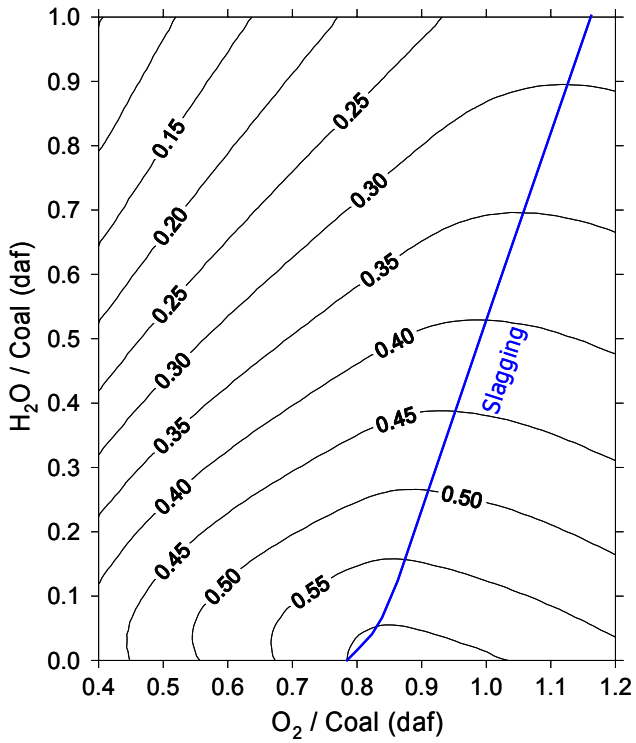


Figure 12. Effect of $H_2O$/coal (daf) and $O_2$/coal (daf) on CO mole fraction (single-stage gasifier, 30 atm, Illinois #6 coal, slurry feed).

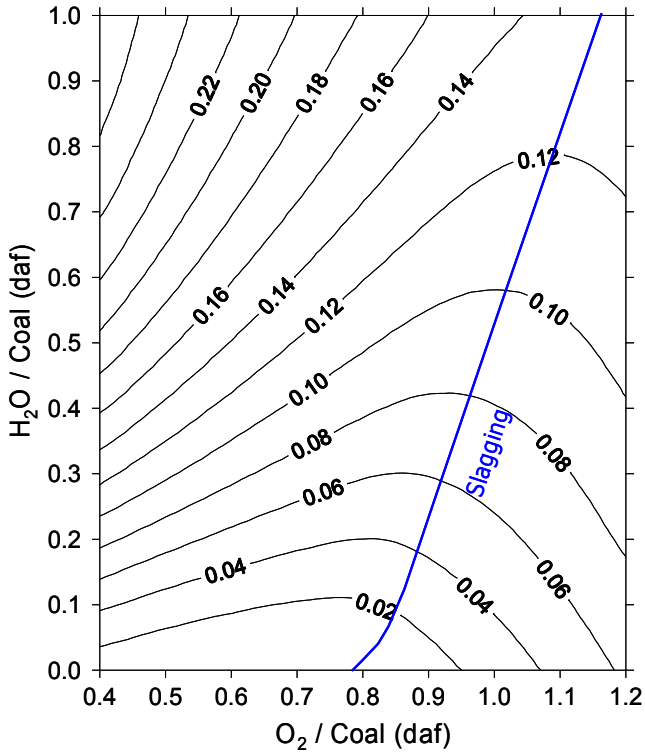


Figure 13. Effect of $H_2O$/coal (daf) and $O_2$/coal (daf) on $CO_2$ mole fraction (single-stage gasifier, 30 atm, Illinois #6 coal, slurry feed).

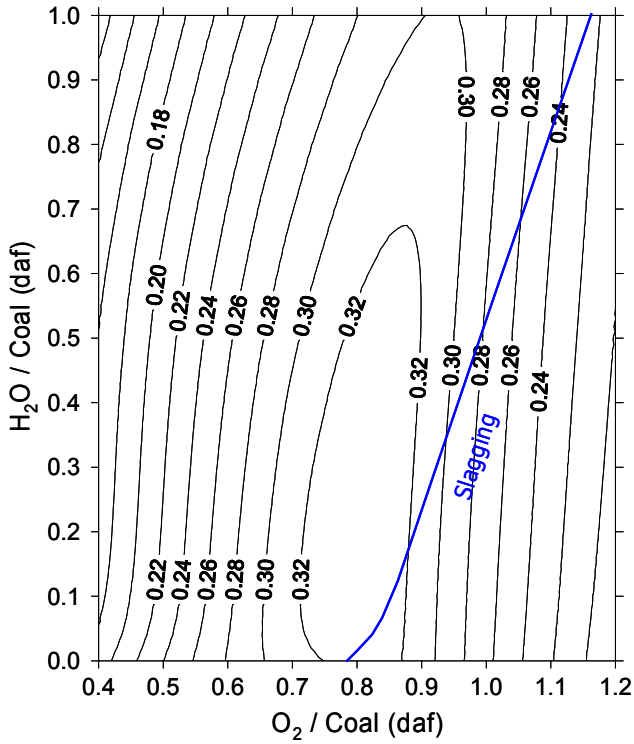


Figure 14. Effect of $H_2O$/coal (daf) and $O_2$/coal (daf) on $H_2$ mole fraction (single-stage gasifier, 30 atm, Illinois #6 coal, slurry feed).

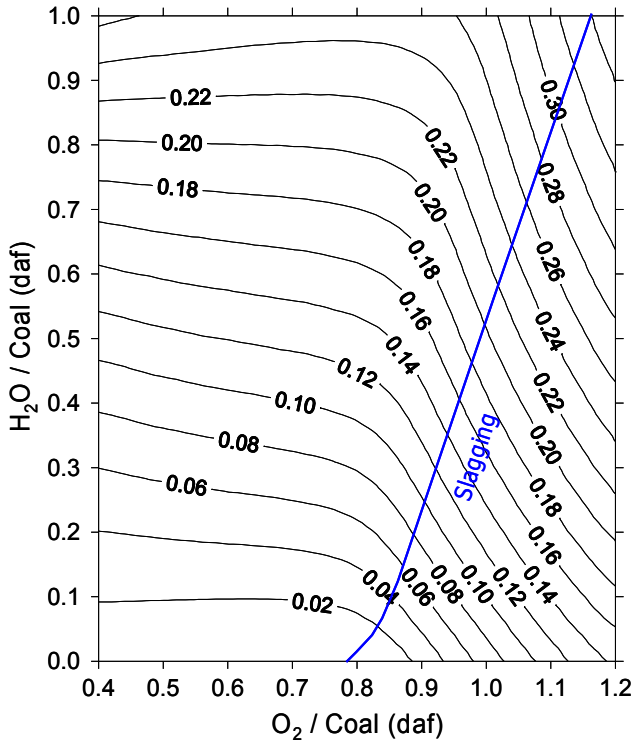


Figure 15. Effect of $H_2O$/coal (daf) and $O_2$/coal (daf) on $H_2O$ mole fraction (single-stage gasifier, 30 atm, Illinois #6 coal, slurry feed).

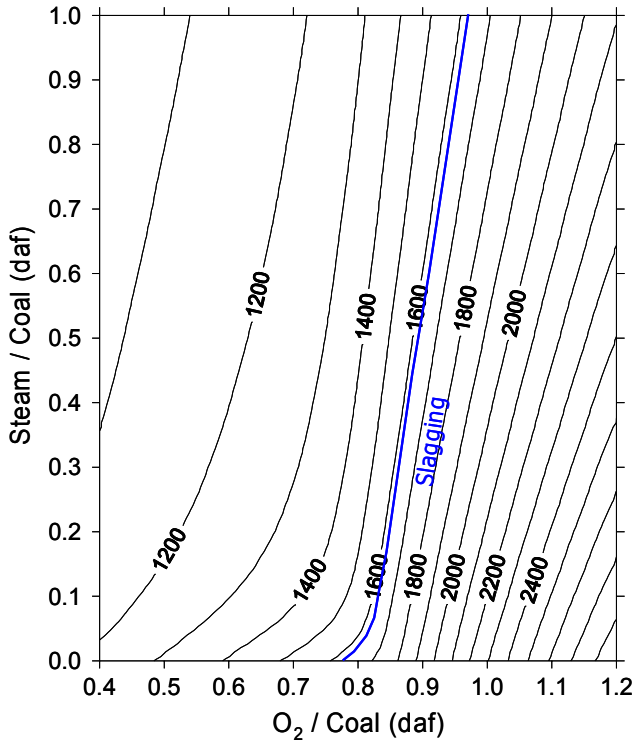


Figure 16. Effect of steam/coal (daf) and $O_2$/coal (daf) on gasifier exit temperature (K) (single-stage gasifier, 30 atm, Illinois #6 coal, dry feed).

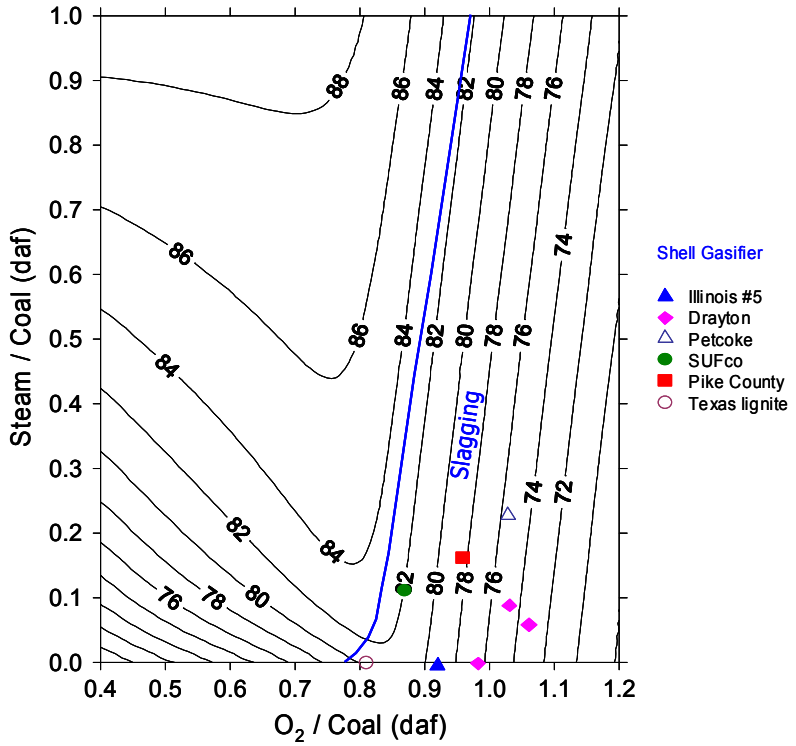


Figure 17. Effect of steam/coal (daf) and $O_2$/coal (daf) on cold-gas efficiency (%, HHV) (single-stage gasifier, 30 atm, Illinois #6 coal, dry feed).

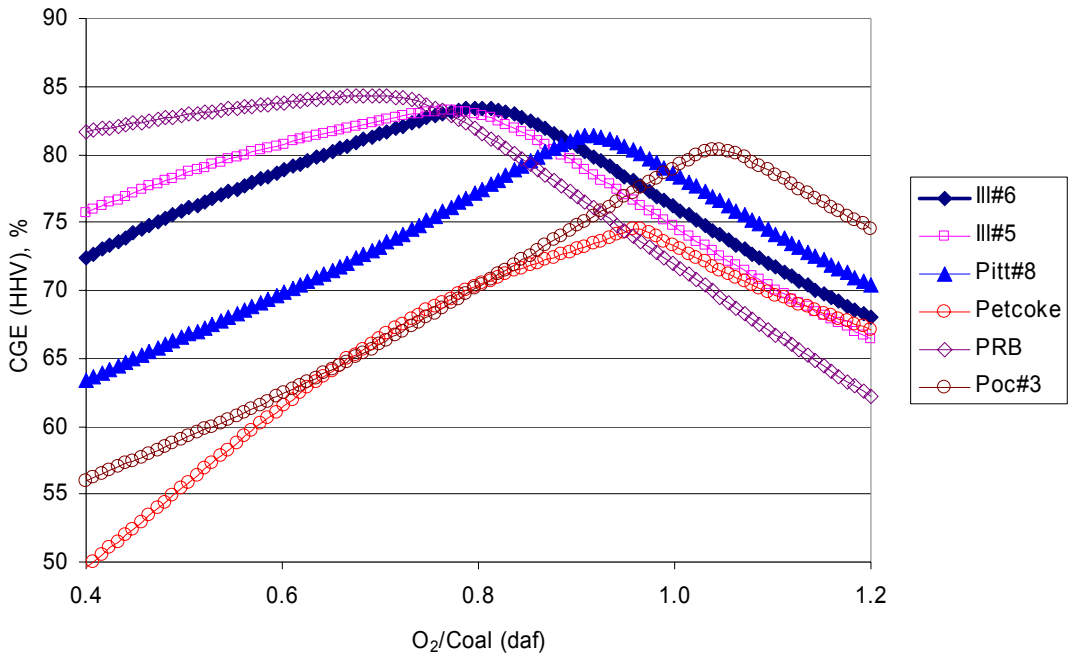


Figure 18. Effect of $O_2$/coal (daf) on cold-gas efficiency for different coal (single-stage gasifier, 30 atm, dry feed, steam/coal (daf) = 0.10).

*Comparison of CFD and Process Model Results*

As described above, we have benchmarked our process model using the limited gasifier data reported in the literature. The process model can be used to provide guidance on selecting gasifier conditions and type for a desired carbon conversion or other output requirements. Table 7 shows the Process Model results using three different gasifier lengths. The gasifier diameter is fixed, by varying the length of the gasifier, different carbon conversions can be achieved due to changes in the residence time of coal particles. Also reported in the table are the net plant power output and the overall plant efficiency calculated using the REI Vision 21 workbench. As expected, as carbon conversion increases, both the cold-gas efficiency and the overall plant efficiency increase. CFD simulations have also been performed using the same conditions as given in Table 7. Results of such simulations are given in Table 8. Clearly, results from both calculations are very similar, especially for the first two cases with shorter gasifiers.

Table 7. Results based on the Process Model.

| | | | |
|---|---|---|---|
| P, psia | 400 | 400 | 400 |
| Particle Size, μm | 39.8 | 39.8 | 39.8 |
| Slurry Temperature, K | 298 | 298 | 298 |
| Water Droplet Size, μm | 25 | 25 | 25 |
| Gasifier Diameter, m | 1.00 | 1.00 | 1.00 |
| Gasifier Length, m | 1.175 | 1.742 | 3.000 |
| Carbon Conversion, % | 90.0 | 95.0 | 99.98 |
| Exit Temperature, K | 1869 | 1754 | 1652 |
| Mole Fraction: CO | 0.3903 | 0.4057 | 0.4200 |
| $H_2$ | 0.2297 | 0.2526 | 0.2744 |
| $H_2O$ | 0.2508 | 0.2200 | 0.1908 |
| $CO_2$ | 0.1048 | 0.0976 | 0.0911 |
| $H_2S$ | 0.0058 | 0.0059 | 0.0060 |
| $CH_4$ | 0.000002 | 0.000007 | 0.000029 |
| COS | 0.000351 | 0.000333 | 0.000318 |
| HCl | 0.000228 | 0.000231 | 0.000235 |
| $N_2$ | 0.0179 | 0.0175 | 0.0170 |
| Syngas Flow Rate, kg/s | 54.77 | 55.77 | 56.78 |
| Syngas Density, kg/m$^3$ | 3.77 | 3.94 | 4.11 |
| LHV of Syngas, Btu/lb | 3360.2 | 3629.1 | 3892.1 |
| HHV of Syngas, Btu/lb | 3788.2 | 4058.2 | 4322.3 |
| Cold-Gas Efficiency (HHV), % | 67.5 | 73.7 | 79.9 |
| Net Plant Power, MW | 290 | 322 | 329 |
| Plant Efficiency (HHV), % | 40.7 | 45.0 | 46.1 |

Table 8. CFD simulation results (same operating conditions as in Table 7).

| | | | |
|---|---|---|---|
| P, psia | 400 | 400 | 400 |
| Particle Size, μm | 39.8 | 39.8 | 39.8 |
| Slurry Temperature, K | 298 | 298 | 298 |
| Water Droplet Size, μm | 25 | 25 | 25 |
| Gasifier Diameter, m | 1.00 | 1.00 | 1.00 |
| Gasifier Length, m | 1.175 | 1.742 | 3.000 |
| Carbon Conversion, % | 90.9 | 95.5 | 98.4 |
| Exit Temperature, K | 1766 | 1686 | 1657 |
| Mole Fraction: CO | 0.3863 | 0.3978 | 0.4068 |
| $H_2$ | 0.2413 | 0.2571 | 0.2650 |
| $H_2O$ | 0.2368 | 0.2109 | 0.1980 |
| $CO_2$ | 0.1105 | 0.1063 | 0.1014 |
| $H_2S$ | 0.0005 | 0.0033 | 0.0040 |
| $CH_4$ | 0.005680 | 0.005786 | 0.006057 |
| COS | 0.000321 | 0.000313 | 0.000323 |
| HCl | - | - | - |
| $N_2$ | 0.0178 | 0.0175 | 0.0173 |
| Syngas Flow Rate, kg/s | 54.95 | 55.89 | 56.43 |
| Syngas Density, kg/m$^3$ | - | - | - |
| LHV of Syngas, Btu/lb | 3444.5 | 3683.1 | 3830.5 |
| HHV of Syngas, Btu/lb | 3877.8 | 4117.7 | 4265.7 |
| Cold-Gas Efficiency (HHV), % | 69.4 | 74.9 | 78.4 |
| Net Plant Power, MW | 302 | 325 | 342 |
| Plant Efficiency (HHV), % | 42.3 | 45.5 | 47.9 |

*Summary*

A series of parametric tests have been performed to further benchmark the process model for entrained flow gasifiers that is contained in our framework. As described above, the difference between the gasifier exit temperature and the water-gas shift equilibrium temperature has been found as a function of exit temperature and quench rate. Although the temperature differential can be as high as 250 K at low quench rates (radiant coolers) and high gasifier temperatures (1687 K), the impact on gasifier performance of making this correction is second order. Parametric studies about a baseline condition were carried out to show that heat loss and pressure had little impact on cold gas efficiency but that small variations in slurry concentration and reactor length (impact on carbon conversion) had a major impact. A procedure was proposed for calculating oxygen/fuel, steam/fuel ratio, and reactor length for use in rapid evaluations of gasifier performance or as inputs to CFD calculations to address a number of issues that cannot be addressed by the process model. Comparisons of predicted values from the process model and a CFD model for the gasifier shows good agreement.

# Conclusions

During the last quarter, good progress has been made on the design and development of the virtual engineering based framework.

- The coordinated effort between REI and DOE funded projects at Carnegie Mellon University and the Iowa State University Virtual Reality Applications Center has been very effective. The teams communicate via email and conference calls frequently and have developed positive, productive working relationships.
- Working with our collaborators at CMU and ISU, REI has completed a preliminary detailed software design. The design details the overall structure of the framework, and defines how the REI, CMU and ISU software components interact. As part of the design, we chose open source, platform independent libraries for both the user interface and for the CORBA component architecture being used. The completion of this design represents an important milestone as it defines the development path as we move forward with the program.
- In addition to creating a preliminary software design, significant progress was made on several development tasks, including: completion of a prototype UI, integration of the ISU VR controller with the new UI, decoupling of the CMU core models and the implementation of a prototype CORBA IDL for defining interaction between the various software components. Included in this IDL is a new specification which defines the interface for integrating new models with the framework. This represents completion of an important quarterly MILESTONE for the project.
- To facilitate technology transfer, an updated version of the workbench was provided to the CCSD and NETL. The CCSD has continued to provide valuable feedback on suggested improvements for the workbench and the component models contained within the workbench. The suggested enhancements have been implemented and are contained in the versions of the workbench provided to the NETL and CCSD.
- A detailed description of our research on intrinsic kinetics for coal gasification and development efforts on a pre-processor for computing global rates from the intrinsic kinetics has been completed.
- A benchmarking study for our entrained flow gasifier process model was performed and described. The study indicates good agreement between the process and CFD models that have been developed for entrained flow gasifiers.
- Plans for improvements to our entrained flow gasifier model and for creating a simple model for mercury capture in the gasifier syngas have been outlined.

Plans for the next quarter include:

- Continue development of the detachable, platform independent UI to provide full communication with both the visualization and computational engines
- Enhance the level of virtual engineering functionality available with the framework through tighter coupling with ISU core visualization kernel
- Demonstrate the capabilities of the prototype framework at the ISU VR facilities
- Continue development of the computational engine to enhance scheduling, model integration and data passing capabilities
- Continued development of the entrained flow gasifier model and mercury capture model.

# References

Brown AL, Fletcher TH. Energy Fuels 1998, 12, 745-757.

Fletcher TH, Kerstein AR, Pugmire RJ, Solum MS, Grant DM. Energy Fuels 1992, 6, 414-431.

Ghani, J.K., Steele, R.D., and McDaniel, J.E., "Monitoring and Removal of Mercury in a Texaco IGCC Gasifier System", paper #03-A-91-AWMA, presented at the DOE Mega-symposium, Washington, D.C., May 18-22, 2003.

Holt, N., "Coal Gasification Research, Development and Demonstration – Needs and Opportunities", presented at the Gasification Technologies 2001 Conference, San Francisco, CA, October 8-10, 2001.

Hufen, K., Origin and properties of slag and fly ash obtained in the PRENFLO process. Paper presented at the International Energy Agency expert meeting on the use of coal gasification slag, Arnhem, Netherlands, 10-11 May 1990.

Patterson, J.H., Hurst, H.J., Quintanar, A., Boyd, B.K., and Tran, H., Evaluation of the slag flow characterization of Australian coals in slagging gasifiers. *Research Report 19, Volume 1. Cooperative Research Centre for Black Coal Utilization*, University of Newcastle, Australia, May, 2001.

Shim, H., Sarofim, A., Davis, K., Bockelie, M. "Modeling the Impacts of Soot From Low-NOx Combustion Systems", The 28th International Technical Conference on Coal Utilization & Fuel Systems, Clearwater, FL, March 2003.

Steele, R.D., Ghani, J.K., and McDaniel, J.E., "Monitoring and Removal of Mercury in a Texaco IGCC Gasifier System", presented at the Gasification Technologies Conference, San Francisco, CA, October, 2003.

# Appendix A

## IDL for Virtual Engineering Framework

The following CORBA interface definition language (IDL) code defines the communication and data exchange between the various software components of the virtual engineering framework. The interface "unit" is of particular importance as it defines how computational models are integrated and accessed with the framework.

```
module Types{
  // Array type def

  typedef sequence<long>      ArrayLong;
  typedef sequence<double>    ArrayDouble;
  typedef sequence<string>    ArrayString;
  typedef sequence<boolean>   ArrayBoolean;
  typedef sequence<any>       ArrayAny;

  typedef sequence<ArrayLong>      ArrayLong2D;
  typedef sequence<ArrayDouble>    ArrayDouble2D;
  typedef sequence<ArrayString>    ArrayString2D;
  typedef sequence<ArrayBoolean>   ArrayBoolean2D;
  typedef sequence<ArrayAny>       ArrayAny2D;

  typedef sequence<ArrayLong2D>      ArrayLong3D;
  typedef sequence<ArrayDouble2D>    ArrayDouble3D;
  typedef sequence<ArrayString2D>    ArrayString3D;
  typedef sequence<ArrayBoolean2D>   ArrayBoolean3D;
  typedef sequence<ArrayAny2D>       ArrayAny3D;

  typedef sequence<ArrayDouble3D>    ArrayDouble4D;

  struct Profile {
      ArrayDouble4D RealData3Ds;
      ArrayDouble3D RealData2Ds;
      ArrayDouble2D     RealData1Ds;
    };
};

 module Error{
  exception EUnknown{
    long code;
    string description;
    string interfacename;
    string operatio;
  };
};

module Body{
  interface Unit{ // this is the component model interface

    //This start the calculation
    void StartCalc() raises(Error::EUnknown);

    //This stop the calculation
    void StopCalc() raises(Error::EUnknown);
```

```
    //This is to pause the calculation
    void PauseCalc() raises(Error::EUnknown);

    //This is to Resume the calculation
    void Resume() raises(Error::EUnknown);

    //This is for querying the status of the module
    string GetStatusMessage() raises(Error::EUnknown);

    //This is to get the 3D data
    string GetUserData() raises(Error::EUnknown);

    //This is to Setup the Module
    void SetParams(in string param) raises(Error::EUnknown);

    //This is to Set the ID
    void SetID(in long id) raises(Error::EUnknown);

    //This is to Get the ID
    long GetID() raises(Error::EUnknown);

    //This is to Set the name
    void SetName(in string name) raises(Error::EUnknown);

    //This is to Get the name
    string GetName() raises(Error::EUnknown);
  };

  interface Executive { // This is the execution Engine;

    //Get the Flow-in Data for Module module_id, port port_id, Called by the Unit and/or UI to display the port data
    string GetImportData(in long module_id, in long port_id) raises(Error::EUnknown);

    //This is to Set the Flow-out Data for Module module_id, port port_i, Called by the Unit
    void SetExportData(in long module_id, in long port_id, in string data) raises(Error::EUnknown);

    //This is to Get the Flow out Data for Module module_id, port port_i, Called by the UI to display the port data
    string GetExportData(in long module_id, in long port_id) raises(Error::EUnknown);

    //This is to set the Multi Dimensional Profile Data, call by the upstream Unit Module
    void SetProfileData(in long module_id, in long port_id, in Types::Profile data) raises(Error::EUnknown);

    //This is to get the Multi Dimensional Profile Data, call by the upstream Unit Module, put the result in the out
parameter to save data copying
    void GetProfileData(in long module_id, in long port_id, out Types::Profile data) raises(Error::EUnknown);

    //This is the Set the Module Message, called by Unit
    void SetModuleMessage(in long module_id, in string msg) raises(Error::EUnknown);

    //This is the Set the Module Result, called by Unit
    void SetModuleResult(in long module_id, in string result) raises(Error::EUnknown);

    //This is the set the network, called by the UI
    void SetNetwork(in string network) raises(Error::EUnknown);

    //This is the set the network, called by the current Editing UI
    void SetModuleUI(in long module_id, in string ui) raises(Error::EUnknown);

    //This is to get the network, called by the UI
    string GetNetwork() raises(Error::EUnknown);
```

```
    //This is to set up the executive watch list, Called by the UI (the editable one)
    void SetWatchList(in Types::ArrayLong id) raises(Error::EUnknown);

    //This is to get the watch list, Called by the UI
    Types::ArrayLong GetWatchList() raises(Error::EUnknown);

    //This is to get the status message of Executive, called by the UI
    string GetStatus() raises(Error::EUnknown);

    //This start the network calculation, Called by the UI
    void StartCalc() raises(Error::EUnknown);

    //This stop the network calculation, Called by the UI
    void StopCalc() raises(Error::EUnknown);

    //This is to pause the calculation, Called by the UI
    void PauseCalc() raises(Error::EUnknown);

    //This is to Resume the calculation, Called by the UI
    void Resume() raises(Error::EUnknown);

    //This is to Register a UI to the Executive, make it aware that this UI is connected in
    void RegisterUI(in string UIName) raises(Error::EUnknown);

    //This is to Register a Unit to the Executive
    void RegisterUnit(in string UnitName) raises(Error::EUnknown);
  };

  interface UI { //This is the UI;

    //This is to update the network, called by the Executive
    void UpdateNetwork(in string network) raises(Error::EUnknown);

    //This is to update the module UI, called by the Executive
    void UpdateModuleUI(in long module_id, in string msg) raises(Error::EUnknown);

    //This is to update the Result UI, called by the Executive
    void UpdateModuleResult(in long module_id, in string msg) raises(Error::EUnknown);

    //This is to update the Link content UI, called by the Executive
    void UpdateLinkContent(in long id, in string msg) raises(Error::EUnknown);

    //This is to Raise the Notification or warning or error message
    void Raise(in string notification) raises(Error::EUnknown);
  };
};
```

# Appendix B

# Development of a Kinetics Preprocessor for Modeling Coal Gasification

*Note- All figures, tables, and literature citations, refer to information contained in this appendix.*

# TABLE OF CONTENTS

**Development of a Kinetics Preprocessor ..... 41**

**1 Reaction Mechanism ..... 46**

**2 Literature Survey & Assessment of Kinetics Database ..... 48**

2.1 Devolatilization ..... 48

2.2 Char Morphology ..... 51

2.3 Oxidation and Gasification Rates ..... 53

2.3.1 Rate Expression ..... 53

2.3.2 Effectiveness Factor ..... 55

2.4 Oxidation Rates in Literature ..... 57

2.5 Gasification Rates in Literature ..... 59

2.5.1 Fractional Order Gasification Kinetics ..... 59

2.5.2 Langmuir-Hinshelwood Gasification Kinetics ..... 61

2.5.3 Product Inhibition Effect ..... 63

2.5.4 $CO_2$ Effect ..... 66

2.6 Comparison of $CO_2$ and $H_2O$ Gasification Rates ..... 68

2.7 Catalytic Effect ..... 72

**3 *PREKIN* ..... 73**

3.1 Submodels ..... 75

3.1.1 Devolatilization ..... 75

3.1.2 Single-Film Char Oxidation ..... 75

3.1.3 Pore Structure Model ..... 78

3.1.4 Effectiveness Factor ..... 79

3.1.5 Thermal Annealing ..... 80

3.1.6 The Ash Encapsulation ..... 81

3.1.7 Mass Weighted Rate ..... 83

3.1.8 Gasification Kinetics ..... 83

3.1.8.1 Approach ..... 83

3.1.8.2 Effectiveness factor for Langmuir-Hinshelwood kinetics ..... 84

3.2 Application of PREKIN ..... 87

**4 Concluding Remarks ..... 90**

**5 REFERENCES ..... 92**

# LIST OF FIGURES

Figure 1. Comparison of model prediction of volatile yields. ..... 49

Figure 2. The effect of pressure of gasification gas on the parent order $n_g$ for $CO_2$ and $H_2O$ (Roberts et al., 2001)[25]. Comparison of theoretical values (open triangles) with data (closed triangles) ..... 55

Figure 3. Estimated effectiveness factor using Roberts and Satterfield's formulation.[26] 56

Figure 4. Comparison for a mole fraction of 0.2 oxygen at 18 atmospheres of the apparent kinetic reaction rates from different correlations in the literature along with the mass transfer controlled rate. ..... 58

Figure 5. Comparison of the rates at 18 atmospheres from Lupa et al. and Roberts and Harris for the apparent reaction rates of $O_2$, $CO_2$, and $H_2O$ (each with a mole fraction of 0.2) with the mass transfer controlled rate for oxygen (also with a mole fraction of 0.2) ..... 60

Figure 6. Comparison of the rates at 70 atmospheres from Lupa et al. and Roberts and Harris for the apparent reaction rates of $O_2$, $CO_2$, and $H_2O$ (each with a mole fraction of 0.2) with the mass transfer controlled rate for oxygen (also with a mole fraction of 0.2) ..... 60

Figure 7. Gasification rates normalized by the rates without CO inhibition as a function of $CO/CO_2$ ratio for $CO_2$ gasification at 1300 K / 1 atm and 1300 K / 60 atm. ..... 64

Figure 8. Gasification rates normalized by the rates without CO inhibition as a function of $CO/CO_2$ ratio for $CO_2$ gasification at 1600 K / 1 atm and 1600 K / 60 atm. ..... 65

Figure 9. Effect of $CO_2$ under varying CO and $CO_2$ using the correlation of Mühlen et al.[35] ..... 66

Figure 10. Effect of $CO_2$ under varying CO and $CO_2$ using the correlation of Wu et al.[36] ..... 67

Figure 11. Contribution from various gasifying agents to gasification rate as a function of temperature (K): A) Dry feed and B) Slurry feed ..... 70

Figure 12. Influence of the product gases $H_2$ and CO on the steam and $CO_2$ gasification, respectively, Temperature, 900ºC; pressure, 40 bar.[35] ..... 71

Figure 13. Steady state reaction rates ($r_n$) for $CO_2$ (▲)and $H_2O$ (+) gasification at 1000K (at 25% burn-off) and rox ($H_2O$, CO) (●) at 844K (after partial gasification in $H_2O$ at 1000K to 25% burn-off) as a function of the K/C ratio of the sample. ..... 72

Figure 14. Schematics of *PREKIN* algorithm. ..... 74

Figure 15 Diameters of particle and carbon-rich core region. ..... 81

Figure 16. Sum of CO and $CO_2$ as a funcation of extent of reaction..... 84

Figure 17. *PREKIN* generated kinetic parameters along with EPRI kinetics. [30]..... 88

Figure 18. Comparison of gasification products from Tampa IGCC power plant using EPRI and *PREKIN* kinetics along with the reported composition of cleaned syngas. ..... 89

# 1 Reaction Mechanism

Reaction mechanisms controlling char oxidation/gasification rates consist of three regimes – chemical kinetics, pore diffusion, and external mass transfer controlled-regimes – and their transitional regimes. There is an extensive study on the char reaction under pulverized coal (pc) conditions. The role of heterogeneous chemical kinetics under gasification conditions can be understood using simple scaling laws to extend our knowledge of atmospheric pc systems to higher pressures. The relative importance of chemical kinetics is governed by the dimensionless ratio of the maximum diffusion rate to the reaction rate based on conditions in the bulk fluid: $k_m P_{ox}/kP_{ox}^n$, using global nth order rate expression, where k is a global reaction rate constant and $k_m$ a mass transfer coefficient.

$$k = k_o \cdot \exp\left(-\frac{E}{R \cdot T}\right)$$

$$k_m = \frac{Sh \cdot D}{d_P}$$

where Sh is Sherwood number, D the diffusivity, and $d_p$ the particle diameter. The ratio is a measure of resistances of all internal processes (chemical reaction and pore diffusion). Substituting $ShD/d_p$ for $k_m$ and recognizing that the diffusivity (D) is inversely proportional to pressure, one obtains the following scaling relation:

$$\textit{Extent of chemical kinetic control} \sim \frac{Sh \cdot x_{ox}^{\;1-n}}{d_p \cdot k \cdot P^n}$$

Where P is the total pressure and $x_{ox}$ is the oxygen mole fraction.

This indicates that high total pressure shifts the reaction toward the diffusion-limited regime, but that both enhanced oxygen concentration ($x_{ox}$) and small particle size (both inherent features of high pressure suspension-firing) shift the reaction back toward the kinetically limited regime (for n less than 1). Based on experience with atmospheric systems, it is expected that the oxygen reaction will be governed by the combined effects of boundary layer transport and surface chemical reaction.

Gasification reactions are believed to be strongly influenced by chemical kinetics under IGCC conditions for a variety of reasons. First the $H_2O$ and $CO_2$ reactions are intrinsically much slower than the $O_2$ reaction (much smaller k in the scaling law above), therefore they are much more likely to be chemically limited under identical conditions. Further, volatile matter, leaving the less reactive gasification agents to consume the final char — the slowest stage of the overall gasification process, consumes much of the oxygen. Finally, peak temperatures in oxygen-blown IGCC can be very high, leading to low reactivity chars in the late stages of burning. All of these factors conspire to make intrinsic chemical kinetics of the carbon/$H_2O$ and carbon/$CO_2$ reactions particularly important in gasifiers.

The scaling laws for intra-particle processes clearly show the importance of pore diffusion under some of the reaction conditions of interest (particularly for oxygen and for larger particles). Because of the mixed reaction modes, detailed coupled kinetic and transport models are needed to describe the combustion process in advanced process control systems.

In the following, we present, in order, a literature survey on oxidation/gasification kinetics including devolatilization, relevant features in determining the rates, and a kinetic preprocessor (*PREKIN*) developed during this program.

# 2 Literature Survey & Assessment of Kinetics Database

There is extensive literature on the kinetics of devolatilization and gasification. Much of it is directed at the early moving bed and fluidized bed gasifiers and therefore is not directly relevant to entrained flow gasifiers that involve higher temperatures and shorter residence times than packed and fluidized bed gasifiers. The literature on entrained flow gasification is limited; furthermore, some of the gasification kinetics at high pressures have been carried out on char samples generated at atmospheric pressure or slow heating conditions and that are therefore not representative of chars present in entrained flow gasifiers. In the current work, we built a kinetics database from literature to gain an insight to assist in understanding and modeling devolatilization, oxidation, and gasification behaviors relevant to gasifiers. This includes data from an ongoing effort on gasification kinetics being carried out in Australia under the directions of Dr. David Harris at the CSIRO and Prof. Terry Wall at the University of Newcastle. The Australian data constitute one of the best sources of information.

## *2.1 Devolatilization*

Thermal decomposition kinetics is fast at entrained gasification temperatures and is not a strong function of pressure. Volatile yields are suppressed because volatile transport out of coal particles is inhibited as the pressure is increased. Many models have been developed for devolatilization, which give the rate and volatile yield. Some models provide the capability of predicting the composition of the products, which is also important in devolatilization. The two components of interest are the tar, that is the precursor to soot, and methane. The two-step Kobayashi/Ubayachar correlation[1,2] has been widely used in a devolatilization modeling for a CFD model due to its simplicity, but the two-step model does not provide the composition of the products as well as a pressure dependence. The three most widely used models are the Functional-Group, Depolymerization, Vaporization, Cross-linking (FG-DVC) model developed by Solomon and co-workers [3, 4], FLASHCHAIN by Niksa and Kerstein[5], and the Chemical Percolation Devolatilization (CPD) model by Fletcher and Pugmire[6]. The models yield relatively comparable results. We have chosen the CPD model of Fletcher and Pugmire to provide information of importance to gasification such as tar yields, since it is in the public domain. The model also provides the effect of pressure on volatile yields. The results from the Fletcher and Pugmire model on the effect of pressure on volatile yields are compared in Figure 1 with data and correlations from a number of different investigations.[6 - 15]

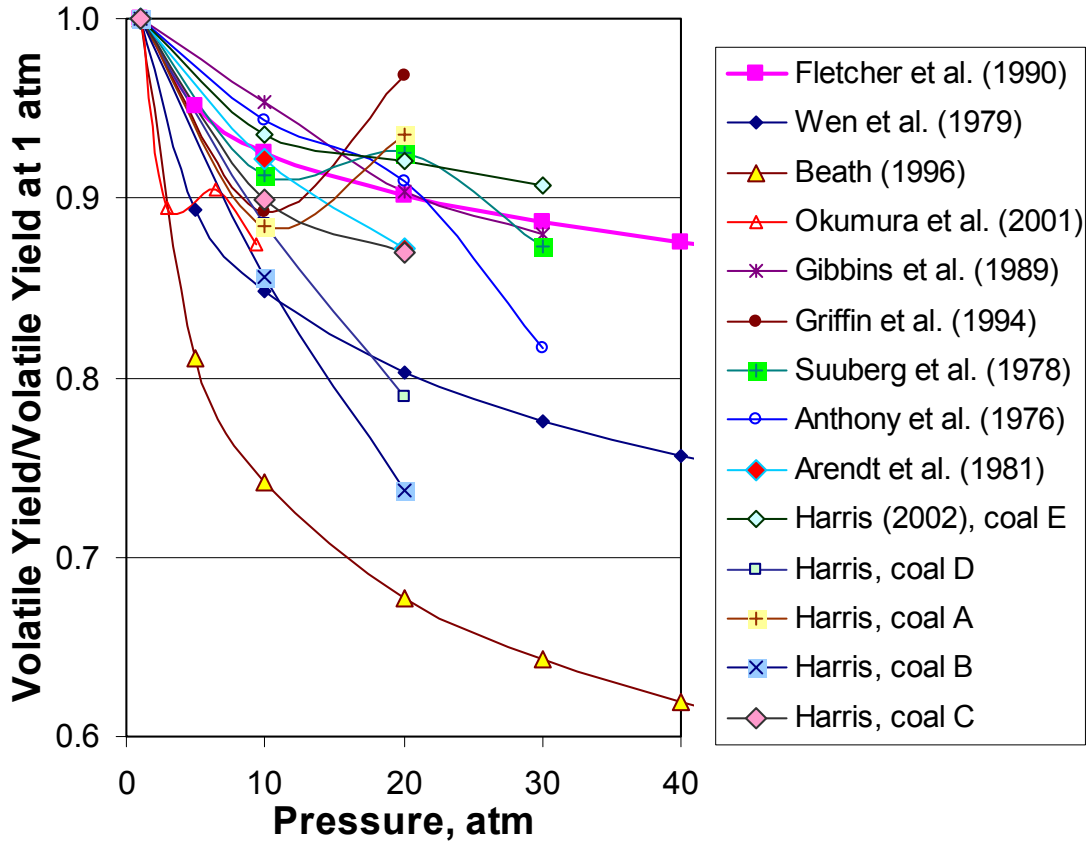


References: Fletcher et al. (1990) [6], Wen et al. (1979)[7], Beath et al. (1996)[8], Okumura et al. (2001)[9], Gibbins et al. (1989)[10], Griffin et al. (1994)[11], Suuberg et al. (1978[12]), Anthony et al. (1976)[13], Arendt et al. (1981)[14], and Harris et al. (2002)[15]

**Figure 1. Comparison of model prediction of volatile yields.**

The effects of pressure show a large variation among the investigators. The CPD model tends to under-predict the decrease in volatile yields with increasing pressure, over a range of pressure from 1 to 30 atm, using a variety of coals. Another correlation, by Beath[8], significantly over-predicts the effect of pressure on volatile yields compared to the other correlations. The volatile yield correlation by Wen et al.[7], based on the data of Anthony et al.[13] over the range of 0.1 to 50 atm has the form:

$$\frac{V_p}{V_{p=1}} = 1 - 0.066 \ln P_t$$

where $P_t$ is the total pressure in atmospheres, $V_p$ the volatile yield at a given pressure, and $V_{p=1}$ the volatile yield at one atmosphere. Our approach is to use the correlation from Wen et al.[7] as a reference value for the pressure dependence of volatile yields, since it passes through the middle of the widely varied correlations among the investigators as

shown in Figure 1. Therefore, re-calculation of the correlation based on CPD results and Wen et al.[7] correlation leads to the following correction form:

$$\frac{V_p}{V_{CPD,p}} = 1 - 0.101082 \cdot \ln P$$

where $V_{CPD,P}$ is the volatile yield calculated by CPD at pressure P.

## 2.2 Char Morphology

The more important effect of total pressure on devolatilization is that on the morphology and reactivity of the product char. Because of the inhibition of volatile transport out of particles during devolatilization, the particles produced at high pressures have a higher percentage of particles with more macropores but with fewer micropores. The chars produced at high pressures contain a high percentage of cenospheric particles, classified as Group I by Wall et al. (2002)[16]. They developed a correlation for the effect of pressure on the fraction of particles forming cenosphere, $f_{ce}$. It is

$$f_{ce} = 0.006P_t + 0.0053vitr + 0.37$$

where $P_t$ is the total pressure in atmospheres and *vitr* is the volume percentage of vitrinite content of coal. Vitrinite concentration in coal can be obtained from readily available Department of Energy Coal Sample (DECS) Bank maintained by Penn State University for a suite of 56 coals[17]. Collection of DECS samples is a continuing effort that begun in 1989. An example DOE Sample data sheet is shown in Table 1. For a gasifier operated at 25 atmospheres with a bituminous coal having 80 percent vitrinite, all of the particles are predicted to be present as cenospheres. For a lower vitrinite content of 50 percent, again at 25 atmospheres, 75 percent of the particles are predicted to be present as cenospheres. The increase in cenosphere content with increasing pressure increases the char fragmentation during gasification with an attendant increase on char reaction rates (Benfell et al., 2000)[22] and a decrease in the particle size of ash produced (Wu et al., 2000).[18]

The microporosity and therefore total surface area of the char is also impacted by the increase in total pressure. These changes in surface area and porosity will also influence the high pressure reactivity of the chars.[22] A further complication on structure is provided by the annealing and deactivation of the carbon structure with increased exposure to high temperatures (Hurt et al., 1998[19]; Seneca et al., 1998[20]). Such deactivation needs to be considered at the longer residence times in the two-stage gasifier and potentially for the char that is recycled.

## Table 1. Example Department of Energy Coal Sample Bank

| Sample | Seam | ASTM Rank | Sample Type | State | County | Year | Ash, dry | S, dry | Btu/lb, dmmf | C, dmmf | H, dmmf | V.M., dmmf | Vit. % | VRo % |
|---|---|---|---|---|---|---|---|---|---|---|---|---|---|---|
| DECS-1 | Bottom | subC | Chan-Seam | TX | Freestone | 1989 | 15.8 | 0.99 | 13239 | 75.9 | 5.8 | 55.5 | 78 | 0.36 |
| DECS-2 | Illinois #6 | hvCb | Chan-Seam | IL | Randolph | 1989 | 16.2 | 4.52 | 14556 | 81.8 | 5.7 | 43.8 | 87 | 0.52 |
| DECS-3 | Coal Basin M | mvb | Chan-Seam | CO | Gunnison | 1990 | 5.4 | 0.65 | 15831 | 88.1 | 5.9 | 28.2 | 94 | 1.28 |
| DECS-4 | Blue | hvCb | Chan-Seam | NM | McKinley | 1990 | 6.2 | 0.46 | 13951 | 78.9 | 5.8 | 48.1 | 88 | 0.51 |
| DECS-5 | Hiawatha | hvCb | Chan-Work | UT | Sevier | 1990 | 8.5 | 0.56 | 14073 | 80.4 | 5.5 | 43.6 | 66 | 0.59 |
| DECS-6 | Blind Canyon | hvAb | Chan-Work | UT | Emery | 1990 | 5.8 | 0.40 | 14874 | 81.9 | 6.3 | 46.9 | 69 | 0.66 |
| DECS-7 | Adaville #1 | hvCb | Chan-Seam | WY | Lincoln | 1990 | 4.2 | 0.98 | 13710 | 77.8 | 5.6 | 47.8 | 95 | 0.45 |
| DECS-8 | Smith-Roland | subC | ROM | WY | Campbell | 1990 | 13.8 | 0.73 | 13148 | 75.8 | 5.3 | 51.8 | 79 | 0.37 |
| DECS-9 | Dietz | subB | Drll-Seam | MT | Bighorn | 1990 | 6.4 | 0.41 | 13251 | 76.1 | 5.2 | 47.1 | 88 | 0.38 |
| DECS-10 | Rosebud | subB | Chan-Work | MT | Rosebud | 1990 | 12.6 | 1.16 | 13378 | 79.7 | 4.3 | 46.9 | 74 | 0.42 |
| DECS-11 | Beulah | ligA | Chan-Seam | ND | Mercer | 1990 | 9.6 | 0.74 | 12350 | 74.1 | 4.5 | 61.6 | 74 | 0.35 |
| DECS-12 | Pittsburgh | hvAb | Chan-Seam | PA | Greene | 1990 | 10.3 | 1.12 | 15259 | 84.7 | 5.8 | 39.4 | 83 | 0.87 |
| DECS-13 | Sewell | mvb | Chan-Seam | WV | Greenbrier | 1990 | 4.2 | 0.62 | 15604 | 88.8 | 5.0 | 25.7 | 77 | 1.35 |
| DECS-14 | Upper Kittanning | hvAb | Chan-Work | WV | Barbour | 1990 | 10.5 | 1.80 | 15503 | 87.0 | 5.6 | 35.4 | 89 | 1.07 |
| DECS-15 | Lower Sunnyside | hvAb | Chan-Seam | UT | Carbon | 1991 | 10.1 | 1.67 | 14967 | 84.3 | 5.7 | 41.3 | 77 | 0.80 |
| DECS-16 | Blind Canyon | hvAb | Chan-Work | UT | Emery | 1991 | 13.9 | 0.47 | 14749 | 82.4 | 6.0 | 47.3 | 77 | 0.64 |
| DECS-17 | Blind Canyon | hvAb | Chan-Sect | UT | Emery | 1991 | 6.6 | 0.44 | 14897 | 82.3 | 6.3 | 49.7 | 80 | 0.59 |
| DECS-18 | Kentucky #9 | hvBb | Chan-Seam | KY | Union | 1991 | 12.3 | 4.21 | 14773 | 82.2 | 6.0 | 45.6 | 86 | 0.56 |
| DECS-19 | Pocahontas #3 | lvb | Chan-Seam | VA | Buchanan | 1991 | 4.6 | 0.74 | 15819 | 90.6 | 4.9 | 18.7 | 89 | 1.71 |
| DECS-20 | Elkhorn #3 | hvAb | Chan-Seam | KY | Floyd | 1991 | 5.5 | 0.97 | 15173 | 85.0 | 5.9 | 39.2 | 78 | 0.87 |
| DECS-21 | Lykens Valley #2 | an | Chan-Seam | PA | Columbia | 1992 | 11.2 | 0.50 | 15122 | 91.5 | 4.1 | 3.9 | 87 | 5.19 |
| DECS-22 | Upper Kittanning | hvAb | Chan-Lith | PA | Armstrong | 1993 | 23.3 | 1.71 | 15827 | 87.8 | 6.1 | 37.8 | 30 | 0.77 |
| DECS-23 | Pittsburgh | hvAb | Chan-Seam | PA | Washington | 1994 | 9.4 | 3.87 | 15307 | 84.6 | 5.8 | 42.3 | 79 | 0.73 |
| DECS-24 | Illinois #6 | hvCb | Chan-Seam | IL | Macoupin | 1994 | 13.4 | 5.53 | 14407 | 80.1 | 5.6 | 45.5 | 90 | 0.49 |
| DECS-25 | Pust | ligA | Chan-Seam | MT | Richland | 1994 | 11.9 | 0.72 | 12569 | 75.8 | 5.3 | 46.9 | 74 | 0.23 |
| DECS-26 | Wyodak | subB | ROM | WY | Campbell | 1994 | 7.6 | 0.43 | 13237 | 76.2 | 6.2 | 48.1 | 86 | 0.29 |
| DECS-27 | Deadman | subA | Drll-Seam | WY | Sweetwater | 1994 | 13.9 | 0.72 | 13757 | 79.2 | 5.4 | 40.6 | 74 | 0.46 |
| DECS-28 | Green | hvCb | Chan-Seam | AZ | Navajo | 1994 | 6.1 | 0.40 | 13648 | 77.8 | 5.5 | 47.9 | 76 | 0.43 |
| DECS-29 | Upper Banner #3 | hvAb | Chan-Seam | VA | Dickenson | 1995 | 6.4 | 0.59 | 15638 | 87.4 | 5.6 | 36.2 | 71 | 1.00 |
| DECS-30 | Splash Dam | mvb | Chan-Seam | VA | Buchanan | 1995 | 3.9 | 0.79 | 15751 | 88.5 | 5.4 | 30.9 | 77 | 1.16 |
| DECS-31 | Pond Creek | hvAb | Chan-Seam | KY | Pike | 1995 | 10.9 | 0.60 | 15538 | 86.8 | 5.5 | 36.6 | 73 | 0.99 |
| DECS-32 | Stockton-Lewiston | hvAb | Chan-Seam | WV | Kanawha | 1995 | 20.3 | 0.73 | 15213 | 85.4 | 5.8 | 38.2 | 68 | 0.90 |
| DECS-33 | Ohio #4A | hvBb | Chan-Seam | OH | Meigs | 1995 | 12.0 | 3.74 | 14630 | 81.8 | 6.0 | 47.8 | 77 | 0.51 |

| Sample | Seam | ASTM Rank | Sample Type | State | County | Year | Ash, dry | S, dry | Btu/lb, dmmf | C, dmmf | H, dmmf | V.M., dmmf | Vit. % | VRo % |
|---|---|---|---|---|---|---|---|---|---|---|---|---|---|---|
| PSOC-1442 | Darco | ligA | Chan-Seam | TX | Harrison | 1985 | 11.3 | 0.78 | 12970 | 74.9 | 4.6 | 75.7 | 83 | 0.47 |
| PSOC-1443 | unnamed | ligA | Chan-Seam | TX | Titus | 1985 | 21.4 | 0.74 | 12878 | 74.4 | 5.4 | 78.2 | 90 | 0.44 |
| PSOC-1446 | New Mexico #8 | hvCb | Chan-Seam | NM | San Juan | 1985 | 20.8 | 0.85 | 14142 | 79.4 | 5.1 | 46.4 | 85 | 0.59 |
| PSOC-1448 | York Canyon | hvAb | Chan-Seam | NM | Colfax | 1985 | 11.4 | 0.46 | 15380 | 85.2 | 6.1 | 40.8 | 85 | 0.71 |
| PSOC-1468 | Buck Mountain | an | ROM | PA | Luzerne | 1985 | 6.8 | 0.49 | 14860 | 96.2 | 1.4 | 3.2 | 86 | 5.45 |
| PSOC-1470 | Pratt | hvBb | Chan-Seam | AL | Walker | 1985 | 20.6 | 2.50 | 15031 | 83.9 | 5.8 | 39.6 | 84 | 0.89 |
| PSOC-1471 | Pee Wee | hvAb | Chan-Seam | TN | Morgan | 1985 | 8.0 | 1.04 | 15046 | 84.0 | 5.6 | 39.4 | 76 | 0.94 |
| PSOC-1482 | Hagel | ligA | Chan-Seam | ND | Oliver | 1985 | 8.5 | 0.72 | 12254 | 72.2 | 4.6 | 46.5 | 88 | 0.39 |
| PSOC-1486 | Big Dirty | subB | Chan-Seam | WA | Lewis | 1985 | 19.4 | 0.94 | 13234 | 75.2 | 6.1 | 52.5 | 90 | 0.38 |
| PSOC-1490 | Brazil Block | hvCb | Chan-Seam | IN | Greene | 1985 | 5.3 | 0.73 | 14830 | 83.4 | 4.5 | 39.8 | 70 | 0.45 |
| PSOC-1491 | Indiana #6 | hvCb | Chan-Seam | IN | Sullivan | 1985 | 15.2 | 2.85 | 14817 | 82.4 | 5.1 | 43.3 | 89 | 0.43 |
| PSOC-1492 | Illinois #5 | hvCb | Chan-Seam | IL | Perry | 1985 | 10.5 | 4.35 | 14490 | 81.4 | 5.4 | 43.6 | 88 | 0.62 |
| PSOC-1498 | Wadge | hvCb | Chan-Seam | CO | Routt | 1985 | 7.1 | 0.52 | 13837 | 78.2 | 5.5 | 44.8 | 89 | 0.60 |
| PSOC-1501 | Juanita C | hvBb | Chan-Work | CO | Gunnison | 1985 | 5.6 | 0.64 | 14465 | 81.2 | 5.3 | 42.7 | 92 | 0.73 |
| PSOC-1515 | Penna. Semian. C | sa | Chan-Seam | PA | Sullivan | 1986 | 29.2 | 0.58 | 15567 | 91.5 | 4.1 | 8.6 | 91 | 2.80 |
| PSOC-1516 | Lower Kittanning | lvb | Chan-Seam | PA | Somerset | 1986 | 10.3 | 1.40 | 15841 | 90.4 | 4.8 | 18.6 | 90 | 1.73 |
| PSOC-1517 | Ohio #5 | hvBb | Chan-Seam | OH | Mahoning | 1986 | 4.8 | 1.92 | 15105 | 84.0 | 5.5 | 39.3 | 87 | 0.86 |
| PSOC-1521 | Lower Hartshorne | lvb | Chan-Seam | AR | Sebastian | 1986 | 11.2 | 0.80 | 15510 | 90.5 | 4.7 | 21.1 | 89 | 1.61 |
| PSOC-1523 | W. Va. #5 Block | hvBb | Chan-Seam | WV | Kanawha | 1986 | 16.1 | 0.71 | 15061 | 85.4 | 5.5 | 37.0 | 62 | 0.92 |
| PSOC-1532 | #4 | subC | Chan-Seam | AK | Koy.-Mid. Y. | 1987 | 9.5 | 0.22 | 12108 | 70.6 | 5.3 | 58.9 | 79 | 0.33 |
| PSOC-1533 | #3 | ligA | Chan-Work | AK | Koy.-Mid. Y. | 1987 | 8.3 | 0.16 | 11665 | 69.6 | 5.0 | 58.4 | 84 | 0.35 |
| PSOC-1534 | Waterfall | subC | Chan-Work | AK | Kenai-Ck. I. | 1987 | 11.1 | 0.15 | 12592 | 71.7 | 5.8 | 49.7 | 87 | 0.28 |
| **PSOC-1535** | **Deadfall Syn. #4** | **subA** | **Chan-Work** | **AK** | **Bar.-Pt. Hp.** | **1987** | **3.3** | **1.46** | **12586** | **75.6** | **4.3** | **37.5** | **86** | **0.73** |

## 2.3 Oxidation and Gasification Rates

### 2.3.1 Rate Expression

Having the correct combustion/gasification kinetics is critical for any gasifier model. Kinetics is needed to size the gasifier/combustor and determine the char combustion efficiency and possible char recycle requirements. The three reactants of importance are $O_2$, $H_2O$, and $CO_2$, with the possible addition of $H_2$ which can contribute to the formation of $CH_4$ at high pressures. The kinetics are determined by three resistances, that of external diffusion of the gas phase reactants to the particle surface and diffusion of the reactants from the surface, diffusion through the porous structure of the char, and reaction at the internal (mostly) and external char surface.

The rate of external diffusion is given by (Smith, 1982)[21],

$$R_D = 0.75 D_i \left(\frac{P_0}{P_t}\right)\left(\frac{T_m}{T_0}\right)^{1.75} \frac{(C_i - C_s)}{d_p}$$

where the diffusion rate, $R_D$ is in kg/m$^2$s, $T_m$ is the average temperature of the boundary layer around the particle, and the subscript 0 denotes the reference conditions. For $P_0$ = 1 bar and $T_0$ = 1500 K, $D_i = 3.1\times10^{-4}$ m$^2$/s for $O_2$. $C_i$, $C_s$, and $d_p$ in the above equation are the reactant concentrations in the gas phase and particle surface and the particle diameter, respectively.

Intrinsic kinetics, a reaction rate based on internal char surface area, is a more fundamental property of the char as it permits the calculation of the effects on the total reaction of changing char structure and surface area.

$$R_{\text{int}} = k_{\text{int}\,o} \cdot \exp\left(-\frac{E_{\text{int}\,o}}{R \cdot T_P}\right) \cdot (P_{si})^{n_{io}}$$

where $R_{int}$ is the intrinsic reactivity, $k_{int\,o}$ the intrinsic reactivity coefficient, $E_{int\,o}$ the true activation energy, $T_p$ particle temperature, $P_{si}$ partial pressure, and $n_{io}$ the true reaction order. Values for the intrinsic rate for a range of pressures is given by the Australian researchers (Benfell et al., 2000[22]; Roberts and Harris, 2000[23]), together with models on how the rates can be converted to the effective surface rate (Liu et al., 2000[24]). One of the advantages of the more fundamental rate expression is that it can permit the determination of the effect of the change in internal pore structure with conversion. Such models have been used to determine the change of reactivity with changing conversion, where there is an initial increase in rate with conversion as the result of the increase in surface area as pores enlarge, followed by a decrease as pores overlap.[24]

The intrinsic kinetics that needs to be used in gasification rate expression is complicated by the adsorption/desorption kinetics at sites with a range of activities. The Langmuir-Hinshelwood model is found to provide a simple representation of the competition of

different reactants as well as products with the surface. For the $CO_2$-char reaction, for example, it provides the following relationship for the reaction rate

$$R_c = \frac{k_1 p_{CO_2}}{1 + k_2 p_{CO} + k_3 p_{CO_2}}$$

The denominator represents the inhibition of the reaction as a result of adsorption on reactive surface sites by reactants and products. The fractional order rate law (or n-th order power law), which is often used in representing the reaction rate, includes reactant inhibition but does not include product inhibition. Therefore, the Langmuir-Hinshelwood type kinetics may be suitable for describing gasification behavior including the inhibition effect. The importance of the inhibition effect is further described in section 2.5. The number of terms in the denominator of the Langmuir-Hinshelwood model will increase in a product mixture containing other species that can be adsorbed on surface sites, such as $H_2O$. As a consequence of the inhibiting factor of adsorbed species, the order of the reaction between $CO_2$ and carbon decreases with increasing pressure (Roberts et al, 2001[25]). This is a reason, additional to the changes in char morphology with pressure, that it is difficult to extrapolate kinetics from atmospheric to higher pressures.

The intrinsic kinetics can be combined with pore diffusion models to obtain the reaction of a particle or to derive reactivity per unit external surface area of a particle, the so-called apparent reactivity. Data obtained on particles are often correlated in terms of the apparent reactivity. A commonly used correlation used for chemical kinetics is the fractional order kinetics (or n-th order power law kinetics) as shown in the following:

$$R_s = k_g P_{si}^{n_g} e^{-E_g / RT}$$

where the rate constant '$k_g$', the activation energy '$E_g$', and the reaction order '$n_g$' includes the complexity of the internal diffusion and therefore may vary with extent of reaction, and the exponent '$n_g$' includes the effects of partial pressures $P_{si}$ of other species at the particle surface and therefore also applies only over a limited range of pressures and gas concentrations. Examples of the dependence of the reaction order on pressure are given for the case of the $H_2O$/carbon and $CO_2$/carbon reactions in Figure 2. The reaction orders are seen to decrease from around 0.7 at one atmosphere to less than 0.2 at 30 atmospheres. The open symbols represent predictions of $n_g$ for $CO_2$ and $H_2O$ based on a model of the saturation of surface sites.[25]

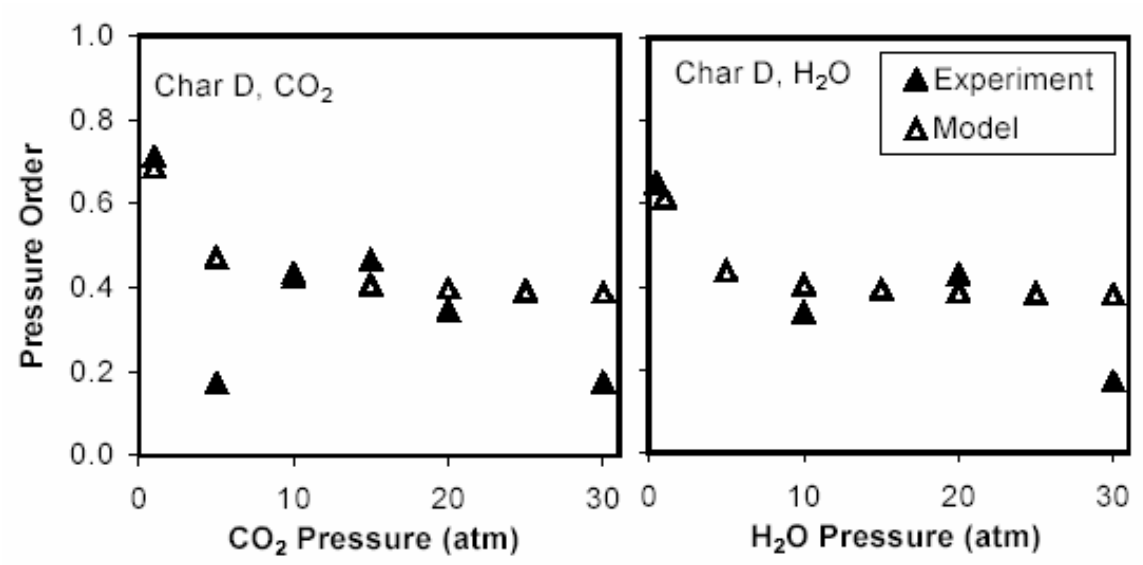


**Figure 2. The effect of pressure of gasification gas on the parent order $n_g$ for $CO_2$ and $H_2O$ (Roberts et al., 2001)[25]. Comparison of theoretical values (open triangles) with data (closed triangles)**

### 2.3.2 Effectiveness Factor

The effectiveness factor is defined as the ratio of the actual reaction rate to that which would occur if all of the surface throughout the inside of the particle were exposed to reactant of the same concentration and temperature as that existing at the outside surface of the particle. The factor is a measure of the effects of mass transfer within a porous structure on observed reaction characteristics[26] and is used to describe global reaction rate in conjunction with intrinsic kinetics. The effectiveness factor can be estimated for Langmuir-Hinshelwood type kinetics as described in Roberts and Satterfield (1965)[26]. Figure 3 shows the estimated effectiveness factor for a particle of 100 μm in diameter at pressures of 1 and 30 atm. The initial $CO_2$ mole fraction was fixed to 0.09. Calculation was performed under two $CO/CO_2$ ratios, 0.1 and 10, respectively. Mühlen et al. [35]'s kinetics was used in the calculation. It is estimated that chemical kinetics controls a reaction at 1500K or lower temperatures. At temperatures higher than 1500K, pore diffusion starts to play a role in determining the rate. At higher pressures, $CO/CO_2$ ratio also affects the effectiveness factor. High $CO/CO_2$ ratio shifts the point where pore diffusion starts to control to a higher temperature. Typical gasifier temperatures can be from 1200K to 1900K and the pressure can reach up to 80 atm. Under these widely varied conditions, Figure 3 implies that pore diffusion or external mass diffusion in addition to intrinsic chemical kinetics should be well addressed in determining the rates in a modeling.

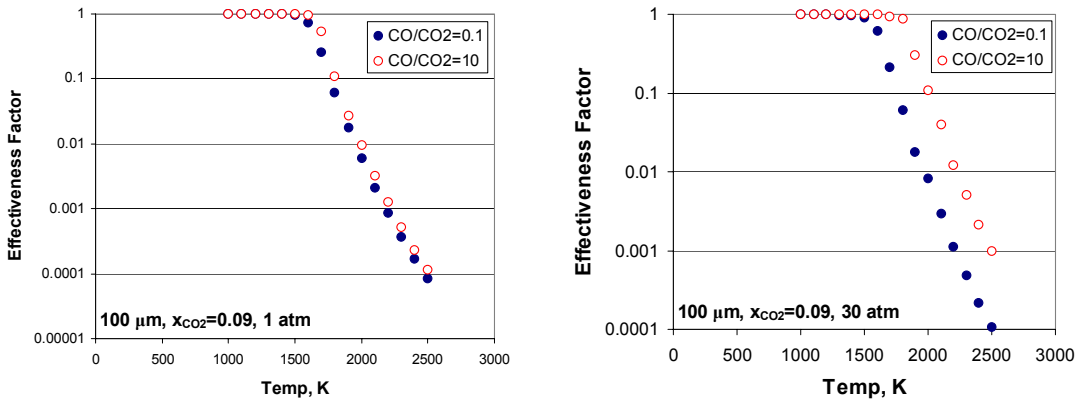


**Figure 3. Estimated effectiveness factor using Roberts and Satterfield's formulation.[26]**

## 2.4 Oxidation Rates in Literature

The literature on char oxidation is enormous and the references in Table 2, were selected because the authors had applied the correlations in the modeling of gasifiers.

**Table 2. Selected Kinetics for Char Oxidation with $O_2$**

| Authors | E, J/mol | k | n |
|---|---|---|---|
| Banin et al. (1997)[27] | 51048 | 40 $kg/m^2 \cdot s$ | - |
| Joutsenoja et al. (1999)[28] | 82368 | 1903 m/s | 1 |
| Monson et al. (1995)[29] | $f(P_t)$ | $F(P_t)$ | 0.5 |
| Lupa and Kliesch (1979)[30] | 100483 | 1404 $kg/m^2 \cdot s \cdot atm$ | 1 |
| Otaka et al. (2001)[31] | 105000* | 95000 $1/atm^n$ | 0.75 |
| Benyon (2002)[32] | 223000 | $5.81\times10^{10}$- $1.02\times10^{11}$ $kg/m^2 \cdot s \cdot atm^n$ | 0.83 |
| Roberts and Harris (2000)[34] | | | |

* E in Otaka et al.'s paper is given as 105,000 J/kmol but this gives too small a temperature dependence. The value was interpreted as being J/mol to bring it into line with the other measurements.

The intrinsic reaction rates of oxygen with carbon can be factors $10^3$ to $10^5$ higher than those of $H_2O$ and $CO_2$ (Harris and Smith, 1990[33]; Roberts and Harris, 2000[34]), but these differences decrease to factors less than ten at the higher temperatures in oxygen-blown gasifiers since the activation energies for $CO_2$ and $H_2O$ are higher (i.e. higher temperature dependence) than those of $O_2$ (see Figure 5 and Figure 6). When allowance is made for diffusion within pores and in the particle boundary layer, the differences between the rates of the exothermic $O_2$/C reaction and the endothermic $CO_2$/C and $H_2O$/C become much smaller. But it is usually the case that the reaction of oxygen with carbon precedes those of $CO_2$ and $H_2O$.

The importance of a chemical kinetics, $R_s$ with the surface concentration $P_{si}$ equated to the bulk concentration, is compared in Figure 4 with a mass-transfer controlled rate, $R_D$ with $C_{si}$ for the case of reactions at 18 atmospheres with oxygen having a mole fraction of 0.2. There is wide difference in the rates among the different investigators at low temperatures but the data spread is much smaller at the higher temperatures. Most of the correlations show the higher reaction rates, at the temperatures of interest for oxidation in either a single-stage or the first stage of a two-stage gasifier ($\geq$ 2000K), that equal or exceed the mass transfer resistance (with the exception of the results of Monson et al.[29]) indicating that the reaction occurs under mass diffusion controlled regime. As the temperature drops, however, the chemical kinetic rate becomes controlling, underlying the importance of finding good kinetic data on char oxidation.

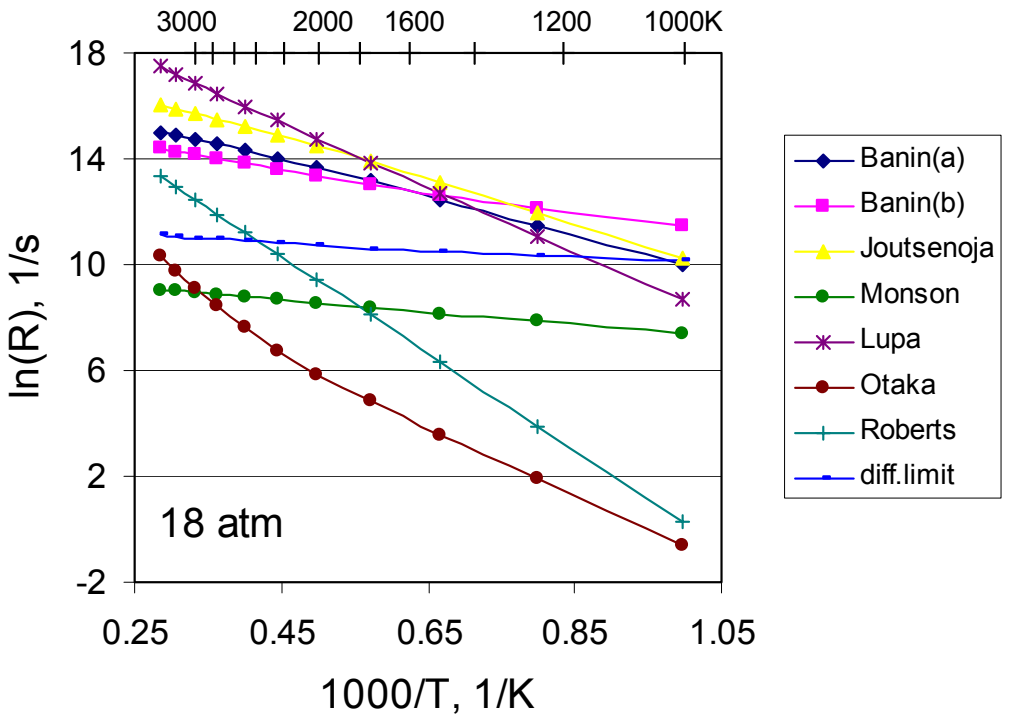


**Figure 4. Comparison for a mole fraction of 0.2 oxygen at 18 atmospheres of the apparent kinetic reaction rates from different correlations in the literature along with the mass transfer controlled rate.**

## *2.5 Gasification Rates in Literature*

### 2.5.1 Fractional Order Gasification Kinetics

The $CO_2$ and $H_2O$ gasification rates are compared in Figure 5 and Figure 6 along with $O_2$ oxidation rates for the kinetics correlations of Lupa and Kliesch (1979)[30] and Roberts and Harris (2000)[34], at total pressures of 18 and 70 atmospheres. The mole fractions of each oxidation or gasification agent were set to 0.2. Both correlations show that the oxidation rates are greater than $CO_2$ and $H_2O$ gasification rates by two to ten orders of magnitude over the temperature range of 1000 to 3000K with the large differences being at the lower temperatures. Lupa et al.'s kinetics shows that, at the high temperature end of the gasifier (over 2500K), the $CO_2$ and $H_2O$ gasification rates are approaching that of $O_2$ and can exceed the mass transfer limit implying that the gasification occurs under mass diffusion controlled regime. The oxidation rate is limited by external mass diffusion over 1150K. At the low temperatures of the second stage of a two-stage gasifier (1200 – 2000K), the rates of the reactions of gasification with $CO_2$ and $H_2O$ are much slower than that of $O_2$. On the other hand, Roberts et al.'s kinetics show that both oxidation and gasification occurs under chemical kinetics controlled regime where the temperature is lower than 2200K. Over 2200K, the gasifications still occur under chemical kinetics controlled regime, while oxidation is limited by mass diffusion. Similar trends are found at high pressure (see Figure 6).

Typical temperature range in a gasifier can vary from 1200 to 3000K at which reaction rate can be controlled by either one of the chemical kinetics and the external mass diffusion or both. This illustrates that the kinetics model to describe oxidation/gasification in a gasifier should allow for a smooth transition from these two ends of reaction regimes including pore diffusion controlled regime in between.

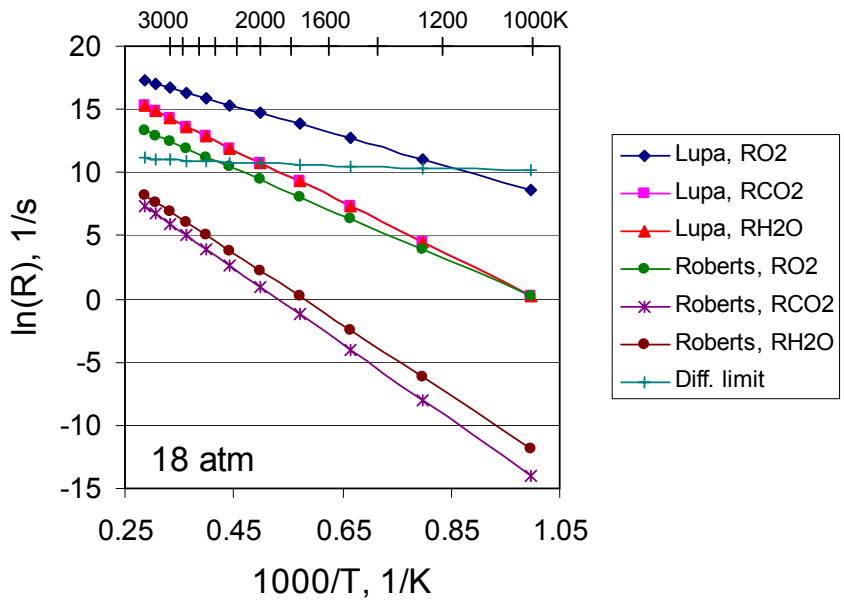


**Figure 5. Comparison of the rates at 18 atmospheres from Lupa et al. and Roberts and Harris for the apparent reaction rates of $O_2$, $CO_2$, and $H_2O$ (each with a mole fraction of 0.2) with the mass transfer controlled rate for oxygen (also with a mole fraction of 0.2)**

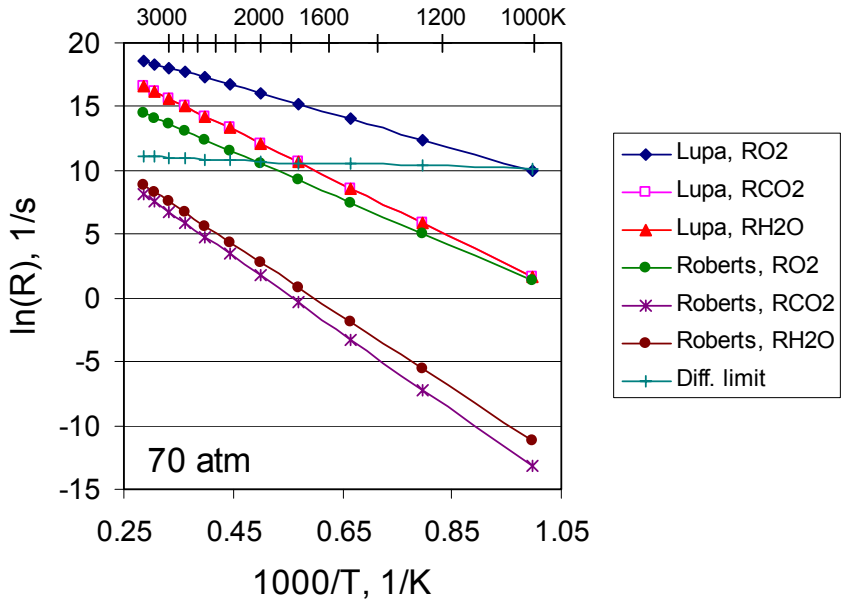


**Figure 6. Comparison of the rates at 70 atmospheres from Lupa et al. and Roberts and Harris for the apparent reaction rates of $O_2$, $CO_2$, and $H_2O$ (each with a mole fraction of 0.2) with the mass transfer controlled rate for oxygen (also with a mole fraction of 0.2)**

### 2.5.2 Langmuir-Hinshelwood Gasification Kinetics

Reactant and product inhibition effects can be significant in determining gasification rates. For example, the fractional order kinetics for $CO_2$ takes care of the $CO_2$ inhibition but not the CO inhibition. Therefore, a Langmuir-Hinshelwood formulation is best suitable as it explicitly places the product inhibition effect in the denominator as shown in the following equation for $CO_2$ gasification:

$$r_s\left(\frac{g}{g\,\min}\right)=\frac{k_1P_{CO_2}}{1+k_2P_{CO}+k_3P_{CO_2}}$$

where

$$k_1=k_{10}\cdot\exp\left(-\frac{E_1}{RT}\right)$$

$$k_2=k_{20}\cdot\exp\left(-\frac{E_2}{RT}\right)$$

$$k_3=k_{30}\cdot\exp\left(-\frac{E_3}{RT}\right)$$

Selected Langmuit-Hinshelwood $CO_2$ gasification rates used in this study are shown in Table 3.

Mühlen et al.[35] used more complicated formulation for gasifications including the effects of conversion as in the following equation:

$$r_s\left(\min^{-1}\right)=\exp\left(-\frac{bX^2}{RT}\right)\frac{r_1P_{CO_2}+r_8P_{CO_2}{}^2+r_9P_{H_2O}+r_{11}P_{H_2O}{}^2+r_{12}P_{H_2O}P_{H_2}+r_4P_{H_2}{}^2}{1+r_2P_{CO_2}+r_3P_{CO}+r_{10}P_{H_2O}+r_5P_{H_2}}$$

$$b(kJ/mol)=\frac{1245-T}{1.56}$$

$$r_i=k_{io}\cdot\exp\left(-\frac{Ei}{RT}\right)$$

where X is a conversion level. Rate constants, $r_i$ are shown in Table 4.

**Table 3. Selected $CO_2$ gasification rates using Langmuir-Hinshelwood formulation**

| Investigators | Sample | $k_{10}$, bar-1min-1 | $k_{20}$, bar-1 | $k_{30}$, bar-1 | E1, kJ/mol | E2, kJ/mol | E3, kJ/mol | Temp., °C | Pres.,atm |
|---|---|---|---|---|---|---|---|---|---|
| Wu et al. [1988][36] | Electrode Carbon | 8.428E+06 | 2.166E-09 | 1.569E-01 | 205.2 | -257.2 | -30.1 | 871-1038 | 1.026 |
| Gadsby et al. [1948][37] | Coconut shell cahrcoal | 8.049E+09 | 1.276E-08 | 3.204E+06 | 246.2 | -190.5 | 126.0 | 734-829 | 0.013-1.0 |
| Wu [1949][38] | Coke | 5.078E+08 | 4.034E-06 | 3.060E-02 | 258.3 | -168.7 | -25.5 | 816-1038 | 1.026 |
| McBride [1947][39] | Coke | 8.049E+05 | 1.276E-02 | 2.545E-01 | 200.5 | -64.5 | -26.8 | 802-1093 | 1 |
| Strange et al. [1976][40] | SP-1 graphite | NA | NA | NA | 414.5 | -54.4 | 50.2 | 900-1007 | 0.013-0.197 |
| Mentser et al. [1973][41] | Spheron 6 | NA | NA | NA | 221.9 | -92.1 | -20.9 | 900-1200 | 1 |
| Biederman [1965][42] | SP-1 graphite | NA | NA | NA | 433.3 | 29.3 | 129.8 | 960-1120 | 0.14 |
| Ergun [1956][43] | Graphite and activated carbons | | | | | | | 700-1400 | 1 |
| von Fredersdorff et al. [1957][44] | Pitch Coke | 8.866E+05 | 1.689E-10 | 0.000E+00 | 167.9 | -230.7 | 0.0 | 800-1090 | |
| Lewis et al. [1949][45] | Anthracite | 1.858E+02 | 3.884E-04 | 1.520E-04 | 136.1 | -70.8 | -69.5 | 926-1150 | |
| Harris et al. [2002][23] | Port Kembla-3 | 7.539E+17 | 1.814E+04 | 1.530E+18 | 510.0 | 89.0 | 461.0 | | |
| | Port Kembla-4 | 3.303E+07 | 1.925E-09 | 6.140E+21 | 250.0 | -247.0 | 544.0 | | |
| | Port Kembla-5 | 4.884E+06 | 1.135E-05 | 6.485E+17 | 222.0 | -155.0 | 452.0 | | |
| | Queensland B Coke-1 | 2.320E+18 | 1.753E+17 | 2.310E-23 | 495.0 | 368.0 | -526.0 | | |
| | Queensland C Coke-1 | 3.030E+16 | 4.731E+01 | 4.256E+08 | 469.0 | 31.0 | 209.0 | | |
| | Queensland C Coke-3 | 3.253E+13 | 4.256E-01 | 1.135E+10 | 381.0 | -45.0 | 238.0 | | |

**Table 4. Rate constants for Mühlen et al.[35]'s kinetics**

| | $k_{io}$ | $k_{io}$ Unit | $E_i$, kJ/mol |
|---|---|---|---|
| $r_1$ | 2.710E+04 | $bar^{-1}min^{-1}$ | 153.1 |
| $r_2$ | 2.060E-02 | $bar^{-1}$ | -23.0 |
| $r_3$ | 3.820E-02 | $bar^{-1}$ | -48.1 |
| $r_4$ | 3.180E+07 | $bar^{-2}min^{-1}$ | 237.4 |
| $r_5$ | 1.530E-09 | $bar^{-1}$ | -209.2 |
| $r_8$ | 1.220E-02 | $bar^{-2}min^{-1}$ | 68.5 |
| $r_9$ | 2.960E+05 | $bar^{-1}min^{-1}$ | 154.0 |
| $r_{10}$ | 1.110E+01 | $bar^{-1}$ | 29.5 |
| $r_{11}$ | 4.400E-03 | $bar^{-2}min^{-1}$ | 80.3 |
| $r_{12}$ | 6.140E-03 | $bar^{-2}min^{-1}$ | 8.5 |
| Temp., °C | 800-950 | | |
| Pres.,atm | 39.48 | | |

### 2.5.3 Product Inhibition Effect

Figure 7 shows the CO inhibition effects by plotting the normalized $CO_2$ gasification rate from various literatures as a function of $PCO/PCO_2$ for two conditions: 1300K/1atm and 1300K/60atm. Calculations were performed under varying $CO/CO_2$ keeping the sum of CO and $CO_2$ constant arbitrarily set to the total pressure. As in the figure, the inhibition effect can be quite significant and this effect should be well addressed in any gasification rate formulation. Under typical operating conditions in various units as specified in the figure, the inhibition effects can cause a maximum of 4 orders of magnitude in the rate depending on which correlation is used. At the higher pressure (60 atm) and at the same temperature, a degree of rate reduction is even higher. At 1600K, the variations in the rate reduction become small compared to those at 1300K as shown in Figure 8, however, increased pressure makes the inhibiting effect larger.

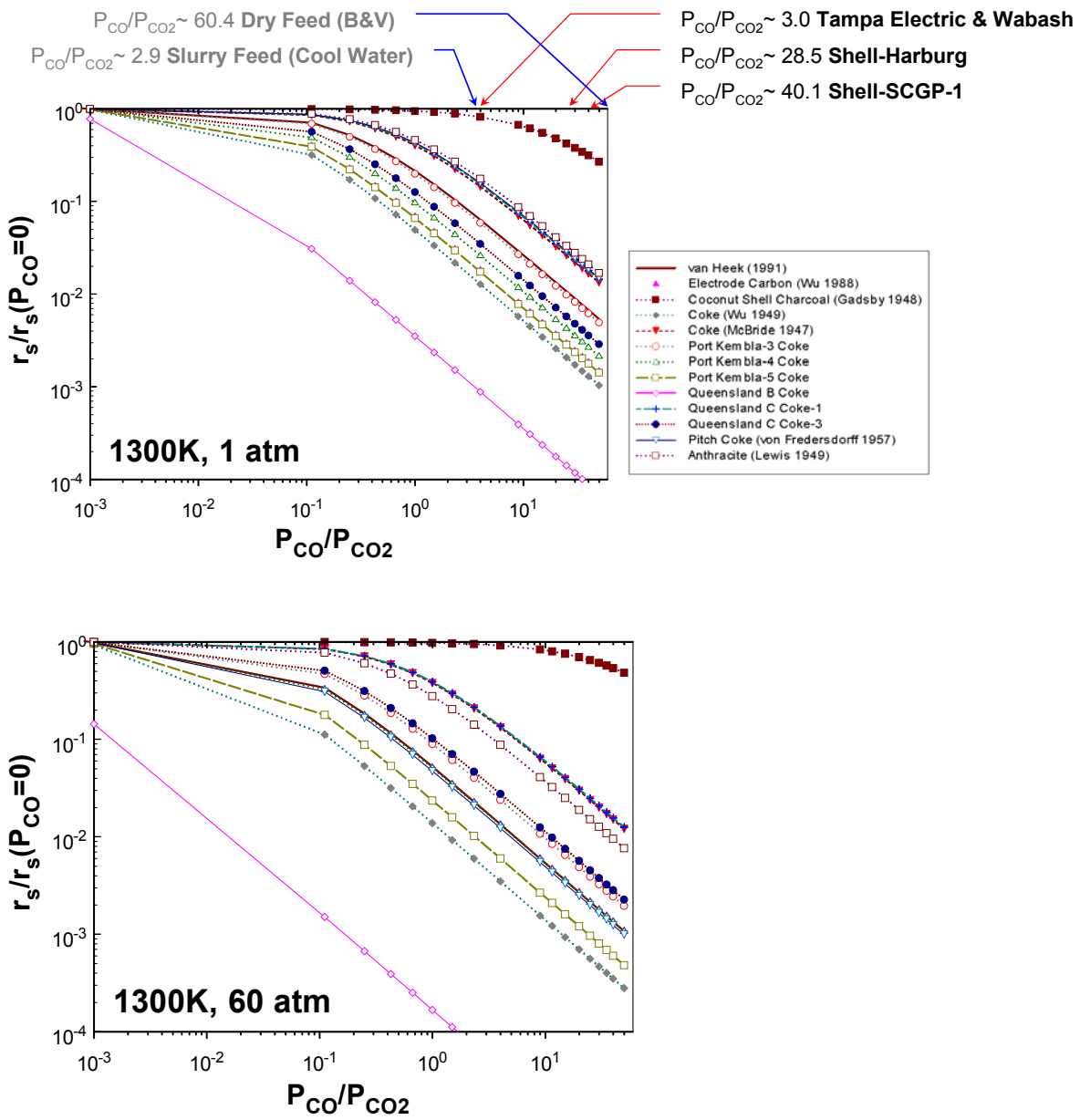


**Figure 7. Gasification rates normalized by the rates without CO inhibition as a function of $CO/CO_2$ ratio for $CO_2$ gasification at 1300 K / 1 atm and 1300 K / 60 atm.**

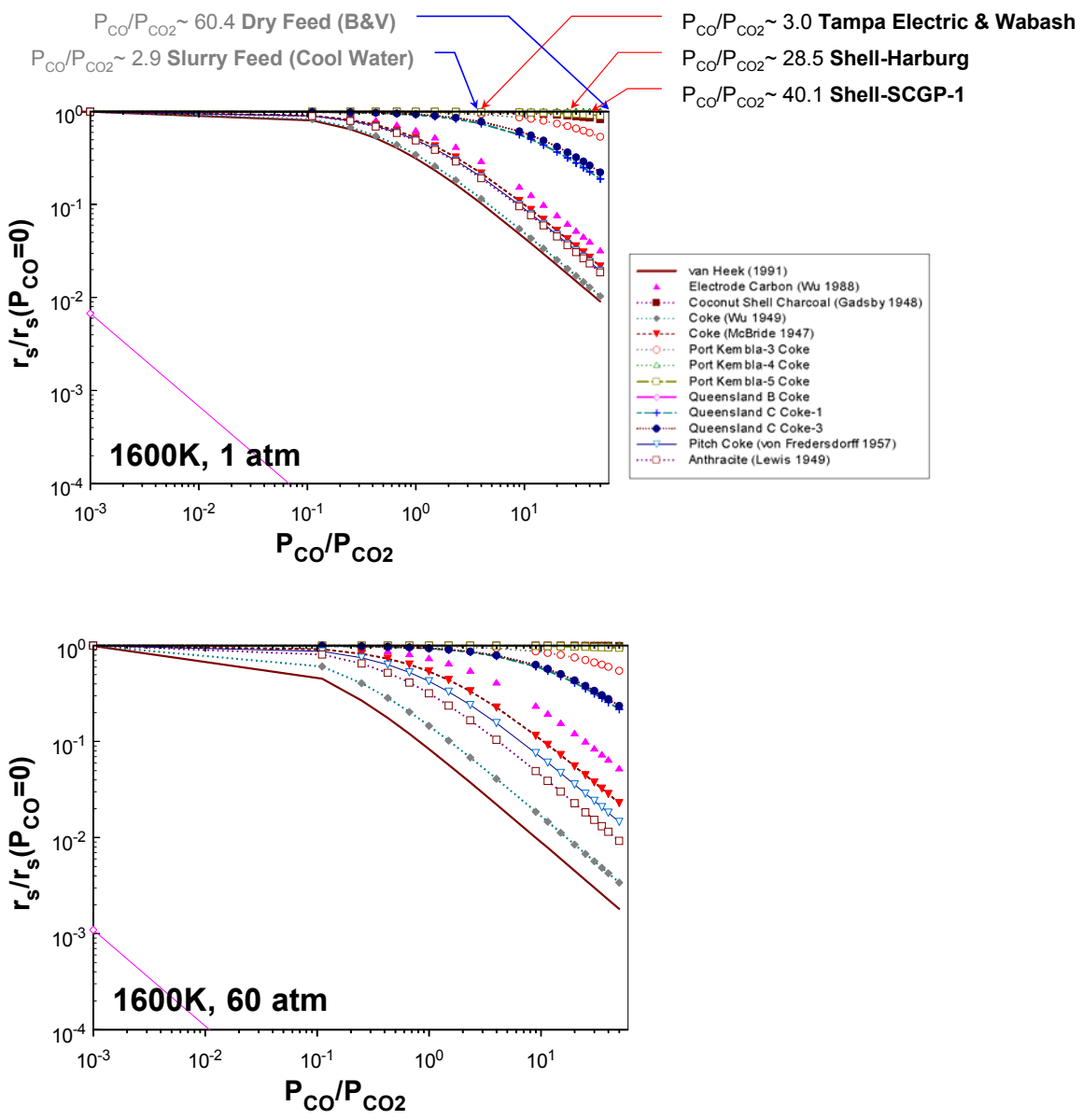


**Figure 8. Gasification rates normalized by the rates without CO inhibition as a function of $CO/CO_2$ ratio for $CO_2$ gasification at 1600 K / 1 atm and 1600 K / 60 atm.**

### 2.5.4 $CO_2$ Effect

Using the correlations of Mühlen et al. [35] and Wu et al.[36], $CO_2$ effect is studied in Figure 9 and Figure 10. Calculations were performed under a given $CO_2$ and varying CO. As $CO_2$ partial pressure increases, the CO inhibition effect also increases. In addition, with decreasing temperature and increasing pressure, the degree of CO inhibition increases. These results indicate that both reactant and product can be involved in the rate reduction.

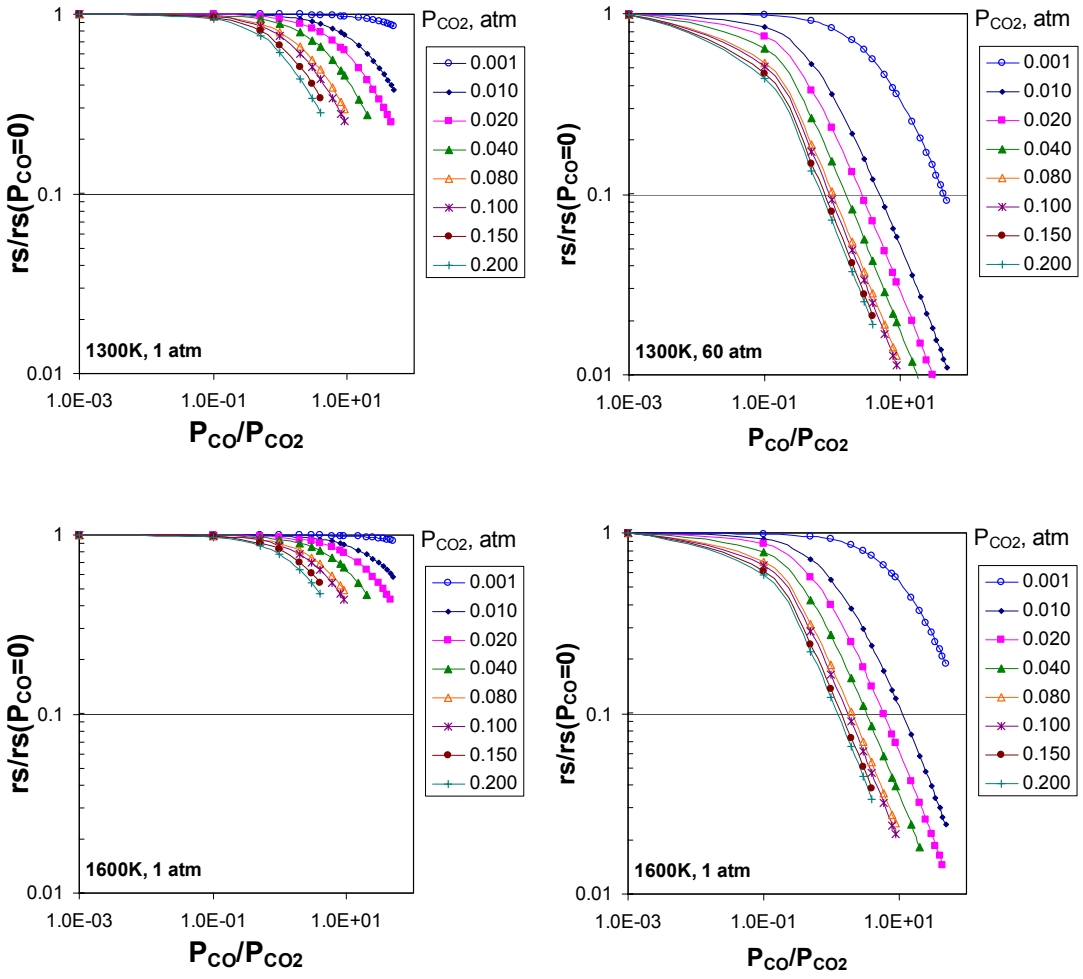


**Figure 9. Effect of $CO_2$ under varying CO and $CO_2$ using the correlation of Mühlen et al. [35]**

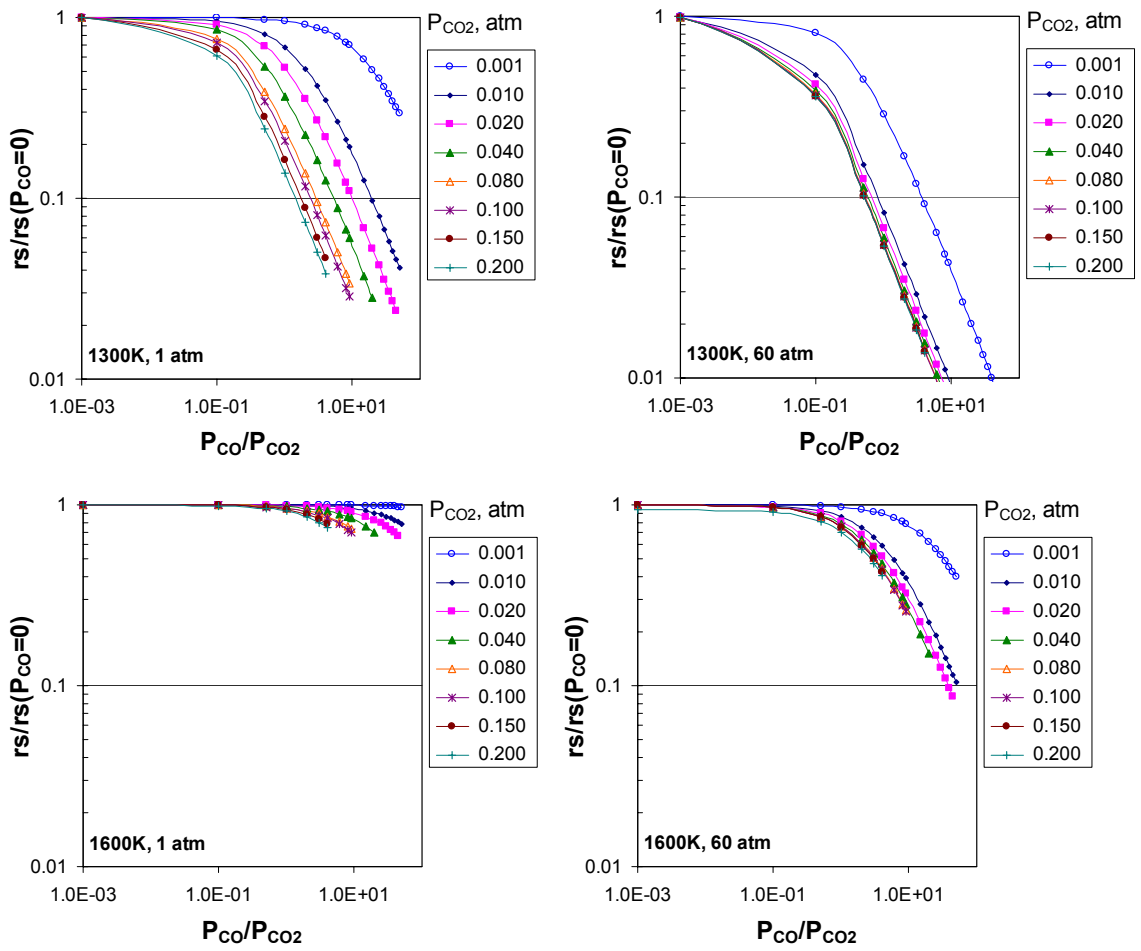


**Figure 10. Effect of $CO_2$ under varying CO and $CO_2$ using the correlation of Wu et al.[36]**

## 2.6 Comparison of $CO_2$ and $H_2O$ Gasification Rates

For a typical gas composition in a gasifier, the importance of gasification is estimated using the correlation from Mühlen et al.[35]

Mühlen et al. reported the rate equation for complex gasifying agents:

$$r_s\left(\min^{-1}\right) = \exp\left(-\frac{bX^2}{RT}\right)\frac{r_1 P_{CO_2} + r_8 P_{CO_2}{}^2 + r_9 P_{H_2O} + r_{11} P_{H_2O}{}^2 + r_{12} P_{H_2O} P_{H_2} + r_4 P_{H_2}{}^2}{1 + r_2 P_{CO_2} + r_3 P_{CO} + r_{10} P_{H_2O} + r_5 P_{H_2}}$$

$$b(kJ/mol) = \frac{1245 - T}{1.56}$$

where X is a conversion level. Rate constants ($R_i$'s) are shown in Table 4.

Typical gas composition in a gasifier is shown in Table 5 for dry and slurry feeds.

**Table 5. Typical gas composition in a gasifier for dry and slurry feeds**

| Mole Fraction | Dry Feed | Slurry Feed |
|---|---|---|
| CO | 0.415 | 0.380 |
| CO2 | 0.086 | 0.117 |
| H2 | 0.290 | 0.269 |
| H2O | 0.158 | 0.163 |
| H2S | 0.008 | 0.008 |
| CH4 | 0.032 | 0.052 |
| COS | 0.000 | 0.000 |
| AR | 0.011 | 0.011 |

The rate equation can be re-arranged as in the following to understand contributions to the overall rate from each composition:

$$r_s\left(\min^{-1}\right) = \exp\left(-\frac{bX^2}{RT}\right)\frac{[C-CO2] + [C-H2O] + [C-(H2O, H2)] + [C-H2]}{1 + r_2 P_{CO_2} + r_3 P_{CO} + r_{10} P_{H_2O} + r_5 P_{H_2}}$$

where

$$[C-CO2] = r_1 P_{CO_2} + r_8 P_{CO_2}{}^2$$

$$[C-H2O] = r_9 P_{H_2O} + r_{11} P_{H_2O}{}^2$$

$$[C-(H2O,H2)] = r_{12} P_{H_2O} P_{H_2}$$

$$[C-H2] = r_4 P_{H_2}{}^2$$

Mass-diffusion limited gasification rates are also calculated for comparison. The diffusion coefficient for a mixture is calculated by the following equations based on the Chapman-Enskog kinetic theory[46]:

$$D_{ik} = 0.0018583 \cdot T^{2/3} \cdot \frac{\left[\frac{1}{M_k} + \frac{1}{M_i}\right]^{1/2}}{P \cdot \sigma_{ik}{}^2 \cdot \Omega_d}$$

where $D_{ik}$ is a species diffusivity for i and k, $\Omega_d$ a dimensionless function of the temperature and of the intermolecular potential field for one molecule of i and one of k, and $\sigma_{ik}$ the Lennard-Jones parameters of species i and k.

Mixture diffusivity can be estimated by:

$$D_{im} = \frac{(1-X_i)}{\sum_{k \neq i} \left(\frac{X_k}{D_{ik}}\right)}$$

where $D_{im}$ is the diffusivity for the $i^{th}$ specie and $X_{i \text{ or } k}$ the mole fraction of species i and k.

Figure 11 shows a degree of contribution from each of the gasification reactions. Contributions from $H_2O$ and $H_2$ gasifying agents to overall rate are much higher than that of $CO_2$. With increasing temperature, the contributions from $H_2O$ and $H_2$ gasifying agents even further increases. In addition, total gasification rate becomes similar to mass transfer limited rate with increasing temperature implying that the external mass transfer controls a reaction at high temperature.

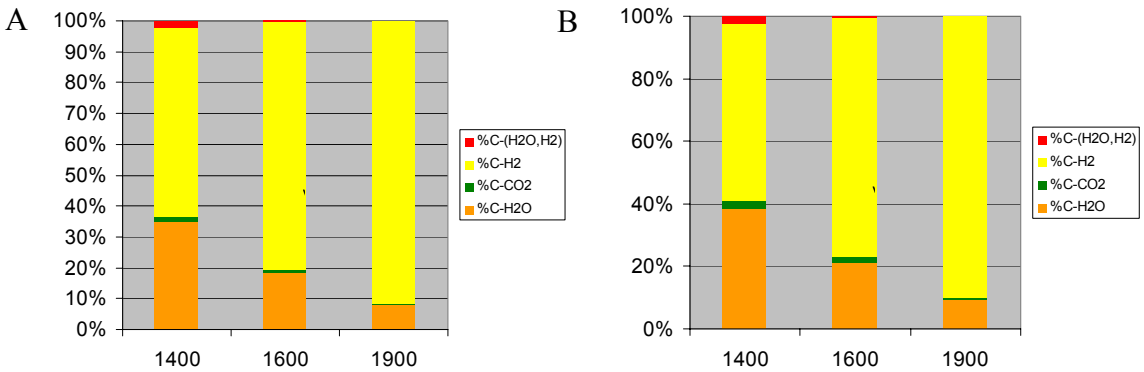


| Gas Comp. | T, K | Total Gas Rate | %C-H2O | %C-CO2 | %C-H2 | %C-(H2O,H2) | ML, CO2+H2O | ML,CO2+H2O+H2 |
|---|---|---|---|---|---|---|---|---|
| Dry Feed | 1400 | 1.716E+00 | 34.7% | 1.9% | 61.2% | 2.2% | 5.124E+04 | 2.654E+05 |
| | 1600 | 2.082E+02 | 18.6% | 1.0% | 80.2% | 0.3% | 5.619E+04 | 2.904E+05 |
| | 1900 | 4.182E+04 | 7.9% | 0.4% | 91.7% | 0.0% | 7.222E+04 | 3.344E+05 |
| Slurry Feed | 1400 | 1.708E+00 | 38.4% | 2.7% | 56.6% | 2.3% | 5.729E+04 | 2.685E+05 |
| | 1600 | 1.968E+02 | 21.3% | 1.5% | 76.9% | 0.3% | 6.285E+04 | 2.938E+05 |
| | 1900 | 3.769E+04 | 9.3% | 0.6% | 90.1% | 0.0% | 7.066E+04 | 3.296E+05 |

Mass diffusion limited (ML) rates were calculated assuming Sherwood number is 2, particle diameter 150 μm, and specific surface area 200 $m^2/g$

**Figure 11. Contribution from various gasifying agents to gasification rate as a function of temperature (K): A) Dry feed and B) Slurry feed**

Figure 12 shows experimental results showing inhibition effects from $H_2O$ and $CO_2$ gasifications.[35] The inhibition effect of $H_2$ in $H_2O$ gasification is higher than that of CO in $CO_2$ gasification. For example, when P($H_2$ or CO)/P is equal to 0.2, $CO_2$ gasification has about 35% reduction and $H_2O$ gasification about 82% reduction in the rates. In addition, it shows that the $H_2O$ rates are faster than $CO_2$ gasification rates. This is consistent with the estimation performed in Figure 11.

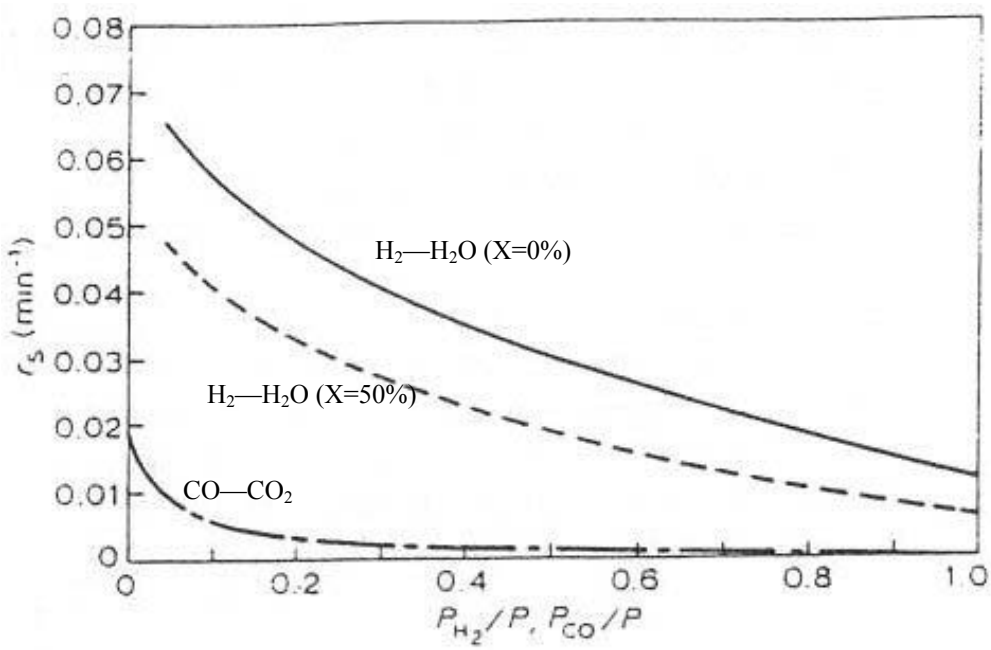


**Figure 12. Influence of the product gases $H_2$ and CO on the steam and $CO_2$ gasification, respectively, Temperature, 900ºC; pressure, 40 bar.** [35]

## 2.7 Catalytic Effect

Biomass is an attractive option to use in gasification for energy production. One of the important characteristics of biomass is highly dispersed inorganic matter resulting in high combustion rate. As an example, Figure 13 shows gasification rates as a function of potassium loading (K/C).[47] With increasing K/C, the rate increased from negligible rate at K/C=0. K/C values can vary depending on fuel, however the importance of catalytic effect is clear as shown in the figure. Therefore, the effect of catalyst (e.g. alkali metal) on gasification rate should be well addressed in a model.

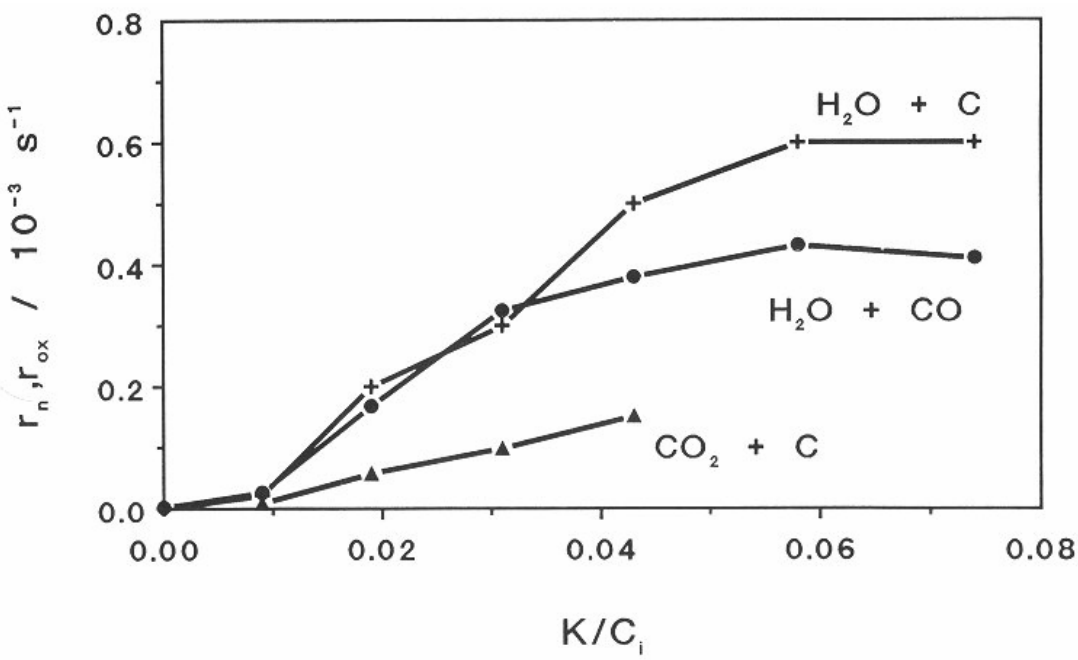


**Figure 13. Steady state reaction rates ($r_n$) for $CO_2$ (▲)and $H_2O$ (+) gasification at 1000K (at 25% burn-off) and rox ($H_2O$, CO) (●) at 844K (after partial gasification in $H_2O$ at 1000K to 25% burn-off) as a function of the K/C ratio of the sample[47].**

# 3 PREKIN

To account for all of the aforementioned solid fuel combustion/gasification behaviors, a model is required. The current heterogeneous reaction model in CFD uses global (or apparent) kinetics due to its simplicity. However, to estimate/study the effects of operational change such as varying total pressure in a system, a more mechanistically based model is required. Our strategy is to use a separate sub-model to address the effects of operational change on kinetics and provide a global kinetics parameters based on the results from the sub-model. This was accomplished by developing a kinetic pre-processor (*PREKIN*) that includes fundamental description of combustion/gasification processes including devolatilization, intrinsic rate, and pore/mass diffusion. Several models are available for each process in order for the user to choose a specific model to obtain kinetics for combustion/gasification. Figure 14 illustrates how global kinetics parameters are obtained in *PREKIN*. Briefly, *PREKIN* calculates reaction rates based on inputs specified by the user and optimizes the global rate expression to fit the calculated rates by varying three parameters: $A_G$, $E_G$, and m. In the following subsections, various models implemented in *PREKIN* are described. Then, preliminary results are presented and compared with EPRI kinetics.[30]

**INPUT**

- Fuel properties: C, H, O, Ash, and Volatile matter
- Particle size distribution
- Intrinsic rate parameters in:
  - Power law kinetics
  - Langmuir-Hinshelwood kinetics
- Reaction Conditions: temperature, partial pressure

**PREKIN**

**Kinetic pre-processor**

- Generate gasification rate based on input temperature and pressure
- Combination of various sub-models: devolatilization, porosity development, thermal annealing, ash inhibition, diffusion, $CO/CO_2$, and gasification rate
- Fitting and Optimizing the results with the equation

$$q_{rxn} = A_G \cdot \exp\left(-\frac{E_G}{R \cdot T_P}\right) \cdot (P_s)^n \qquad \text{(A)}$$

**OUTPUT**

$A_G$ , $E_G$ , & n

For given range of reaction conditions

**Figure 14. Schematics of *PREKIN* algorithm.**

## 3.1 Submodels

### 3.1.1 Devolatilization

The user can choose from two devolatilization models: the Two-step mechanism[1] and the Chemical Percolation Devolatilization (CPD) model[48]. The user needs to input kinetic parameters to use the two-step mechanism. The CPD model needs coal structure parameters from 13 C NMR measurements. The structure parameters can manually be typed in or *PREKIN* can generate the parameters based on the fuel compositions[48]. When the CPD model is selected and the total pressure is higher than 1 atm, the following correlation is used:

$$\frac{V_p}{V_{CPD,p}} = 1 - 0.101082 \cdot \ln P_t$$

where $V_{CPD,P}$ is the volatile yield calculated by CPD at pressure, P.

### 3.1.2 Single-Film Char Oxidation

The single-film char oxidation model sets a foundation for the *PREKIN* model and consists of four aspects:

1) intrinsic n-th (fractional) order kinetics or semi-global kinetics[49]
2) film diffusion in the particle boundary layer;
3) heat generation and transfer;
4) mode of burning expressions.

The model assumes that the particle is isothermal and oxygen is assumed to be the sole oxidizer; the intrinsic n-th order rate equation is used to represent char oxidation rates:

$$q_{rxn} = \eta \cdot k_o \cdot \exp\left(-\frac{E}{R \cdot T_P}\right) \cdot \left(\frac{P_s}{R \cdot T_P}\right)^n \cdot s \cdot \sigma_A \cdot \gamma$$

where $q_{rxn}$ (gC/cm$^2$-s) is the rate of reaction (expressed per unit external area of solid), $\gamma$ (cm) the characteristic dimension of the particle (d/6 for sphere and thickness/2 for flat plate), $\eta$ the effectiveness factor, s (cm$^2$/gC) the specific surface area, $\sigma_A$ (gC/cm$^3$) the carbon density in the particle, $k_o$ (gC/s-cm$^2$-(mol/cm$^3$)$^n$) the intrinsic reactivity coefficient (or the pre-exponential factor in the Arrhenius form), and n the true reaction order.

In the semi-global kinetics[49], the following mechanism was used for steady-state combustion:

1. $C + O_2 \rightarrow 2C(O)$

2. $C(O) + O_2 \rightarrow CO_2 + C(O)$

3. $C(O) \rightarrow CO$

Then, intrinsic rate is expressed as:

$$q_{rxn,\text{int}} = \frac{k_1 k_2 P_{O2} + k_1 k_3 P_{O2}}{k_1 P_{O2} + k_3 / 2}$$

where $k_1$, $k_2$, and $k_3$ are reaction rate constants (dimensionless or $bar^{-1}$).

This report will describe the oxidation submodel based on intrinsic n-th order kinetics. Semi-global kinetics can be similarly derived.

Both CO and $CO_2$ are considered as primary products of the heterogeneous char oxidation reactions. The $CO/CO_2$ product ratio (MR) [52] is assumed to depend on particle temperature and is expressed as:

$$MR = \frac{CO}{CO_2} = A_C \cdot \exp\left(-\frac{E_C}{RT_P}\right)$$

The fraction of the carbon content of the particle converted to $CO_2$ is denoted as $\psi$ and determined from the $CO/CO_2$ product ratio (MR):

$$\psi = \frac{1}{1 + MR}$$

The mass diffusion outside the particle is[50]:

$$q_{diff} = \frac{k_D P}{\gamma} \ln\left(\frac{1 - \gamma P_s / P}{1 - \gamma P_g / P}\right) \text{ where } \gamma \neq 0$$

$$q_{diff} = k_D \left(P_{og} - P_{os}\right) \text{ where } \gamma = 0$$

where the mass transfer coefficient is given by:

$$k_D = \frac{M_C D_{ox} Sh}{d_p R' T_m \nu_o}$$

where $M_c$ is molecular weight of carbon (gC/mol), $D_{ox}$ oxygen diffusion coefficient ($cm^2/s$), R' gas constant, and $\nu_o$ and $\gamma$ are given by:

$$\nu_o = \frac{1 + \psi}{2}$$

$$\gamma = \frac{\psi - 1}{\psi + 1}$$

Then, the quasi-steady state assumption leads to

$$q_{diff} = q_{rxn}$$

If the particle temperature is known, the above equations can be used to determine the value of $P_s$ (partial pressure at the char surface). Numerically, a value is guessed for $P_s$, the difference between $q_{rxn}$ and $q_{diff}$ is driven to zero by changing the value of $P_s$ using the Newton-Raphson method.

A set of equations was derived to describe the evolution of particle size and density during combustion. The char particle is assumed to consist of two components: a combustible component whose density changes with burnoff and a non-combustible inorganic component whose density is constant. The particle (or apparent) density is defined as:

$$\rho_P = \frac{\text{total weight of particle}}{\text{volume of particle}} = \frac{w_c + w_a}{V_p}$$

where the particle volume, $V_p$, is the volume occupied by a sphere having a diameter of $d_p$. Rewriting this equation in terms of the apparent densities of the combustible material and the ash and the volumes they occupy yields:

$$\rho_P = \frac{w_C}{V_p} + \frac{w_a}{V_P} = \frac{v_c}{V_P} \cdot \frac{w_c}{v_c} + \frac{v_a}{V_P} \cdot \frac{w_a}{v_a} = \frac{v_c}{v_c + v_a} \cdot \rho_c + \frac{v_a}{v_c + v_a} \cdot \rho_a$$

The weights of combustible material and ash in the particle can be expressed as:

$$w_a = x_a \cdot V_P \cdot \rho_P = v_a \cdot \rho_a$$

and

$$w_C = (1 - x_a) \cdot V_P \cdot \rho_P = v_C \cdot \rho_C$$

then,

$$v_a = \frac{x_a \cdot V_P \cdot \rho_P}{\rho_a} \quad \text{and} \quad v_C = \frac{(1 - x_a) \cdot V_P \cdot \rho_P}{\rho_C}$$

Finally, total volume is defined as:

$$V_P = v_a + v_C = \frac{x_a \cdot V_P \cdot \rho_P}{\rho_a} + \frac{(1 - x_a) \cdot V_P \cdot \rho_P}{\rho_C}$$

Utilizing the above equations to eliminate $v_a$ and $v_C$ yields the following relation for the apparent density of the coal char particle:

$$\rho_P = \frac{1}{\frac{x_a}{\rho_a} + \frac{(1 - x_a)}{\rho_C}}$$

The change of parent carbon density is related to burnout by:

$$\frac{\rho_c}{\rho_{c,o}} = \left( \frac{m_c}{m_{c,o}} \right)^{\alpha}$$

where $\alpha$ is the empirical mode of burning parameter[51,52]. The values of $\alpha$ were calculated from high temperature char oxidation data [52] for ten US coals and were found to vary only modestly from char to char, and a mean value of 0.2 can be taken as an estimate for an unknown char. After calculating a new $\rho_c$, the equation above can be used to convert the $\rho_c$ value into a $\rho$ value, after which geometric considerations yield:

$$\frac{d_p}{d_{p,o}} = \left[ \left( \frac{m}{m_o} \right) \left( \frac{\rho_o}{\rho} \right) \right]^{1/3}$$

### 3.1.3 Pore Structure Model

The molecular diffusivity, $D_M$ is estimated by the correlation developed for $O_2$ diffusion into $N_2$ [53]:

$$D_M = 1.523 \cdot 10^{-5} \cdot \frac{T_m^{1.67}}{P}$$

where $T_m$ is $(T_g+T_p)/2$ and P pressure.

A pore structure model is required to convert molecular diffusivity to effective diffusivity. Two pore models were implemented into *PREKIN*: the parallel pore model and the random pore model. The parallel model[54] uses the porosity and tortuosity to obtain effective diffusivity as in the following equation:

$$D_{effC} = \frac{D_M \cdot \theta_{CORE} \cdot f}{\tau}$$

where $\theta_{CORE}$ is core porosity, f the fraction of the total porosity in feeder pores, and $\tau$ the tortuosity. In *PREKIN*, the intraparticle transport parameter ($\tau$/f) is treated as a single empirical parameter (default value is 6). In the random pore model[55], the effective diffusivity can be expressed as:

$$D_{effC} = \theta_{Macro}{}^{2} D_{Macro} + \frac{(\theta - \theta_{Macro})^2 (1 + 3\theta_{Macro})}{1 - \theta_{Macro}} D_{micro}$$

where

$$D_{Macro} = \frac{1}{\frac{1}{D_M} + \frac{1}{D_{Macro}}}$$

$$D_{micro} = \frac{1}{\frac{1}{D_M} + \frac{1}{D_{K,micro}}}$$

$$D_{K,Macro} = 9.7 \times 10^3 r_{p,Macro} \left( \frac{T}{Mw_g} \right)^{0.5}$$

$$D_{K,micro} = 9.7 \times 10^3 r_{p,micro} \left( \frac{T}{Mw_g} \right)^{0.5}$$

where $r_{p,Macro}$ and $r_{p,micro}$ are the average macro- and micro-pore radii, respectively, $\theta$ porosity, $\theta_{Macro}$ macro porosity, and $Mw_g$ molecular weight of reactant (32 for $O_2$).

### 3.1.4 Effectiveness Factor

An $\eta$ is estimated by calculating Thiele modulus ($M_T$):

$$M_T = \gamma \cdot \sqrt{\frac{n+1}{2 \cdot D_{effC}} \cdot \left( \frac{P_S}{R \cdot T_P} \right)^{n-1} \cdot k_o s \cdot \exp\left( -\frac{E}{RT_P} \right) \cdot C_{incore} \cdot d_C}$$

where $C_{incore}$ is the core carbon mass per unit volume ($gC/cm^3$) and is calculated by:

$$C_{incore} = \rho_{CORE} \cdot (1 - x_{ao})$$

The effective diffusivity for transport to the particle interior is estimated as described in Sec. 3.1.3. For example, by utilizing the parallel pore model, the effective diffusivity is:

$$D_{effC} = \frac{D_M \cdot \theta_{CORE} \cdot f}{\tau}$$

where $\theta_{CORE}$ is core porosity, f the fraction of the total porosity in feeder pores, and $\tau$ the tortuosity. Porosity in core region ($\theta_{CORE}$) is calculated by the following equations:

$$\theta_{CORE} = 1 - x_{ao} \cdot \left( \frac{\rho_{CORE}}{\rho_{at}} \right) - \frac{1}{2} \cdot \rho_{CORE} \cdot (1 - x_{ao})$$

where $x_{ao}$ is initial ash fraction, $\rho_{at}$ true ash density, and $\rho_{core}$ core density is calculated from particle diameters, $d_P$ and $d_C$:

$$\rho_{CORE} = \rho_P \cdot \left( \frac{d_P}{d_C} \right)^3 \cdot (1 - x_a \cdot (1 - AshinCore))$$

where AshinCore is ash fraction in carbon-rich core region.

Then, η is calculated based on $M_T$ value assuming a sphere:

$M_T > 4$ $\qquad \eta = \frac{1}{M_T}$

$M_T < 0.4$ $\qquad \eta = 1$

$0.4 < M_T < 4$ $\qquad \eta = \frac{1}{3M_T} \cdot \left( \coth(3M_T) - \frac{1}{3M_T} \right)$

Finally, the burning rate ($q_{rxn}$, gC/cm$^2$-s) is calculated by the following equation:

$$q_{rxn} = \gamma \cdot \eta \cdot k_o s \cdot \left( \frac{P_s}{R \cdot T_P} \right)^n \cdot \exp\left( -\frac{E}{R \cdot T_P} \right) \cdot C_{incore}$$

### 3.1.5 Thermal Annealing

The thermal annealing submodel is a variation of the distributed activation energy formulation proposed by Suuberg[56] and based on Hurt's Carbon Burnout Kinetics code.[19] The thermal annealing model assumes that the intrinsic reactivity is proportional to the total number of active sites. The active sites are assumed to have identical oxidation kinetics, but to anneal at different rates. The number of active sites for a given type is assumed to be annealed by a first order thermal process:

$$\frac{d(N_E / N_o)}{dt} = -\left( \frac{N_E}{N_o} \right) A_d \exp\left( -\frac{E_d}{RT_p} \right)$$

Where $N_E$ is the number of active sites that share a common annealing activation energy $E_d$, $N_o$ is the total number of active sites, and $A_d$ and $E_d$ are the empirical kinetic parameters. All active sites are assumed to share a common pre-exponential factor for annealing, $A_d$, but to be distributed with respect to $E_d$:

$$d(N_E/N_o) = f_E(t, E_d)dE_d$$

$$\frac{N(t)}{N_o} = \int_0^\infty f_E(t, E_d)dE_d$$

At time zero the function $f_E$ is assumed to be a normalized log-normal distribution in $E_d$ and integration yields a value of unity. In Zone I,

$$\frac{A(t)}{A_o} = \frac{N(t)}{N_o} = \int_0^\infty f_E(t, E_d)dE_d$$

In Zone II, classical Thiele theory leads to[51]:

$$\frac{A(t)}{A_o} = \left[\frac{N(t)}{N_o}\right]^{1/2} = \left[\int_0^\infty f_E(t, E_d)dE_d\right]^{1/2}$$

### 3.1.6 The Ash Encapsulation

Mineral matter inhibits combustion in the late stages by one of several physical mechanisms. First, an ash film can pose an additional resistance to oxygen transport to the reacting surface; second, the existence of the inert ash layer outside the particle increases the diameter of the particle, reducing the global rate expressed on an external area basis.

The ash encapsulation submodel assumes the presence of a porous ash film surrounding a carbon-rich core as shown in Figure 15. The core region is assumed to have a constant local mass fraction of mineral matter equal to the overall mineral mass fraction in the unreacted char.

The following figure illustrates the particle and carbon-rich core diameters during burnoff.

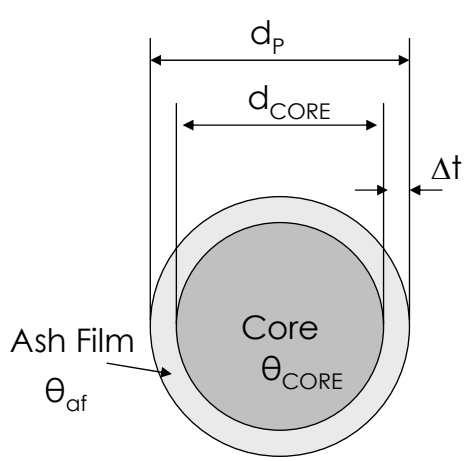


**Figure 15 Diameters of particle and carbon-rich core region.**

The core region has a constant local mass fraction of mineral matter equivalent to the overall mineral mass fraction in the unreacted char, (Ma/Vp)o. A mass balance on the inorganic fraction yields:

$$M_a = \frac{\pi}{6} dc^3 \left( \frac{M_a}{V_P} \right)_o + \frac{\pi}{6} \left( d_P{}^3 - dc^3 \right) \rho_{af}$$

where the first term accounts for ash in the carbon–rich core, and the second term accounts for ash in the outer film. Note that this expression neglects the effects of vaporization and inorganic reactions involving mass changes

(Ma/Vp)o can be expressed as:

$$\left( \frac{M_a}{V_P} \right)_o = \frac{M_a}{\left( \frac{M_{t,o}}{\rho_o} \right)} = X_{a,o} \rho_o$$

where the ash mass is:

$$M_a = X_a M_P = X_a \rho \left( \frac{\pi}{6} \right) d_P{}^3$$

and the subscript "o" denotes properties of the unreacted char. The ash density can be expressed as:

$$\rho_{af} = \rho_{a,n} \left( 1 - \theta_{af} \right)$$

where $\Theta_{af}$ is the porosity of the ash film, and $\rho_{a,n}$ is the density of nonporous ash.

The ash film thus has a volume determined by its mass, the nonporous ash density, $\rho_{a,n}$, and the porosity of the ash film, $\Theta_{af}$. Using the above equations:

$$d_c = d_P \left[ \frac{\left( X_a \rho - \rho_{a,n} \left( 1 - \theta_{af} \right) \right)}{\left( X_{ao} \rho_o - \rho_{a,n} \left( 1 - \theta_{af} \right) \right)} \right]^{1/3}$$

This result allows the calculation of the core diameter, $d_c$, knowing the constants $\rho_{a,n,}$, $\Theta_{af}$, $X_{a,o}$, $\rho_o$, the instantaneous overall particle diameter, dp, and density, $\rho$. The latter two parameters can be calculated from the mode of burning equations.

The effective diffusivity through the ash film ($D_{effa}$) is estimated by the empirical correlation[57]:

$$D_{effa} = D_M \cdot \theta_{af}{}^{2.5}$$

where $D_M$ is the molecular diffusivity and $\theta_{af}$ the porosity of the ash film.

The overall mass diffusion coefficient representing the combined diffusional coefficient in the boundary layer and ash film can be expressed by:

$$k_{diff} = \frac{Sh \cdot D_M \cdot D_{effa} \cdot d_p}{R \cdot T_m \cdot \upsilon \cdot \left(Sh \cdot \Delta t \cdot D_M \cdot d_C + D_{effa} \cdot d_C{}^2\right)}$$

where Sh is a Sherwood number (default is 2.0), $\Delta t$ ash film thickness, and $\upsilon$ stoichiometric coefficient ($molO_2/gC$).

$$\upsilon = \frac{(1+\psi)}{2}\frac{1}{M_c}$$

### 3.1.7 Mass Weighted Rate

A mass weighted rate for multiple particle sizes is calculated as in the following equation:

$$\overline{q}_{rxn} = \frac{\sum\left(q_{rxn,i} \cdot pmf_i\right)}{\sum pmf_i}$$

where $q_{rxn,i}$ is an oxidation/gasification rate for particle size, i, and $pmf_i$ is the mass fraction of the particle size, i.

### 3.1.8 Gasification Kinetics

#### 3.1.8.1 Approach

Two models are available in *PREKIN*; power-law (or fractional order rate law) and Langmuir-Hinshelwood kinetics. Power-law kinetics is similar to the one previously described for oxidation. Therefore, only Langmuir-Hinshelwood kinetics is described here.

For a given gasifier operation, rate is a function of $P_{CO}$ and $P_{CO2}$ (or $P_{H2}$ and $P_{H2O}$). Both the products of gasification (CO or $H_2$) and the ratio of the product (CO or $H_2$) to the reactant ($CO_2$ or $H_2O$) are a function of conversion (extent of reaction) as shown in Figure 16. Then $CO/CO_2$ can be expressed as a function of $CO_2$. Similarly, $H_2/H_2O$ can be expressed as a function of $H_2O$.

$$CO/CO_2 = f(CO_2)$$

$$H_2/H_2O = f(H_2O)$$

Then, the calculated reaction rate can be fitted with the n-th order global power law expression with embedded inhibition effect of a product (including reactant) in gasification.

<u>*Rate from Langmuir-Hinshelwood Kinetics*</u> =

$$A_G \exp\left(-\frac{E_G}{RT}\right) P_{CO2}{}^{n} \text{ or } A_G \exp\left(-\frac{E_G}{RT}\right) P_{H2O}{}^{n}$$

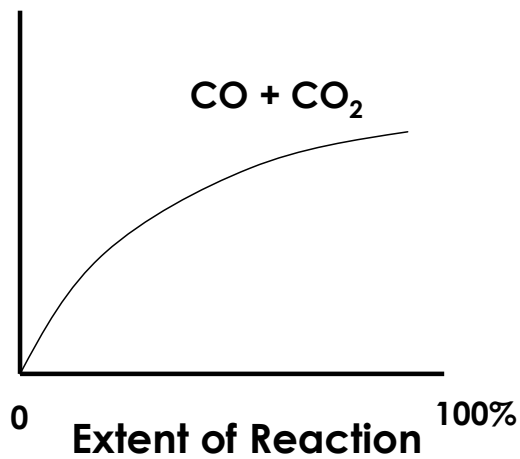


**Figure 16. Sum of CO and $CO_2$ as a funcation of extent of reaction.**

### 3.1.8.2 Effectiveness factor for Langmuir-Hinshelwood kinetics

Generally, the Langmuir-Hinshelwood gasification rate is of the form:

$$r_{in} = \frac{k_1 C_{CO2}}{1 + k_1 C_{CO} + k_3 C_{CO}} \text{ or } r_{in} = \frac{k_1 C_{H2O}}{1 + k_1 C_{H2} + k_3 C_{H2O}}$$

Then, according to Roberts and Satterfield[26]:

$$r_{in} = \frac{k \cdot C_{CO2}}{1 + K \cdot C_{CO2}} \text{ or } r_{in} = \frac{k \cdot C_{H2O}}{1 + K \cdot C_{H2O}}$$

where

$$k = \frac{k_1}{w}$$

$$K = \frac{\left[k_3 - \left(\frac{D_{CO2}}{D_{CO}}\right) \cdot k_2 \cdot \nu_{CO}\right]}{w} \text{ or } K = \frac{\left[k_3 - \left(\frac{D_{H2O}}{D_{H2}}\right) \cdot k_2 \cdot \nu_{H2}\right]}{w}$$

$$w = 1 + k_2 \cdot P_{CO2,S} \cdot \left[ \frac{P_{CO,S}}{P_{CO2,S}} + \nu_{CO} \cdot \left( \frac{D_{CO2}}{D_{CO}} \right) \right] \text{ or}$$

$$w = 1 + k_2 \cdot P_{H2O,S} \cdot \left[ \frac{P_{H2,S}}{P_{H2O,S}} + \nu_{H2} \cdot \left( \frac{D_{H2O}}{D_{H2}} \right) \right]$$

where $r_{in}$ is the intrinsic rate, $\nu_i$ (i = product gas, CO or $H_2$) the stoichiometric coefficient for the products and D the diffusivity.

Then the observed rate would be:

$$r_{obs} = \eta \cdot r_{in}$$

where η is the effectiveness factor.

On the other hand, the global reaction rate can be expressed as:

$$r_{obs} = A \cdot C_s^{\,n}$$

where $C_s$ is the reactant concentration ($CO_2$ or $H_2O$) at the surface.

A global "effective" reaction order can be obtained by:

$$\frac{d \ln(r_{obs})}{d \ln(C_s)} = n_{eff}$$

Then, we can replace $r_{obs}$ with the one from the Langmuir-Hinshelwood expression and obtain the effective reaction order:

$$\frac{d \ln(r_{obs})}{d \ln(C_s)} = \frac{d \ln\left( \eta \cdot \frac{k \cdot C_s}{1 + K \cdot C_s} \right)}{d \ln(C_s)} = \frac{1}{1 + K \cdot C_s} = n_{eff}$$

The Thiele modulus ($M_T$), then, can be expressed as:

$$M_T = \gamma \cdot \sqrt{\rho \cdot \nu_{C-CO2} \frac{n_{eff} + 1}{2 \cdot D_{CO2}} \cdot \frac{1}{C_{CO2,S}} \cdot \frac{k \cdot C_{CO2}}{1 + K \cdot C_{CO2}}} \text{ or}$$

$$M_T = \gamma \cdot \sqrt{\rho \cdot \nu_{C-H2O} \frac{n_{eff} + 1}{2 \cdot D_{H2O}} \cdot \frac{1}{C_{H2O,S}} \cdot \frac{k \cdot C_{H2O}}{1 + K \cdot C_{H2O}}}$$

where $\nu_{C\text{-}CO2}$ and $\nu_{C\text{-}H2O}$ are stoichiometric coefficients for $CO_2$ and $H_2O$ gasification, respectively.

Then the effectiveness factor can be calculated for a sphere from:

$M_T > 4$ $$\eta = \frac{1}{M_T}$$

$M_T < 0.4$ $$\eta = 1$$

$0.4 < M_T < 4$ $$\eta = \frac{1}{3M_T} \cdot \left( \coth(3M_T) - \frac{1}{3M_T} \right)$$

## 3.2 Application of PREKIN

Global oxidation and gasification kinetics parameters were obtained by *PREKIN* for Pittsburgh No. 8 under 27.22 atm of total pressure based on the intrinsic expression of Mühlen et al. (1985)[35] Properties of Pittsburgh No. 8 coal is shown in Table 6. Figure 17 shows *PREKIN* generated kinetics along with EPRI kinetics.[30] EPRI report[30] uses the same kinetics for $H_2O$ and $CO_2$ gasification that is based on Dobner's work at EPRI (1976) performed at one atmosphere assuming it is meaningless to account for difference in gasifcation with inherent errors of extrapolation since combustion is more significant than gasification.[58] EPRI's oxidation rate shows about 3 orders of magnitude higher than those of gasification. *PREKIN* generated the oxidation rate is higher by a factor of 10 than EPRI kinetics at low temperature, but the difference becomes smaller as temperature increases. At the temperatures higher than 1600K, the *PREKIN* rate is higher by a factor of 2 than the EPRI kinetics. *PREKIN* $H_2O$ gasification rate, on the other hand, is higher than EPRI's kinetics, while *PREKIN* $CO_2$ gasification rate is slower than EPRI's $CO_2$ rate. In the *PREKIN* results, the $H_2O$ gasification rate is higher than the $CO_2$ gasification rate by a factor of 10 at 1200K. However, the difference becomes only smaller with increasing temperature and the rates are almost identical at temperatures higher than 1700K. The faster rate of $H_2O$ gasification rate is consistent with the literature data (see Figure 12) in which the $H_2O$ rate is faster than $CO_2$ rate by a factor of 3 or 4 at one atmosphere. At a higher pressure, the difference is expected to be smaller, as the mass diffusion effect becomes more significant.

**Table 6. Pittsburgh No. 8 properties**

| Proximate Analysis | As-Received (wt%) |
|---|---|
| Moisture | 4.74 |
| Ash | 7.88 |
| Volatile Matter | - |
| Fixed Carbon | - |
| HHV (Btu/lb) | 13290 |
| **Ultimate Analysis** | **As-Received (wt%)** |
| Moisture | 4.74 |
| Carbon | 73.76 |
| Hydrogen | 4.72 |
| Nitrogen | 1.39 |
| Sulfur | 2.45 |
| Chlorine | 0.10 |
| Ash | 7.88 |
| Oxygen (by difference) | 4.96 |
| TOTAL | 100.00 |

| size, μm | mass fraction |
|---|---|
| 5.44 | 0.04 |
| 8.95 | 0.06 |
| 12.30 | 0.08 |
| 16.15 | 0.10 |
| 21.19 | 0.13 |
| 29.20 | 0.18 |
| 40.07 | 0.13 |
| 52.53 | 0.10 |
| 69.09 | 0.08 |
| 95.33 | 0.06 |
| 168.72 | 0.04 |

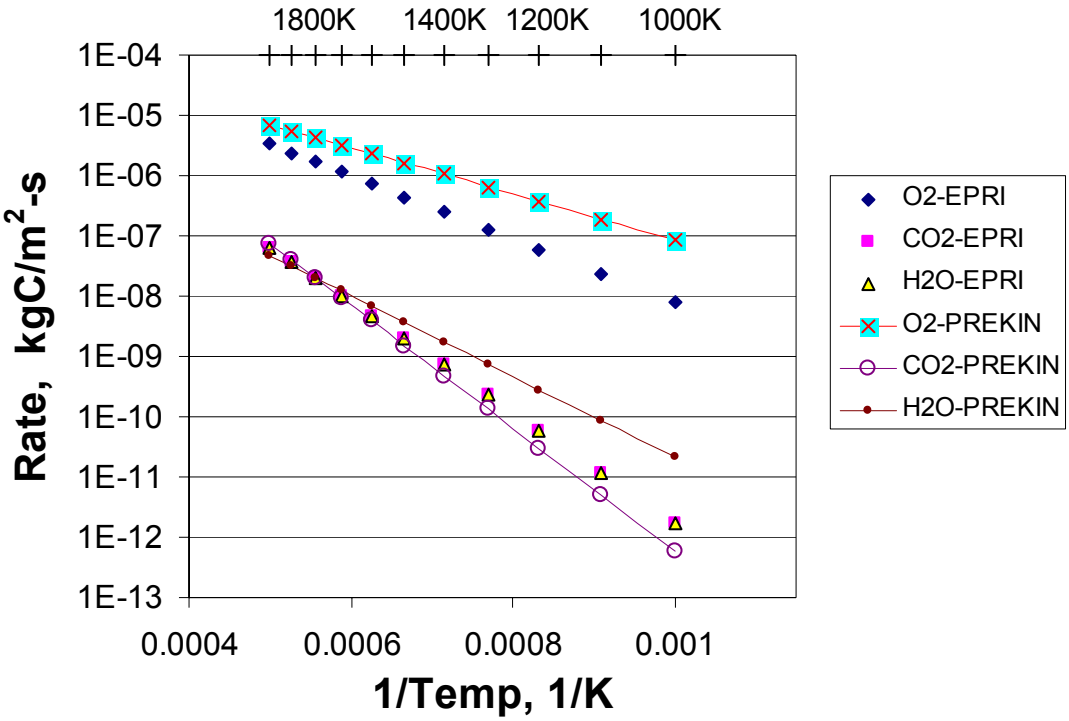


**Figure 17. *PREKIN* generated kinetic parameters along with EPRI kinetics.** [30]

The kinetics was applied to REI's workbench process model that had been developed during the current project. Operating conditions were adapted from the Tampa Electric IGCC power plant configuration.[59] Briefly, the Tampa unit uses a single-stage, downward-firing, entrained-flow coal reactor. The summary of operating conditions is shown in Table 7.

**Table 7. Tampa Electric IGCC power plant operating conditions.**

| | |
|---|---|
| Gasifier Pressure | 27.22 atm |
| Coal | Pittsburgh No. 8 |
| Coal flow rate | 23.10 kg/s |
| Oxidant flow rate | 22.795 kg/s (95% $O_2$ and 5% $N_2$) |
| Slurry temperature | 298K |
| Oxidant temperature | 298K |

Gas product distributions using two different kinetic sets: EPRI and *PREKIN* are compared in Figure 18 along with the reported composition of cleaned syngas from the Tampa unit. The gas product distributions were estimated by assuming similar $H_2O$ and $H_2S$ compositions as in the reported composition. The $CO/CO_2$ ratio based on EPRI kinetics is by a factor of 2 higher than that based on *PREKIN* kinetics, illustrating the

impact of faster char oxidation rate in *PREKIN*. The reported $CO/CO_2$ is 3.0 while EPRI and *PREKIN* kinetics show 4.6 and 2.1, respectively. *PREKIN* kinetics shows lower $H_2$ concentrations, while giving a similar $N_2$ level to the others. Further study is required to understand these differences; however, it is clear that the kinetics used in the model make a significant difference in product gas distribution, therefore, an accurate description of kinetics is required.

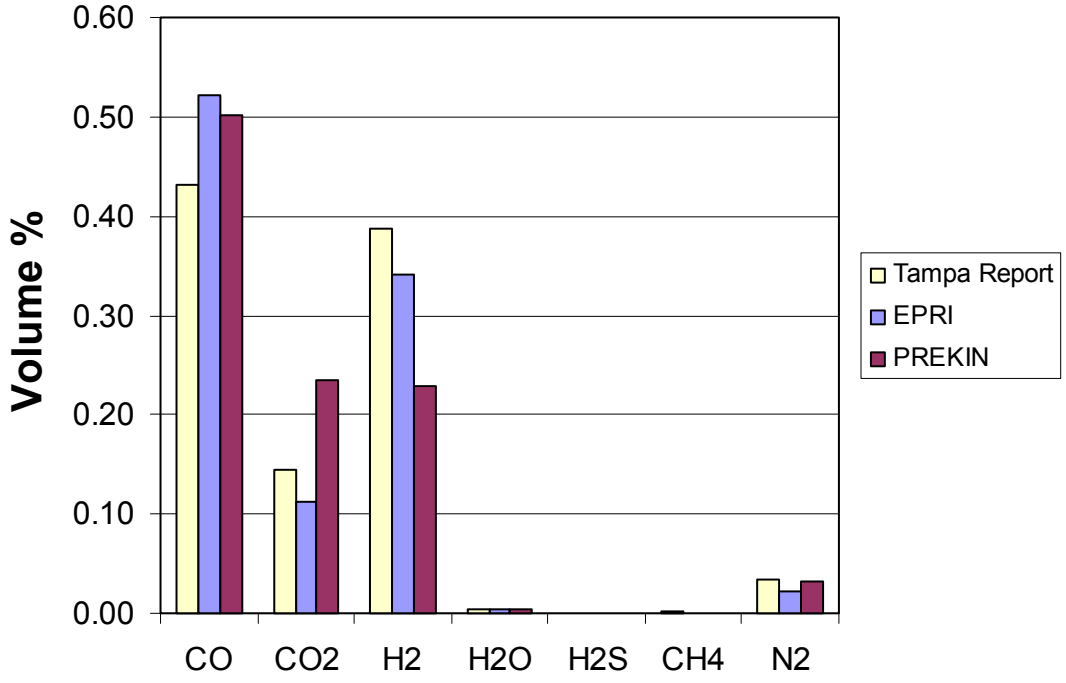


**Figure 18. Comparison of gasification products from Tampa IGCC power plant using EPRI and *PREKIN* kinetics along with the reported composition of cleaned syngas.**

# 4 Concluding Remarks

Kinetics is an important aspect in modeling a gasifer as it is needed to size the gasifier/combustor and determine the char combustion efficiency and possible char recycle requirements. In this study, a literature survey on coal devolatilization and char combustion/gasification was performed to provide guidelines in developing a kinetic package that can be interfaced with REI's process and CFD gasifier models.

The following summarizes the literature survey:

- Wide variations exist in the published kinetics on coal devolatilization, char combustion/gasification. Kinetics were selected from the literature where the author used the kinetics for a gasifier modeling.

- Higher pressure suppresses volatile yield, which should be reflected in devolatilization kinetics for a gasifier. The three most widely used models that predict this behavior include FG-DVC, FLASHCHAIN, and CPD models, all of which predicted similar results. Our approach was to employ the publicly available CPD model and to use a corrected correlation based on Wen et al.'s data.[7]

- High pressure can increase the cenosphere content in the char with a subsequent increase on char reaction rates and a decrease in the particle size of ash produced. A correlation exists from Wall et al.[16] that describes the effect of pressure on the fraction of particles forming cenosphere based on vitrnite content of coal.

- Effectiveness factors estimated by using the kinetics from Mühlen et al.[35] show that chemical kinetics is important at the temperatures lower than 1500K and pore diffusion controls the reaction rate beyond 1500K. As typical gasifier temperatures range from 1200K to 3000K, both mechanisms should be well described in a kinetic model.

- Comparison of the fractional order kinetics of char oxidation and gasification implies that both chemical kinetics and external mass transfer are important due to relatively wide range of temperature found in a gasifier (1200-3000K).

- Product inhibition effect can be significant, over 4 orders of magnitude, under typical $CO/CO_2$ ratios in a real gasifer based on comparisons of various Langmuir-Hinshelwood kinetics available in the literatures.

- Among gasifying agents in a gasifier, $H_2O$ and $H_2$ contributions are higher than $CO_2$ to overall gasification rate based on the calculation performed using Mühlen et al.[35] kinetics.

- Catalytic effects of inorganic matter should be considered in a kinetic model. Literature survey shows that the gasification rates increases with increasing loading of potassium (K/C). This also applies to the oxidation rate.

Based on the literature survey and previous experience in char kinetics modeling, a kinetic preprocessor, *PREKIN*, was developed, which could be interfaced with the REI's process and CFD gasifier models. *PREKIN* includes a fundamental description of combustion/gasification processes including devolatilization, intrinsic rate expression, and pore/mass diffusion. Table 8 shows the implemented models for each process. In addition, thermal annealing and ash inhibition effect are implemented.

**Table 8. Sub-models implemented into *PREKIN*.**

| | |
|---|---|
| Devolatilization | Manual input of volatile yield<br>Two step model[1]<br>CPD[6] |
| Oxidation | Fractional order power law<br>Semi-global kinetics[49] |
| Gasification | Fractional order power law<br>Langmuir-Hinshelwood kinetics |
| Pore structure | Parallel model[54]<br>Random pore model[55] |

Comparison of *PREKIN*-generated kinetics and EPRI kinetics resulted in a somewhat different gasifier product distributions, which emphasizes the need to have a correct kinetics. *PREKIN* provides a mechanistic approach in generating kinetics under typical operating conditions found in a gasifier and it can be easily interfaced with REI's workbench model.

# 5 REFERENCES


1 Kobayashi H,Howard JB,Sarofim AF 16th Symp.(Int.) Comb., Combustion Inst., Pittsburgh, 411 (1977).

2 Ubhayakar SK, Stickler DB, von Rosenberg CW, Gannon RE 16th Symp.(Int.) Comb., Combustion Inst., Pittsburgh, 427 (1977).

3 Solomon P.R., Hamblen D.G., Carangelo R.M., Serio M.A. and Deshpande G.V., General model of coal devolatilization, *Energy & Fuels*, 2, 405, 1988.

4 Solomon P.R., Serio M.A. and Suuberg E.M., Coal pyrolysis: experiments, kinetic rates and mechanisms, *Prog. Energy Combustion Sci*., 18,m 133-220, 1992.

5 Niksa S. and Kerstein A.R., FLASHCHAIN theory for rapid coal devolatilization kinetics 1. Formulation, *Energy & Fuels*, 5, 673-683, 1991.

6 Fletcher T.H., Kerstein A.R., Pugmire R.J. and Grant D.M., *Energy & Fuels*, 4, 54, 1990.

7 Wen C.Y. and Chaung T.Z., Entrained coal gasification modeling, *Ind. Eng. Chem. Process Des. Dev.,* 18, 684-695, 1979.

8 Beath A.C., Mathematical modeling of entrained flow gasification, PhD thesis, University of Newcastle, Australia, 1996.

9 Okumura Y., Sugiyama Y. and Okazaki K., Evolution behavior of coal-nitrogen in high pressure pyrolysis processes, Fuel Chemistry Division Preprints, 46, 141-143, 2001.

10 Gibbins J.R. and Kandiyoti R., The effect of variations in time-temperature history on product distribution from coal pyrolysis, *Fuel*, 68, 895-903, 1989.

11 Griffin T.P., Howard J.B. and Peters W.A., Pressure and temperature effects in bituminous coal pyrolysis: experimental observations and a transient lumped-parameter model, *Fuel*, 73, 591-601, 1994.

12 Suuberg E.M., Peters W.A. and Howard J.B., Product compositions and formation kinetics in rapid pyrolysis of pulverised coal - implications for combustion, *Proceedings of the Combustion Institute*, 17, 117-128, 1978.

13 Anthony D.B. and Howard J.B., Coal devolatilisation and hydrogasification, *AIChE J*., 22, 625-656, 1976.

14 Arendt P. and van Heek K.H., Comparative investigations of coal pyrolysis under inert gas and H2 at low and high heating rates and pressures up to 10 MPa, *Fuel*, 60, 779-787, 1981.

15 Harris D.J., Kelly M.D., Roberts D.G., Mill C.J., Stubington J.F. and Wall T.F., Determining coal reactivity parameters at elevated pressures using bench-scale techniques, 2002.

16 Wall T.F., Liu G.-S., Wu H.-W., Roberts D.G., Benfell K.E., Lucas J.A. and Harris D.J., The effect of pressure on coal reactions during pulverized coal combustion and gasification, to be published, 2002.

17 Request forms, a booklet describing the entire Penn State Coal Sample Bank and Database, and assistance in acquiring samples and data can be obtained from:
Coal and Organic Petrology Laboratories
The Pennsylvania State University
105 Academic Projects Building
University Park, PA 16802-2300

18 Wu, H., Bryant, G. W., and Wall, T. F., *Energy and Fuels*, 14, 745-750 (2000).

19 Hurt, R., Sun, J-K, Lunden, M., *Combustion and Flame,* 113, 181 (1998)
20 Senneca, O., Salatino, P., Masi, S., *Fuel*, 77, 1483 (1998).
21 Smith I.W., The combustion rates of coal chars: a review, *Proceedings of the Combustion Institute*, 1045-1065 (1982)
22 Benfell, K. E., Liu, G.-S., Roberts, D. G., Harris, D. J., Lucas, J. A., Bailey, J. D., and Wall, T. F., *Proceedings of the Combustion Institute,*28, 2233-2241 (2000)
23 Harris D.J., Kelly M.D., Roberts D.G., Mill C.J., Stubington J.F. and Wall T.F., Determining coal reactivity parameters at elevated pressures using bench-scale techniques, 2002.
24 Liu, G., Benyon, P., Benfell, K.E., Bryant, G.W., Tate, A.G., Boyd, R. K., Harris, D.J., and Wall, T.F., *Fuel*, 79, 617-626 (2000)
25 Roberts, D.G., Harris, D. J., and Wall, T. F. , "High-Pressure Intrinsic Char Gasification Kinetics: an Application of a modified nth-order rate equation", 18th Pittsburgh Coal Conference, Newcastle, Australia, 3-7 Dec, 2001.
26 Roberts GW, Satterfield CN, "Effectiveness Factor for Porous Catalysts", Ind. Eng. Chem. Fundamentals, Vol. 4, No. 3, 288 (1965)
27 Banin et al., *Combustion and Flame*, 108, 1-8 (1997)
28 Joutsenoja et al., *Energy and Fuels*, 13, 130-145 (1999)
29 Monson et al., *Combustion and Flame*, 100, 669-683 (1995)
30 Lupa and Kliesch, "Simulation of a Texcao Gasifier, Vol.1 A Steady State Model", EPRI Report AF-1179, Vol. 1 Research Project 1037-1. Final Report, 1979
31 Otaka et al., 26th International Conference on Coal Utilization and Fuel Systems, Clearwater, Fl., 2001
32 Benyon P.J., Computational modeling of entrained flow slagging gasifiers, PhD thesis, University of Sydney, Australia, 2002.
33 Harris, D. J., and Smith, I. W., *Proceedings of the Combustion Institute*, 23, 1185-1190 (1990)
34 Roberts, D. G., and Harris, D. J., *Energy & Fuels*, 14, 483-489 (2000)
35 Mühlen H-J,van Heek KH,Jüntgen H "Kinetic studies of steam gasification of char in the presence of H2, CO2 and CO" Fuel, Vol 64, July, 944-949 (1985).
36 Wu P-C, Lower WE, Hottel HC "Reaction kinetics of carbon dioxide with electrode carbon particles", Fuel, Vol 67, February, 205 (1988).
37 Gadsby J, Long FJ, Sleightholm P, Sykes KW Proc.Roy.Soc.(London) 1948, A193, 357
38 Wu PC "The kinetics of the reaction of carbon with carbon dioxide", ScD thesis Chem.Eng., Massachusetts Institute of Technology, 1949
39 McBride GT Jr. "Gasification of carbon by carbon dioxide in a fluidized bed", ScD thesis Chem.Eng., Massachusetts Institute of Technology, 1947.
40 Strange JF, Walker PL Jr. Carbon 1976, 14, 345.
41 Mentser M, Ergun S, "A study of the carbon dioxide carbon reaction by oxygen exchange", Bull.US Bur.Mines No. 664, 1973.
42 Biederman DL "A study of the oxidation of graphite by carbon dioxide", PhD Thesis, Penn. State Univ., 1965.
43 Ergun S J.Phys.Chem. 1956, 60,480.
44 von Fredersdorff CG, Pyrcioch EJ, Pettyjohn ES Inst.Gas Technol., Research Bull., NO. 7, 71 (1957)

45 Lewis WK, Gilliland ER, McBride GT Jr., Ind.Eng.Chem. 31, 1213-26 (1949)
46 Chapman S, Cowling TG "Mathematical Theory of Non-Uniform Gases", Second Edition, Cambridge University Press (1951), Chapaters 10 and 14.
47 Meijer R, Sibeijn M, van Dillen MRB, Kapteijn F, Moulijn JA I&EC Research., 30(8), 1760-1770 (1991).
48 Grant, D. M., R. J. Pugmire, T. H. Fletcher, and A. R. Kerstein, "A Chemical Model of Coal Devolatilization Using Percolation Lattice Statistics," Energy and Fuels, 3, 175 (1989).
49 Hurt RH,Calo JM Semi-Global Intrinsic Kinetics for Char Combustion Modeling Comb.Flame 125, 1138-1149 (2001).
50 Frank-Kamenetskii DA, Diffusion and Heat Transfer in Chemical Kinetics, Plenum Press, New York (1969).
51 Hurt RH,Sun JK,Lunden M, " A Kinetics Model of Carbon Burnout in Pulverized Coal Combustion," Combustion and Flame 113, 181 (1998).
52 Mitchell RE, Hurt RH, Baxter LL, Hardesty DR Compilation of Sandia Coal Char Combustion Data and Kinetic Analyses: Milestone Report Sandia Technical Report, SAND92-8208, 1992.
53 Mitchell RE A Theoretical Model of Chemically reacting Recirculating Flows, Sandia Technical Report, SAND79-8236, Sandia National Laboratory, Livermore, CA (1980)
54 Wheeler A, Advances in Catalysis, Adademic Press, New York (1951).
55 Wakao N, Smith JM, Diffusion in Catalyst Pellets, Chem. Eng. Sci., 17, 825 (1962).
56 Suuberg EM, Fundamental Issues in Control of Carbon Gasification Reactivity, Kluwer Academic Publishers, Dordrecht (1991).
57 Hampartsoumian JE, Pourkashanian M, Williams A Journal of the Institute of Energy, March, p. 48 (1989)
58 Dobner S, Modeling of Entrained Bed Gasification: The Issues; EPRI Internal Report, 1/15/76.
59 Tampa Electric Integrated Gasification Combined-Cycle Project, Clean Coal Technology Topical Report Number 19, July 2000.